

University of Nottingham
UK | CHINA | MALAYSIA

Optimal Design of Magnetic Fields in a Magnetically Shielded Cylinder

Michael W. Packer

Thesis submitted to the University of Nottingham
for the degree of Doctor of Philosophy

Supervised by T.M. Fromhold

To my parents, who continued to love, support, and encourage me throughout my years of education. Without you, this would not have been possible.

Abstract

Magnetic field control of sensitive equipment is at the cornerstone of many experiments and state-of-the-art technologies. The industrial applications of these technologies range from geophysical mapping of mineral deposits to the detection of bio-magnetic signals from the human body. Due to their low background magnetic field requirements, some of these experiments and technologies need high-permeability magnetic shields to minimize erroneous fields and reduce external interference. Active current-carrying field-generating components can then be designed to select the desired field profile, or remove further unwanted deviations, within the shielded environment. However, the active components' intended field profile is distorted by the high-permeability material, inhibiting the ability to control the magnetic field environment accurately. Various magnetic field design methods are discussed within this work which are built upon to allow the accurate generation of magnetic fields in shielded environments. Specifically, throughout three publication-style chapters, the interaction of static magnetic fields in a finite-length high-permeability cylindrical magnetic shield is investigated.

In the first two research chapters, the Green's function solution for the magnetic vector potential generated by a current source is modified to account for a closed finite-length cylindrical magnetic shield in a cylindrical and planar coil basis, respectively. The boundary condition on the surface of the magnetic shield is satisfied through matching the azimuthal Fourier modes allowing the response of the shield to be determined in terms of the initial current source. Using this formulation, a quadratic optimization procedure is utilized to find globally optimal continuum current solutions that can accurately generate any arbitrary physical magnetic field within a magnetically shielded cylinder in free space. These analytical formulations mark a notable shift in understanding the response of cylindrical magnetic shields to internal magnetic fields, enabling the efficient and accurate design of magnetic fields in shielded environments.

The third research chapter builds on the previous work by examining discrete current loops near the interior surface of a cylindrical magnetic shield. A coil basis formed of discrete 'building blocks' is formulated and the magnetic field decomposed into a set of orthogonal harmonic fields. Optimal coil configurations of these building blocks are then determined using a genetic algorithm, creating accurate and simplistic field generating systems. These design methods allow the construction of compact active field generating structures, facilitating the miniaturization of new technologies, enabling laboratory-based experimental systems to be taken into real-world settings.

Acknowledgements

First and foremost, I would like to thank my parents as I would not be here without them. Their unwavering support has allowed me to add, however small, to the vast quantity of human knowledge and understanding, and, for this, I will be forever grateful. Along side my parents, I would like to thank the rest of my family, specifically my grandad, who I used to call on my walks home from university. His encouragement and pride in me meant more to me than he will ever know.

I would also like to express my sincere gratitude to my supervisor Professor Mark Fromhold. His guidance through the minefield, that is academia, has been indispensable. His mentorship and faith in my abilities, no matter how misplaced, gave me the confidence to push myself further than I ever thought was possible.

I would like to sincerely thank everyone from the Sir Peter Mansfield Imaging Centre, who was involved in the work. Notably, I would like to thank Professor Richard Bowtell for the incredibly insightful talks, comments, and suggestions throughout the years. I would also like to thank Professor Matthew Brookes for the research opportunities and for showing me that a lot of the research could be done after office hours in the pub.

To all the people who have endured me throughout the years, Chris, Rosy, Hannah, Peter, Noah, and everyone else, thank you. They were always there when I needed them the most, and without them, writing this would not have been possible.

Lastly, I am deeply grateful to my partner Jess and her family. Words can not describe how truly appreciative I am for the help and encouragement throughout the years. I look forward to many more of the same.

List of Publications

1. Optimal Inverse Design of Magnetic Field Profiles in a Magnetically Shielded Cylinder - Published in Physics Review Applied [Chapter 3]

2. Planar Coil Optimization in a Magnetically Shielded Cylinder - Published by Physics Review Applied [Chapter 4]

3. Genetic Algorithm Optimization of Discrete Coils in a High Permeability Cylinder - Submitted [Chapter 5]

4. UK Government Intellectual Property Office (Application No.1913549.0) [Chapters 3-5]

Contents

Abstract i

Acknowledgements ii

List of Publications iii

1 Introduction 1

2 Magnetic Fields 6

2.1 Magnetostatics 6

2.2 Magnetic Field Design Methodologies 9

2.2.1 Discrete Methods 9

2.2.2 Pseudo-Analytical Methods 13

2.2.3 Numerical Methods 14

2.3 Mathematical Optimization Used in Magnetic Field Design . . . 16

2.3.1 Quadratic Programming 18

2.3.2 Multi-objective Optimization 20

2.4 Magnetic Field Design in Magnetic Shields 22

3 Optimal Inverse Design of Magnetic Field Profiles in a Magnetically Shielded Cylinder 29

4 Planar Coil Optimization in a Magnetically Shielded Cylinder 30

5 Magnetic Field design in a Cylindrical High Permeability Shield: The Combination of Simple Building Blocks and a Genetic Algorithm 31

6 Conclusion 32

Bibliography 35

Appendices 42

A Cartesian Differentiation of Spherical Harmonics 42

Chapter 1

Introduction

The generation of magnetic fields has been of interest within various fields of research for decades. Fundamentally, the existence of magnetic fields results from either the flow of electrons or material properties. Therefore, the field strength and its direction can vary both spatially and temporally, giving rise to complex magnetic field landscapes. These magnetic fields, in turn, affect the movement of atoms and change the properties of materials. The exploitation of intricate magnetic field patterns has since resulted in many technological advancements which are entirely dependent on the accurate generation of magnetic fields.

Magnetic resonance imaging (MRI) is arguably the most prominent application of accurate spatially and temporally dependent magnetic fields in recent years. Clinical MRI demands magnetic fields of very high homogeneity, usually generated by superconducting magnets orientated in a single direction [1]. Additional active current elements, specifically shim coils [2], produce orthogonal harmonic field variations along the superconducting magnet's major axis to fine-tune the homogeneous field and improve the spatial imaging resolution. Coils that can generate time-varying magnetic field gradients [3] then act to encode the nuclear magnetic resonance (NMR) signal to image a particular sample. Due to the magnetic fields' desired accuracy and the requirement for fast and efficient medical diagnosis, there has been considerable effort in de-

signing passive magnetic material [4, 5] and active coils [6, 7] based on the analytical and numerical calculation of magnetic fields. Similar design methods have also been employed for plasma containment in fusion reactors [8], atom-trap design [9, 10], and compensation systems [11], facilitating progress within their respective disciplines.

Through technological development, atomic physics has been able to utilize magnetic fields to make tremendous progress in understanding physics's fundamental laws. Magnetically sensitive atoms are at the center of many fundamental research experiments, being used to test exotic states of matter [12], the equivalence principle [13], fine structure constants [14], and gravitational waves [15]. Through the investigation of these fundamental experiments, real-world applications have emerged to exploit these phenomena, such as rotation and inertial sensors [16], ultra-precise atomic clocks [17], and gravity sensors [18]. The aim of many of these devices is to supersede current state-of-the-art technologies by using quantum phenomena. For many of these devices to become commercially viable, they must be miniaturized so that laboratory-based experiments can be taken out into real-world environments [19]. This process is complicated, as every component within the system has specific performance requirements and must also provide a low size, weight, power, and cost solution [20]. Due to the reliance on quantum phenomena and magnetically sensitive atoms, many of these technologies demand precisely monitored magnetic field environments to ensure their reliability [21, 22].

Due to the systems' sensitivity to erroneous fields [23–25], many of these experiments need magnetic shielding to attain the required field stability. This shielding is usually performed with high-permeability materials, which divert areas of high field variation away from enclosed regions by providing a low resistance pathway for magnetic field lines. These shields, therefore, are required for many of these laboratory-based experiments [26, 27]. The desired magnetic field variations within these shielded environments can then be selected through the generation or further cancellation of magnetic fields using

active field-generating components. However, the same mechanisms that allow effective magnetic shielding also warp the magnetic field generated by internal active components, introducing inaccuracies within the system [28].

In systems that require a zero-field environment, active structures can be used to lower the remnant background field within the shielded region [29]. This reduction in the background field allows the removal of small amounts of passive shielding material, therefore lowering the system's size, weight, and cost. However, due to the active components' interaction with the shield, active field cancellation systems designed using standard methods are only effective over small regions at large distances from the passive material. Within systems that require an accurate, actively driven, background field the error introduced by the interaction between the shield and active components must be minimized. Therefore, if standard design methods are used, these components need to be either spatially distant from the shield or self-canceling [30], unnecessarily increasing the system's size, weight, power, and cost. Due to this interaction, further improvement and miniaturization of these laboratory-based experiments is limited, preventing these technologies' advancement.

Here, a comprehensive design method of quasi-static magnetic fields in cylindrical high-permeability magnetic shields is presented. Although this work's applications directly relate to physics, and to technological developments concerning it, the methods and techniques used throughout are more mathematical in nature. Hence, the specific experimental dependence on the accurate generation of magnetic fields is omitted. This work's primary focus is on the mathematical formulation of the governing equations, the exploitation of symmetries, and the approximate analytical solutions of quasi-static magnetic fields generated by active structures within cylindrical high-permeability magnetic shields. Mathematically-based optimization procedures are then used to allow the optimal generation of user-defined magnetic field profiles in these shielded environments. The results provide numerous solutions to the long-standing issue of optimal active field generation within magnetically shielded

quantum technologies.

The work begins with an introduction to the basics of magnetostatics, discussing and formulating the fundamental governing equations that dictate the generation of magnetic fields in free space. An overview of established magnetic field design methods, pertaining to the formulation of gradient and shim coils, is then considered, broadly discussing their merits. The optimization methods used in magnetic field design are then discussed. Design methods that account for the interaction of magnetic shields and their boundary conditions are then reviewed, and their limitations are presented.

Three publication-style chapters are written to provide a complete solution to quasi-static magnetic field design within a high-permeability cylinder, each tackling the problem with a distinct set of active components. They do, however, formulate the problem in the same way. The boundary condition on the high-permeability finite-length cylinder's surface is approximated to that of a perfect magnetic conductor. The magnetic field generated by the finite-length perfect magnetically-conducting cylinder is then cast in terms of a mathematically equivalent pseudo-current density. The problem is decomposed into a cylindrically symmetric Green's function, and the magnetic field generated by the shield and current source matched to satisfy the boundary condition on the magnetic shield's surface. The magnetic field generated by the shield is then found in terms of the initial current source, and the magnetic field generated by the entire system is calculated. An optimization method is then applied to find optimized configurations to generate arbitrary magnetic fields in magnetically shielded environments.

Within the first research chapter, arbitrary cylindrical currents are considered. The total magnetic field generated by the shield and current source at an arbitrary radial position within the coil is determined in terms of a set of Fourier coefficients that dictate the magnitude and flow of a cylindrical streamfunction. This formulation is then cast into a quadratic programming problem where the optimal Fourier coefficients can be found to generate a desired magnetic field

at a set of preselected points through matrix inversion. Due to the ill-posed nature of this problem, a Tikhonov regularization is applied to facilitate the inversion. This regularization, for this example, is the power dissipated, allowing the design of accurate low-power systems in cylindrical high-permeability magnetic shields.

The second research chapter considers arbitrary planar current sources perpendicular to the cylindrical magnetic shield's major axis. Again, the combined magnetic field from the source and shield is calculated at an arbitrary point within the magnetic shield and determined in terms of a set of Fourier coefficients that dictate the planar current source's flow. This formulation is also cast into a quadratic programming problem and solved using the same methods described in the first research chapter.

The last research chapter covers the design of discrete cylindrical currents. Using the formulation derived within the first research chapter, the magnetic fields generated by a complete coil basis are analyzed. The fields generated by the basis are then decomposed into the set of harmonic fields and their magnitudes related to simple coil parameters. Using these relations and a genetic algorithm, optimal discrete structures are determined that generate user-defined magnetic fields.

Within the final chapter, the design methods are summarized, and their advantages and disadvantages are discussed. The prospects of further development and future work are considered.

Chapter 2

Magnetic Fields

2.1 Magnetostatics

To effectively design magnetic fields, their physical formation must be understood from a mathematical perspective. The magnetic field strength, $\mathbf{H}$, may be expressed in terms of the vector potential, $\mathbf{A}$, as well as the scalar potential, Φ. Any transformation of these variables leads to an arbitrary choice of gauge in the way the potential is defined. As the problems studied here are in the quasi-static regime, using the Coulomb gauge is the most logical choice for simplicity, and so, unless stated, this gauge is used throughout. The Maxwell equations that describe static magnetic fields, through a volume within which no current passes, are given by Gauss' and Ampere's law, respectively,

$$\nabla \cdot \mathbf{B} = \nabla \wedge \mathbf{H} = 0, \tag{2.1}$$

with the magnetic flux density, $\mathbf{B}$, being related to the scalar and vector potential by

$$\mathbf{B} = -\nabla\Phi = \nabla \wedge \mathbf{A}. \tag{2.2}$$

The magnetic flux density may be related to the magnetic field strength through the use of the magnetic permeability, μ, in free space this relation

takes the simplified form of

$$\mathbf{B} = \mu_0(\mathbf{H} + \mathbf{M}), \tag{2.3}$$

where $\mathbf{M}$ is the magnetization relating to the bound pseudo-current density of a magnetized surface

$$\mathbf{J}_b = \nabla \wedge \mathbf{M}. \tag{2.4}$$

Upon substitution of (2.2) into (2.1) it is found that

$$\nabla \cdot \nabla\Phi = \nabla \wedge \nabla \wedge \mathbf{A} = 0. \tag{2.5}$$

Using vector identities with choice of gauge, $\nabla \cdot \mathbf{A} = 0$, it is seen that the scalar and vector potential satisfy Laplace's equation,

$$\nabla^2\Phi = \nabla^2\mathbf{A} = 0. \tag{2.6}$$

It then follows that

$$\nabla^2\mathbf{B} = 0. \tag{2.7}$$

Laplace's equations may be solved in spherical polar coordinates such that,

$$\nabla^2 f = \frac{1}{r^2}\frac{\partial}{\partial r}\left(r^2\frac{\partial f}{\partial r}\right) + \frac{1}{r^2\sin^2\theta}\frac{\partial^2 f}{\partial \phi^2} + \frac{1}{r^2\sin\theta}\left(\sin\theta\frac{\partial f}{\partial \theta}\right) = 0, \tag{2.8}$$

which, through the use of separation of variables, has real solutions of the form

$$f = \sum_{n=0}^{\infty}\sum_{m=-n}^{n} C_{nm}\begin{pmatrix} r^n \\ r^{-n-1}\end{pmatrix} P_{nm}\left(\cos\theta\right)\cos\left(m\left(\phi - \psi\right)\right), \tag{2.9}$$

where $P_{nm}(x)$ are Ferrer's associated Legendre polynomials of the n^{th} order and m^{th} degree and ψ is an arbitrary angular rotation. These functions generate a complete orthogonal basis for both the scalar and vector magnetic potential, as well as the individual magnetic field components. From this, the physical

set of magnetic fields may be constructed from the relationship of the scalar potential and the magnetic field. In Cartesian coordinates, about the origin, the magnetic field can be written as

$$\begin{aligned} B_x = \tfrac{r^{n-1}}{2}(-(1+\delta_{m,0})P_{n-1,m+1}\left(\cos\theta\right)\cos\left((m+1)\left(\phi-\psi\right)\right) \\ +(1-\delta_{m,0})(n+m)(n+m-1)P_{n-1,m-1}\left(\cos\theta\right)\cos((m-1)\left(\phi-\psi\right))) \end{aligned} \tag{2.10}$$

$$\begin{aligned} B_y = \tfrac{r^{n-1}}{2}(-(1+\delta_{m,0})P_{n-1,m+1}\left(\cos\theta\right)\sin\left((m+1)\left(\phi-\psi\right)\right) \\ -(1-\delta_{m,0})(n+m)(n+m-1)P_{n-1,m-1}\left(\cos\theta\right)\sin((m-1)\left(\phi-\psi\right))) \end{aligned} \tag{2.11}$$

$$B_z = r^{n-1}(n+m)P_{n-1,m}\left(\cos\theta\right)\cos\left(m\left(\phi-\psi\right)\right), \tag{2.12}$$

where the derivation is given in Appendix. A. In the case where the magnetic field is the result of a current source, $\mathbf{J_c}$, Ampere's Law states that

$$\nabla \wedge \mathbf{H} = \mathbf{J_c}, \tag{2.13}$$

which, when combined with the bound current from a magnetized material (2.4), results in the Poisson equation,

$$\nabla^2 \mathbf{A} = -\mu_0(\mathbf{J_c} + \mathbf{J_b}). \tag{2.14}$$

This may be reformulated through the use of a Green's function for an arbitrary current with integral solutions

$$\mathbf{A}\left(\mathbf{r}\right) = \frac{\mu_0}{4\pi}\int_V \mathrm{d}V\left(\mathbf{r}'\right)\frac{\mathbf{J}\left(\mathbf{r}'\right)}{\left|\mathbf{r}-\mathbf{r}'\right|}, \tag{2.15}$$

which, by taking the curl of the above, yields the Biot-Savart Law,

$$\mathbf{B}\left(\mathbf{r}\right) = \frac{\mu_0}{4\pi}\int_V \mathrm{d}V\left(\mathbf{r}'\right)\frac{\mathbf{J}\left(\mathbf{r}'\right)\wedge\left(\mathbf{r}-\mathbf{r}'\right)}{\left|\mathbf{r}-\mathbf{r}'\right|^3}, \tag{2.16}$$

whose differentials take the form

$$\mathrm{d}\mathbf{A}\left(\mathbf{r}\right) = \mathrm{d}V\left(\mathbf{r}'\right)\frac{\mu_0}{4\pi}\frac{\mathbf{J}\left(\mathbf{r}'\right)}{\left|\mathbf{r}-\mathbf{r}'\right|}, \tag{2.17}$$

and

$$\mathrm{d}\mathbf{B}\left(\mathbf{r}\right) = \mathrm{d}V\left(\mathbf{r}'\right)\frac{\mu_0}{4\pi}\frac{\mathbf{J}\left(\mathbf{r}'\right)\wedge\left(\mathbf{r}-\mathbf{r}'\right)}{\left|\mathbf{r}-\mathbf{r}'\right|^3}, \tag{2.18}$$

respectively. Rather than relating the magnetic field contributions to the current through the generalized volume element $\mathrm{d}V(\mathbf{r}')$, it may be useful to represent this instead by the current flow over a surface, S, with infinitesimal elements $\mathrm{d}S(\mathbf{r}')$, or the current intensity, I, through a closed curve, C, by wire elements $\mathrm{d}\mathbf{l}(\mathbf{r}')$. These equations underpin all static magnetic fields and, hence, dictate every coil design method, in some form or another.

2.2 Magnetic Field Design Methodologies

Generally speaking, coil design methods can be broadly separated into three cases, discrete, pseudo-analytical, and numerical. Within these sections, an array of sophisticated techniques are used to design magnetic fields for a whole host of applications such as cold atom experiments [31, 32], geophysical mapping [33], fusion reactor design [34], medical imaging [35, 36], and many more. The medical imaging community, specifically, has provided incredible advancements in the theory behind magnetic field design, spurred on through the need for faster, more accurate, and situationally specific MRI machines. Due to the rigorous and substantial existing literature, the focus here is on the design methods of gradient and shim coils for MRI.

2.2.1 Discrete Methods

Discrete coil geometries have been used for decades with the most basic configurations formed from simple loops designed through symmetry arguments. The conventional Helmholtz-type coils, which predominantly generate axial

bias and gradient fields, are formed with two circular loops of radius ρ_c, carrying currents of I, placed equidistant from the origin at $z_0 = \pm d$. The two coaxial loops, if placed in the xy-plane, generate a magnetic field along the z axis of

$$B_z(z) = \frac{\mu_0 I \rho_c^2}{2\left[\rho_c^2 + (z - z_0)^2\right]^{\frac{3}{2}}} \pm \frac{\mu_0 I \rho_c^2}{2\left[\rho_c^2 + (z + z_0)^2\right]^{\frac{3}{2}}}. \tag{2.19}$$

These arrangements prohibit all odd and even variations, respectively, where the separation distance may be chosen to cancel the leading-order errors in the Taylor expansion [37]. These designs are depicted in Fig. 2.1 a-b.

Other simple configurations such as Golay coils may also be constructed using simple symmetry arguments. Golay coils are constructed from arcs of azimuthal periodicity π connected via straight axial wires forming double saddle setups. The saddle positions are then chosen to minimize the unwanted harmonics, A_{nm} and B_{nm} for $m \neq 1$ and $n \neq 1$, in the axial field

$$B_z(r, \theta, \phi) = \sum_{n=0}^{\infty} \sum_{m=0}^{n} r^n P_{nm}(\cos\theta) \left(A_{nm} \cos(m\phi) + B_{nm} \sin(m\phi)\right), \tag{2.20}$$

expanding each wire element and maximizing the linear gradient in the transverse direction [38], depicted in Fig. 2.1 c.

Building on these simple design methods, Romeo and Hoult first laid the theoretical framework to design MRI shim coils [39] through the use of loops and arcs. They expanded the Green's function within the differential form of the vector potential (2.17), using spherical harmonics, and generated an expression that contained the entire set of orthogonal fields (2.12) in terms of surface current elements

$$\begin{aligned} d\mathbf{A}(r, \theta, \phi) = \frac{I d\mathbf{s}}{4\pi r'} \sum_{n=0}^{\infty} \sum_{m=0}^{n} \epsilon_m \frac{(n-m)!}{(n+m)!} \\ \times P_{nm}(\cos\alpha) \left(\frac{r}{r'}\right)^n P_{nm}(\cos\theta) \cos\left(m\left(\phi - \psi\right)\right), \end{aligned} \tag{2.21}$$

where the Neumann factor $\epsilon_m = 1$ if $m = 0$ and $\epsilon_m = 2$ otherwise, and

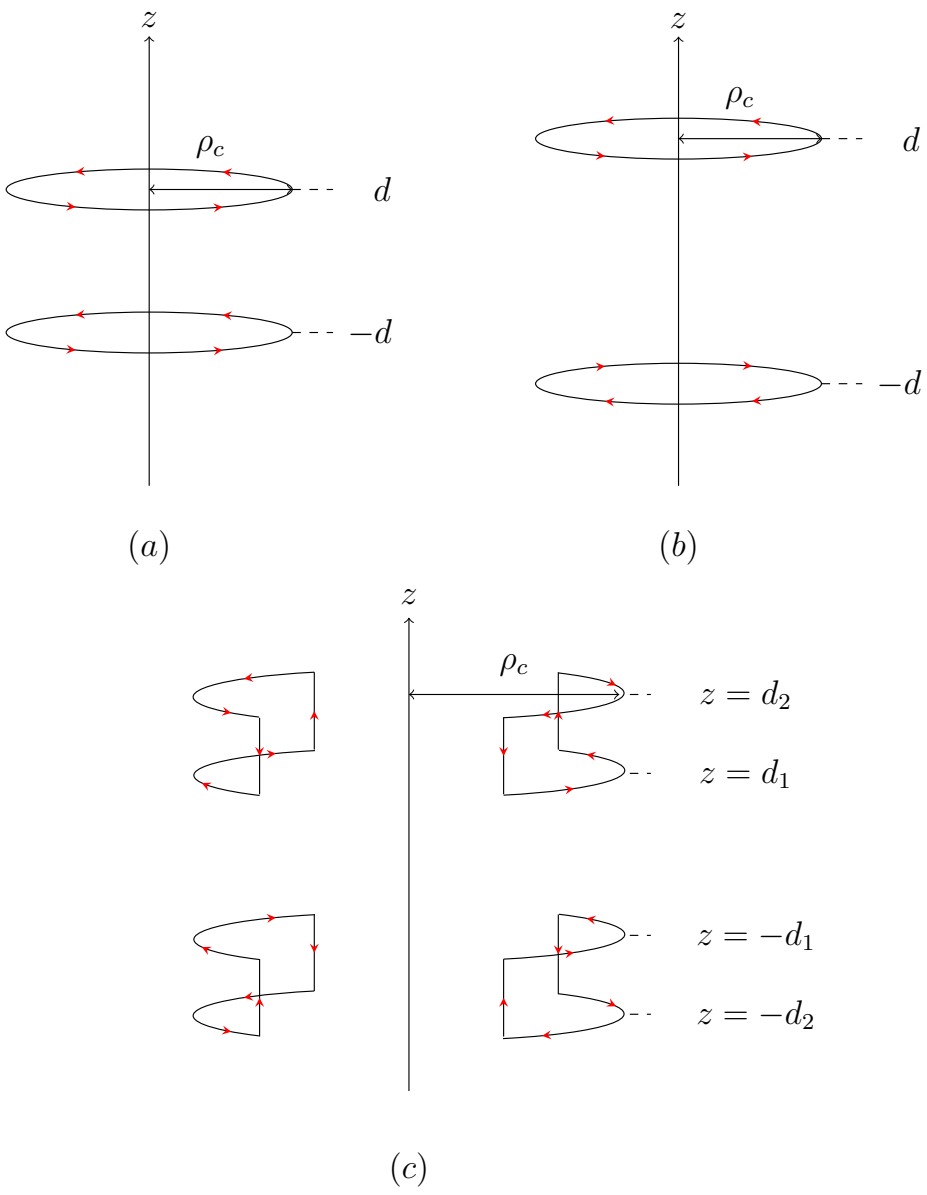


Figure 2.1: *Coil configurations for (a) Helmholtz with separation $d = \rho_c/2$ (b) anti-Helmholtz with separation $d = \sqrt{3}\rho_c/2$ and (c) Golay coil where $d_1 = 0.388\rho_c$ and $d_2 = 3.89\rho_c$.*

(r', α, ψ) is the position of the surface element. The radius, zenith position, angular length, and the number of these loops and arcs could then be adjusted to select specific harmonic variations in the magnetic field while minimizing erroneous contributions. Example zonal designs found using this method are depicted in Fig. 2.2.

The main drawback of these methods is that they are difficult to implement generally. For a given application, they require the magnetic field's formulation and symmetries within the system to be completely understood. However, if

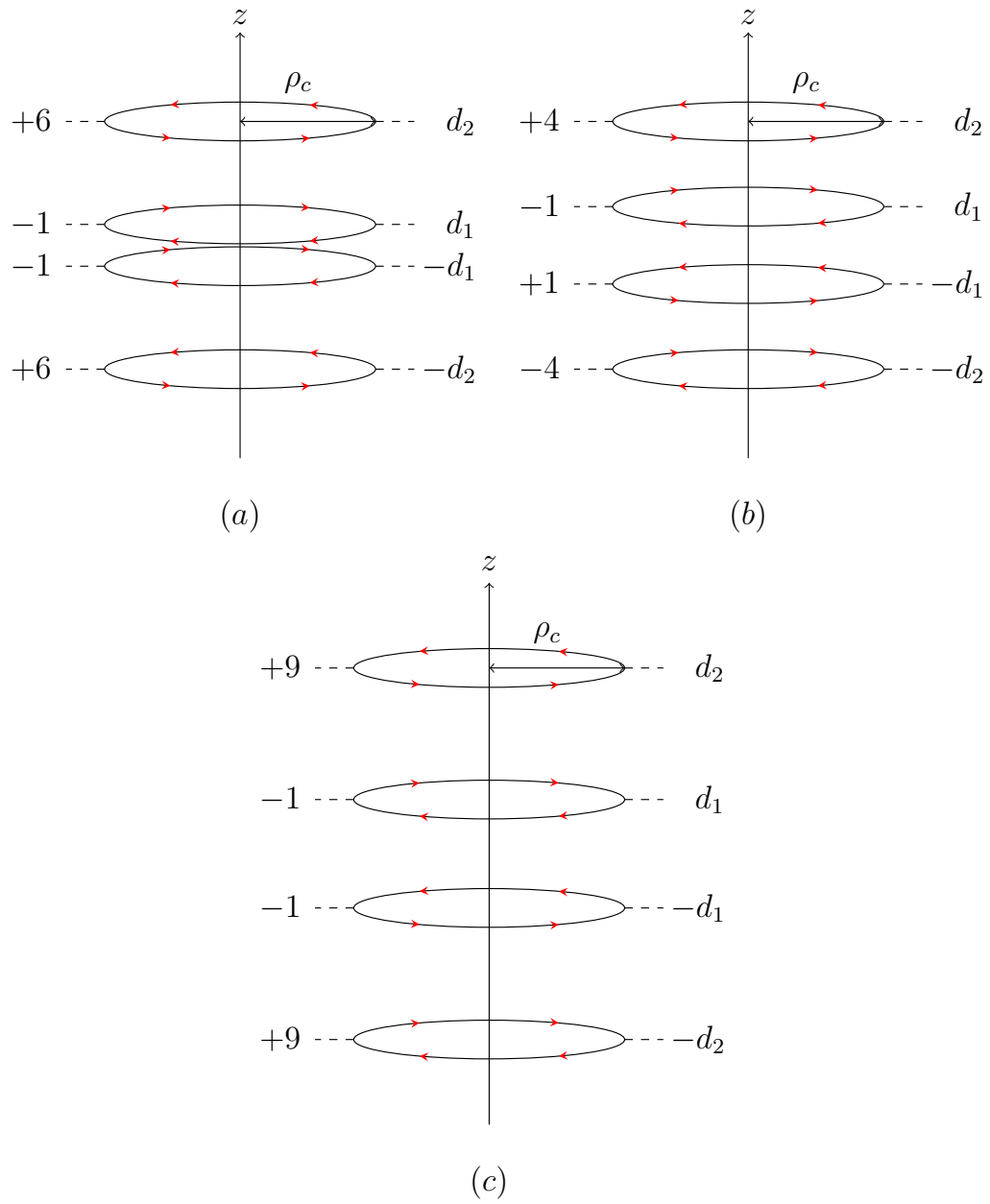


Figure 2.2: *Axial harmonics $m = 0$ (a) $n = 2$ where $d_1 = 0.268$ and $d_2 = 1.594$ (b) $n = 3$ where $d_1 = 0.510$ and $d_2 = 1.558$ and (c) $n = 4$ where $d_1 = 0.729$ and $d_2 = 2.379$. The number of turns through each loop and the direction of current flow ($\pm$ indicates clockwise/anti-clockwise with respect to the z-axis) are shown to the left of the coil and the loop positions, d_i, are shown to the right.*

the problem is setup correctly, the desired magnetic field can be efficiently generated using a small and straightforward arrangement of preselected current elements. Based on the decomposition of specific field variations, these discrete design methods present the first of many steps towards the modern design methods used today. For brevity the symmetries between the harmonic fields and current elements are not discussed since discrete design is covered in depth

within chapter 5.

2.2.2 Pseudo-Analytical Methods

Turner presented the first pseudo-analytical method of coil design [40] using a Fourier-Bessel expansion of the Green's function,

$$\frac{1}{|\mathbf{r}-\mathbf{r}'|} = \frac{1}{\pi}\sum_{m=-\infty}^{\infty}\int_{-\infty}^{\infty} \mathrm{d}k \quad e^{im(\phi-\phi')}e^{ik(z-z')}I_m(k\rho_<)K_m(k\rho_>), \tag{2.22}$$

where $I_\nu(z)$ and $K_\nu(z)$ are the modified Bessel functions of order ν. This expansion enabled the symmetries within the cylindrical system to be exploited to generate simple relations between the Fourier transform of the azimuthal current density and the axial magnetic field. The current density can then be determined for a given target magnetic field from this simple relation using numerical methods. This method, based on the convergence of the modified Bessel functions, provides well-behaved coil structures. One downside of this method is that there is no exact coil length specified, resulting in some impractical designs. However, constraints may be added to design physically realistic coils over a finite interval at the cost of compromising field fidelity [41].

The target field method was then built on by Hoult [42], who used a matrix description of the magnetic field at N different locations. If the N points are chosen well, this provides a non-singular, though ill-conditioned, matrix inversion problem, which yields multiple, very different, possible wire designs. However, these problems may be overcome by using Tikhonov regularization [43], first proposed in the context of coil design by Carlson [44], to generate coil designs through an inductance minimization constraint.

In the years since these methods were first proposed, a vast number of pseudo-analytical design methods were formulated for a variety of coil geometries based on either a continuous current flow or its streamfunction representation. These geometries include, but are not limited to, symmetric and asymmetric planar [45–47], cylindrical [48, 49], spherical and hemispherical [50], and toroidal [51].

These methods incorporate many different objectives other than field fidelity, such as minimum power [52], self-shielding [53], and multi-region field generation [54]. They all, however, revolve around current bases, symmetries within the system, and an optimization technique. First, a current basis is chosen such that specific components overlap with a particular coordinate system so that the system's Green's function can be decomposed appropriately. This way, simple expressions for the magnetic field can be written and calculated over a desired region efficiently. A numerical optimization procedure is then used to find the optimal selection of eigenfunctions and associated eigenvalues within the current basis. Usually, the system is cast into a least squares problem with a regularization term added to ensure that the problem is non-singular. The difference between the desired field and the field generated by the individual components of the current basis are calculated and the system is solved using a quadratic programming algorithm to find the globally optimal solution. If a continuum representation of the current is used the solution can then be discretized into individual wire patterns to generate an accurate physical representation of the optimal coil. Although elegant and computationally efficient, these methods require simple geometries to generate closed formed solutions in terms of standard functions and cannot be easily formulated for more complex situations.

2.2.3 Numerical Methods

The methods described above are all based around functional forms of the coil itself or the streamfunction predicating the current flow used to describe the global distribution. Pissanetzky [55] pioneered a method where the streamfunction's value is based around the local characterization of the current density on a surface geometry. This resulting formulation generated a geometry independent optimization scheme based around the minimization of a quadratic objective function [56], where the optimization of parameters such as field fi-

delity, power, wire curvature, and magnetic energy, may be taken into account. The formulation is based on the approximation of the streamfunction S, as the linear combination of linear basis functions $\varphi_n(\mathbf{r})$

$$S(\mathbf{r}) \approx \sum_{n=1}^{N} I_n \varphi_n(\mathbf{r}), \tag{2.23}$$

where N is the number of nodal points on the surface geometry with the unknown coefficient I_n. Applying the condition that the current is bound to a surface

$$\mathbf{J}(\mathbf{r}) = \nabla \wedge [S(\mathbf{r})\,\mathbf{n}(\mathbf{r})], \tag{2.24}$$

where $\mathbf{n}(\mathbf{r})$ is the outwards normal at some point $\mathbf{r}$ on the surface, and combining (2.23) and (2.24) results in

$$\mathbf{J}(\mathbf{r}) \approx \sum_{n=1}^{N} I_n \nabla \wedge [\varphi_n(\mathbf{r})\,\mathbf{n}(\mathbf{r})] = \sum_{n=1}^{N} I_n \mathbf{f}_n(\mathbf{r}). \tag{2.25}$$

The mathematical formalism in formulating an expression for the basis function, $\mathbf{f}_n(\mathbf{r})$, relies on the discretization of the surface geometry into a triangular mesh, defining a normalized edge current formed from the opposite edge of a given node in the mesh. The basis function $\mathbf{f}_n$ is then defined by

$$\mathbf{f}_n(\mathbf{r}) = \mathbf{v}_{ni} = \frac{\mathbf{e}_{ni}}{2A_{ni}} \qquad \text{if} \quad \mathbf{r} \in \Delta_{ni}, \tag{2.26}$$

where A_{ni} is the area of the i^{th} triangle with the n^{th} node, where $\mathbf{e}_{ni}$ is the vector defined by the edge opposite to the node n, selecting a specific direction in which the current is circulating around a node (clockwise or anti-clockwise) (see Fig.2.3). In this description, the computation of many surface integrals over the triangle must be calculated. These integrals, usually computed by numerical procedures, result in long computational times but may be approximated by summations to allow a more efficient optimization scheme. This does, however, result in a potential source of error.

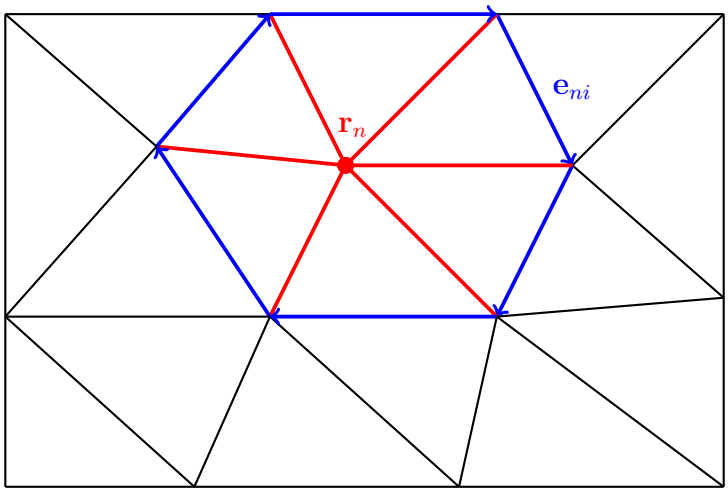


Figure 2.3: *Graphical representation of the edge current* $\mathbf{e}_{ni}$ *associated with the node at* $\mathbf{r}_n$.

Ludwig [57] expanded on the method which was then combined with a 3D contouring algorithm by Poole [58], that allowed the calculation of wire positions on an arbitrary surface. This formalism provided an efficient optimization scheme for accurate MRI gradient coil design and demonstrated a significant development for the design of coils with arbitrary geometries. This software was then successfully applied to shielded head gradient coils with an asymmetric geometry, bi-planar coils, and head gradient coils with shoulder cut-outs.

2.3 Mathematical Optimization Used in Magnetic Field Design

As seen in the previous section, optimization methods have been utilized to enhance the performance of electromagnetic systems to meet the required technical specifications. Many attributes need to be optimized within magnetic field design, such as power, inductance, and magnetic energy. However, the main objective is to generate a specific magnetic field profile within the desired accuracy. Due to the technological advances of computers and the accessibility of code, optimization techniques can be easily implemented to find optimal configurations of these complicated electromagnetic systems.

At the core of optimization is the mathematical-based selection of a set of variables that satisfy specific criteria. Generally speaking, optimization techniques apply a particular algorithm to a specific problem that allows the best solution to be found efficiently. These optimization algorithms and their applicability have been an area of intense research for decades, originating in mathematics, but now being applied to computer science, physics, engineering, and economics problems. Many of these problems revolve around either the maximization or minimization of one or many objective functions subjected to system constraints. An objective function can depend on many variables resulting in a complicated optimization landscape with many maxima and minima. These maxima and minima can be separated into local and globally optimal solutions. The local optima are the best solutions in the neighborhood of points, and the global optimum is the best solution out of every point.

Here, two optimization sub-classes are considered, quadratic programming [56] and multi-objective optimization [59], which are used to find these optima within magnetic field design methods.

Quadratic programming focuses on a single objective function utilizing iterative-based methods that use classical convergence-based algorithms that calculate the derivative, Hessian, or use the objective function to find more optimal solutions progressively. Examples of these optimization methods include interior point [60] or gradient descent methods [61]. These methods are well documented and researched, allowing the effective search of non-linear problems and successful convergence on optimal solutions. They can, however, be slow and unnecessarily computationally expensive.

Multi-objective optimization methods use heuristic techniques that allow the efficient computation of approximate solutions to be found for complex problems [62]. These methods are typically used when there are multiple objective functions and traditional approaches fail to find an optimal solution in a reasonable amount of time. Some examples of heuristic methods include particle swarm optimization [63], simulated annealing [64], and genetic algorithms

[65]. These methods take inspiration from biological and physical processes that efficiently traverse the multidimensional optimization hyperspace to find approximately optimal solutions. These methods, although extremely useful, do not guarantee an optimal solution and trade accuracy for computational speed.

2.3.1 Quadratic Programming

Quadratic programming encompasses the specific class of optimization techniques that are used when dealing with quadratic functions [56]. The generalized form of quadratic programming is such that there exists some square n-dimensional real symmetric matrix M and n-dimensional vector $\mathbf{v}$ which is minimized by the variable, $\mathbf{x}$,

$$\min_{\mathbf{x}} \mathbf{x}^T M \mathbf{x} + \mathbf{v}^T \mathbf{x}, \tag{2.27}$$

subject to m constraints where C is an n by m matrix and $\mathbf{d}$ is an m-dimensional real vector

$$C\mathbf{x} \leq \mathbf{d}. \tag{2.28}$$

For the magnetic field problems considered here, this quadratic programming problem takes the simplified form of a least squares optimization. The objective function in this case depends on the difference between the desired magnetic field, $\mathbf{B}^{\text{des}}(\mathbf{r_k})$, and magnetic field generated, $\mathbf{B}(\mathbf{r_k})$, by a current density, $\mathbf{J}(\mathbf{r}')$, at a specific set of preselected points, $\mathbf{r_k}$

$$\Phi = \sum_k \left(\frac{\mathbf{B}(\mathbf{r_k}) - \mathbf{B}(\mathbf{r_k})^{\text{des}}}{\mathbf{B}(\mathbf{r_k})^{\text{des}}} \right)^2. \tag{2.29}$$

For quadratic optimization to be used effectively the magnetic field must be linearly dependent on a set of adjustable parameters, A_i, such that

$$\mathbf{B}(\mathbf{r_k}) = \sum_i A_i \mathbf{b_i}(\mathbf{r_k}). \tag{2.30}$$

This is only possible if the specific contribution $\mathbf{b_i}(\mathbf{r_k})$ is predetermined for every i^{th} component. Therefore, the geometry and position of the current density must be preselected. The current must be decomposed into a current basis where A_i dictates the magnitude of current through the predetermined elements. This basis can take many forms, such as discrete loops, triangular elements on a discretized surface geometry, or a Fourier series describing a current flow. This problem, however, is ill-conditioned if multiple solutions could generate a specific field over a discrete finite number of points. In this case, a geometry-dependent constraint on the current density can be used to find a unique solution. This constraint takes the form of Tikhonov regularization, which, within electromagnetic systems, can be the power, inductance, or magnetic energy. They all, however, achieve the same outcome. If the regularization term is relatively large, the final design is well-conditioned and yields simplistic current flows with reduced field accuracy. Conversely, if the regularization term is small, the inverse problem is less well-conditioned and results in a more complex field pattern with increased field accuracy. The final objective function, using (2.29) and (2.30) with the addition of a regularization term which is quadratically dependent on the coil geometry, can be written as

$$\Phi = \alpha \sum_k \left(\mathbf{B}(\mathbf{r_k}) - \sum_i A_i \mathbf{b_i}(\mathbf{r_k}) \right)^2 + \beta \sum_i A_i^2 D_i, \tag{2.31}$$

where D_i is some geometry dependent parameter, and α and β are scaling parameters such that the objective function is dimensionless. In this instance, since the problem is purely quadratic, the solutions can be found easily by

taking the derivative with respect to A_j and setting it equal to zero

$$\frac{d\Phi}{dA_j} = -2\alpha \sum_k \mathbf{b_j}(\mathbf{r_k}) \left(\mathbf{B}(\mathbf{r_k}) - \sum_i A_i \mathbf{b_i}(\mathbf{r_k}) \right) + 2\beta \sum_i A_i \delta_{ij} D_i = 0, \quad (2.32)$$

where the optimal values A_i can be found through some iterative-based method or matrix inversion

$$A_i = \alpha \sum_k \mathbf{b_j}(\mathbf{r_k}) \mathbf{B}(\mathbf{r_k}) \left(\alpha \sum_k \mathbf{b_j}(\mathbf{r_k}) \mathbf{b_i}(\mathbf{r_k}) + \beta \delta_{ij} D_i \right)^{-1}, \quad (2.33)$$

if the matrix is sufficiently small. Depending on the formulation of the problem, further steps may be necessary to transform the final solution into a physical wire design such as the approximation of a surface current density to a discrete winding pattern.

2.3.2 Multi-objective Optimization

Multi-objective optimization [59] focuses on the techniques and algorithms that can simultaneously maximize or minimize N objective functions

$$\min_{\mathbf{x}} \left(f_1(\mathbf{x}), f_2(\mathbf{x}), \ldots, f_N(\mathbf{x}) \right). \quad (2.34)$$

These objective functions often conflict with each other, meaning the optimal solution exists on an N-dimensional surface called a Pareto front. A Pareto optimal solution is one that cannot improve an objective function without the deterioration of others. Due to the complexity of these multi-objective problems, standard iterative methods fail at finding optimal solutions in reasonable amounts of time. Therefore, more sophisticated methods that can traverse the optimization landscape need to be employed. These methods take a more practical approach to finding solutions, with many of the methods using multiple start points. These start points are then iterated. The method by which the progressive solutions are iterated depends on the technique used.

One method typically used to solve multi-objective optimization problems is a genetic algorithm [65]. Genetic algorithms are stochastic biologically-based search methods motivated by natural processes. The iterative algorithm is inspired by Darwinian survival of the fittest, where an initial population is evolved towards a better solution. This evolution is controlled by mutation, crossover, and selection functions, determining how the next generation is chosen. The solutions which have performed the best out of the initial population are selected to become parents within the next generation. These parent solutions then have their attributes combined, through the crossover function, to seed the remainder of the population. A certain amount of randomness is introduced through the mutation function to maintain genetic diversity and enable local optima within a problem to be circumvented.

These genetic algorithms are very good at finding high-quality solutions to multi-objective problems that vary non-linearly on the system parameters. However, they are most effective when the system depends on few variables. This form of optimization can be beneficial within electromagnetics since the analytical form of magnetic field profiles can be highly non-linear. An example of where this method could be used is the optimal selection of discrete coil positions. For example, the standard anti-Helmholtz configuration can be improved through the addition of multiple loops. Using (2.19) a set of N pairs of symmetrically placed loops of radius ρ_c at position d_i would generate an axial magnetic field on axis

$$B_z(z) = \frac{\mu_0 I \rho_c^2}{2} \sum_i^N \left(\frac{1}{\left[\rho_c^2 + (z - d_i)^2\right]^{\frac{3}{2}}} - \frac{1}{\left[\rho_c^2 + (z + d_i)^2\right]^{\frac{3}{2}}} \right). \tag{2.35}$$

The axial field can be expanded about the origin using a Taylor's expansion and polynomial field variation can be determined in terms of the coil parameters. Here, a genetic algorithm could be used to find optimal wire placements where the objective functions are the first $\tilde{N}$ unwanted polynomial variations in the

magnetic field

$$\begin{cases} \min f_1(d_i, \ldots, d_N) = \frac{d^3 B_z(z)}{dz^3} \\ \qquad\qquad \vdots \\ \min f_{\tilde{N}}(d_i, \ldots, d_N) = \frac{d^{2\tilde{N}+1} B_z(z)}{dz^{2\tilde{N}+1}}. \end{cases} \tag{2.36}$$

This system could be further developed by introducing a turn ratio, I_i, at each axial position d_i. However, this becomes slightly more complicated as an integer constraint on I_i must be added.

Another algorithm that could solve this problem efficiently would be a particle swarm method. Within this method, the movement of biological systems such as a flock of birds or school of fish is represented as a mathematical search method where the movement of each solution in the optimization landscape is affected by the local best known position around them. Using this method, the trial solutions are expected to 'swarm' around the best solution. Analysis of the difference between these two search methods has been explored, with some scenarios being better suited to one algorithm over the other. However, the way each method traverses the optimization hyperspace is not well understood [66].

The methods described here all facilitate the optimization of electromagnetic systems. However, they all rely on an accurate model of the physical system. Hence, to be able to design magnetic fields within shielded environments the shielding mechanism needs to be understood.

2.4 Magnetic Field Design in Magnetic Shields

Low-frequency magnetic shielding has been an active research area for many years. This interest originated from the need to shield internal circuitry from external radio frequency interference [67]. Through the progression of technology and the increasing use of magnetically sensitive equipment, low magnetic field environments are now critical in the functionality of devices used in

medical imaging [68], geophysical mapping [69], precision timing [70], particle accelerators [71] and many, many, more areas of application. Usually, shielding material is used to reduce quasi-static magnetic fields, altering the magnetic field's spatial distribution and diverting areas of high magnetic field variation away from designated regions.

Materials shield low-frequency magnetic fields through two mechanisms, flux-shunting and eddy current cancellation. Flux-shunting is the result of Ampere's and Gauss's laws requiring the continuity of the tangential and perpendicular components of the magnetic field strength and flux density, respectively, across a surface interface, S, resulting in the boundary conditions

$$\left(\frac{1}{\mu_r}\mathbf{B}_{\text{mat.}} - \mathbf{B}_{\text{air}}\right) \wedge \hat{\mathbf{n}} = 0 \qquad \text{on } S, \tag{2.37}$$

and

$$(\mathbf{B}_{\text{mat.}} - \mathbf{B}_{\text{air}}) \cdot \hat{\mathbf{n}} = 0 \qquad \text{on } S, \tag{2.38}$$

respectively, where $\hat{\mathbf{n}}$ is the unit vector normal to the boundary and μ_r is the relative permeability of the material. For materials with very large permeability, the magnetic field, in air, parallel to the interface's surface is practically non-existent, and the field is 'shunted' into the material. The material acts as a low resistance pathway for magnetic field lines diverting the magnetic field into the shield and away from any enclosed region. On the other hand, the eddy current mechanism occurs only with the existence of time-varying fields. As a result of Faraday's law, an electric field is induced within the material when it is subjected to time-varying magnetic fields. This electric field, in turn, results in an induced current density dictated by Ohm's law, opposing the incident field where the magnitude of the response is related to the conductivity of the material [72].

Magnetic shields play an instrumental role in generating precisely controlled magnetic field environments and are necessary to remove external interference from a system. This process is usually achieved using multiple shielding layers,

resulting in a cumbersome and immobile experiment. If further field cancellation or field generation is required within the shield, this can be accounted for by an internal active current system. However, the active field cannot be accurately generated using standard design methods performed in free space. This inaccuracy is caused by the same mechanisms that shield enclosed regions from external magnetic fields, affecting the generation of magnetic fields within the shield.

The magnetic shield's effect on the magnetic field generated by a current source can be numerically calculated using forward finite element methods [73]. However, these simulations are computationally intensive and cannot efficiently be utilized in forward optimization methods unless the initial trial solution is near-optimal. Due to the complexity of the problem, no general method exists to optimize active structures within materials efficiently and must be investigated on a case-by-case basis.

Design methods that take the magnetic shield into account have been formulated for a variety of very specific situations. These methods are highly situational and depend on the geometry and material of the shield and the frequency domain of the desired actively generated field. The two main shielding geometries used within systems today are cubic and cylindrical due to their simple construction and shielding efficiency. Due to the symmetries within cubic and cylindrical shields, simplified analytical formulations for the governing partial differential equations (PDEs) of the systems can be written. These, however, are very difficult to solve generally in 3D and only simple analytical expressions for loops and pseudo-3D shields of infinite extent can be found [72]. Approximate solutions in 3D have been found in the limiting cases for high-frequency fields within a shield with high-conductivity and low-permeability, and quasi-static fields within high-permeability shields, with boundary conditions

$$\mathbf{B}(\mathbf{r})_{\perp} \approx 0 \quad \text{on } S, \tag{2.39}$$

$$\mathbf{B}(\mathbf{r})_{\parallel} \approx 0 \quad \text{on } S, \tag{2.40}$$

where the dominant mechanisms are eddy current and flux shunting, respectively. The limits to which the material's response is considered perfect depends on the propagation constant, γ, of a given material, which is related to the complete time-dependent solution of the vector potential

$$\nabla^2 \mathbf{A} - \gamma^2 \mathbf{A} = 0, \tag{2.41}$$

where

$$\gamma = \sqrt{i\omega\mu_0\mu_r(\sigma + i\omega\epsilon_0\epsilon_r)}, \tag{2.42}$$

in a material and zero in free space, where σ and ϵ_r are conductivity and relative permittivity of the material, respectively, where ω is the frequency of the magnetic field. For a good conductor, $\omega\epsilon_0\epsilon_r \ll \sigma$, γ can be simplified to

$$\gamma = (1+i)\sqrt{\frac{\omega\mu_0\mu_r\sigma}{2}} = \frac{1+i}{\delta}, \tag{2.43}$$

where δ is the skin depth of the material. For the high frequency and conductivity regime, the perfect conducting response

$$\mathbf{B}(\mathbf{r})_{\perp} = 0 \quad \text{on } S, \tag{2.44}$$

is valid when the thickness of the shield, Δ, is much greater than the skin depth, $\frac{\Delta}{\delta} \gg 1$, and the majority of the time varying field is reflected. The opposite is true for the low-frequency high-permeability regime where the perfect magnetic response

$$\mathbf{B}(\mathbf{r})_{\parallel} = 0 \quad \text{on } S, \tag{2.45}$$

is valid when the permeability is very large, $\mu \gg 1$ and the skin depth is much greater than the thickness of the material, $\frac{\delta}{\Delta} \gg 1$ i.e. the eddy current response is almost zero.

For cubic geometries, the shield's approximate responses in the perfect cases are found through the method of mirror images [37]. The magnetic field interior to the magnetic shield is calculated by generating image currents that ensure the magnetic field satisfies the boundary conditions (2.44) and (2.45). In the quasi-static high-permeability case, the image current positions are mirrored about the planar surfaces such that their combined parallel components along the boundary are eliminated. This response is opposite to the high frequency and conductivity case where the positions are mirrored and current directions flipped, removing all perpendicular components. Within a cubic shield, infinitely many images are generated using the method of mirror images in 3D, where the current source and its images are reflected about each planar surface. Both perfect cases are depicted in Fig. 2.4. The method of mirror images has since been used to design accurate bi-planar and discrete coils, generating quasi-static fields in high-permeability shields effectively [74].

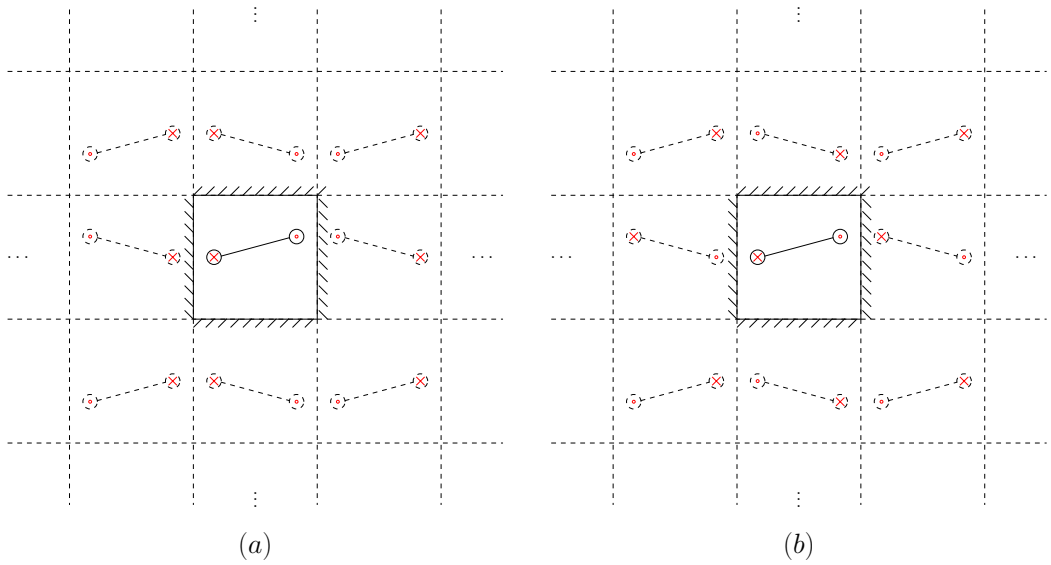


Figure 2.4: *Schematic diagram showing the method of mirror images for a 2D slice for an arbitrary current source in (a) perfect magnetic conductor and (b) perfect electric conductor. Black circles show cross-sections of wires carrying current into (red crosses) and out of (red circles) the page. The initial currents are reflected about the hatched black lines to satisfy the perfect boundary conditions.*

In cylindrical geometries, these limiting cases are approximately solved using Green's function methods. Turner [75] first decomposed the Green's function in cylindrical coordinates for a perfectly conducting cylinder and a cylindrical

current source. The perfect conducting cylinder's response was cast in terms of an induced current on the surface of an infinite cylindrical shield. The magnetic field generated by both the source and shield was then calculated and matched at the shield's boundary, enabling the induced current to be found in terms of the initial current source. The field and optimal placement of simple discrete loops were then analyzed to improve these shielded coil systems. This cylindrical decomposition method then allowed the solution for static magnetic fields to be found within infinitely long shields of arbitrary permeability, which was used in the analysis of simple discrete coil structures [76].

Further methods that include closed finite-length cylinders have also been developed, using an exact Green's function solutions for a perfect magnetic conducting finite-length cylinder [77] and, in the finite-permeability case, using the Green's function for an infinite cylinder combined with the method of mirror images [78]. However, these are limited to specific cases of magnetically-shielded solenoids and discrete current loops. Currently, no analytical method exists that allows the calculation of arbitrary coils within cylindrical magnetic shields.

Numerical boundary element methods have been recently developed to optimize magnetic fields generated by surface currents on a triangular mesh that incorporates high-permeability boundaries [79, 80]. These methods utilized the formulation proposed by Poole [58] with the addition of an equipotential scalar field to enforce the perfect boundary condition on the surface of a topologically closed shield. A quadratic optimization procedure is then used to find coil designs that account for the perfect magnetic conductor. However, this numerical method is limited by computational power as the solution's accuracy can be mesh-dependent if the distance between the coil and shield is small compared to the mesh size. This numerical method is, nevertheless, very powerful, allowing complicated hybrid systems to be developed without designing geometry-specific methods.

Analytical coil design methods within magnetic shields are advantageous in

many geometrically simple situations. They provide an accurate, fast, and efficient route to calculate the magnetic field. They give intuition on the shield's response, allowing for a more fundamental understanding of the interaction mechanisms. They also provide flexibility in designing magnetic fields with either a discrete geometry or continuum current density. Due to these reasons, within the following three publication style chapters, three quasi-static magnetic field design methods in high-permeability cylindrical magnetic shields are presented. Due to the problem formulation and method used to satisfy the boundary conditions, the chapters are thematically similar. For completeness, each publication begins with the formulation of the boundary conditions for a high-permeability shield; these chapters then diverge, solving the problem in their specific cases. In reality, due to the work's similarity, these publications should be considered parts 1, 2, and 3 of a larger publication. However, as the work has been conducted over a prolonged period, these publications have been separated into three standalone pieces of work.

Chapter 3

Optimal Inverse Design of Magnetic Field Profiles in a Magnetically Shielded Cylinder

Optimal Inverse Design of Magnetic Field Profiles in a Magnetically Shielded Cylinder

M. Packer,[1] P.J. Hobson,[1] N. Holmes,[2] J. Leggett,[2] P. Glover,[2] M.J. Brookes,[2] R. Bowtell,[2] and T.M. Fromhold[1,*]

[1] *School of Physics and Astronomy, University of Nottingham, Nottingham NG7 2RD, United Kingdom*

[2] *Sir Peter Mansfield Imaging Centre, School of Physics and Astronomy, University of Nottingham, Nottingham NG7 2RD, United Kingdom*

(Received 8 June 2020; revised 10 September 2020; accepted 10 September 2020; published 3 November 2020)

Magnetic shields that use both active and passive components to enable the generation of a tailored low-field environment are required for many applications in science, engineering, and medical imaging. Until now, accurate field nulling, or field generation, has only been possible over a small fraction of the overall volume of the shield. This is due to the interaction between the active field-generating components and the surrounding high-permeability passive shielding material. In this paper, we formulate the interaction between an arbitrary static current flow on a cylinder and an exterior closed high-permeability cylinder. We modify the Green's function for the magnetic vector potential and match boundary conditions on the shield's interior surface to calculate the total magnetic field generated by the system. We cast this formulation into an inverse optimization problem to design active–passive magnetic field shaping systems that accurately generate any physical static magnetic field in the interior of a closed cylindrical passive shield. We illustrate this method by designing hybrid systems that generate a range of magnetic field profiles to high accuracy over large interior volumes, and simulate them in real-world shields whose passive components have finite permeability, thickness, and axial entry holes. Our optimization procedure can be adapted to design active–passive magnetic field shaping systems that accurately generate any physical user-specified static magnetic field in the interior of a closed cylindrical shield of any length, enabling the development and miniaturization of systems that require accurate magnetic shielding and control.

DOI: 10.1103/PhysRevApplied.14.054004

I. INTRODUCTION

Regions of space that require precisely controlled magnetic field environments are essential for a wide range of experiments, devices, and applications. These include quantum sensing of gravity and gravity gradients for geophysical survey and mapping [1–4]; atomic magnetometry [5–7] for applications including material characterization [8] and magnetoencephalography [9,10]; noise reduction in fundamental physics experiments [11,12] such as timing using high-precision atomic clocks [13,14], measuring the electric dipole moment of fundamental systems [15–18], and testing Lorentz invariance by observing the limits of spin precession [19–21]. Typically, these systems are enclosed within high-permeability materials, such as mumetal, to shield magnetically sensitive components from undesired magnetic fields. Cylindrical geometries, in particular, are widely used due to their comparatively high shielding factor relative to their low manufacturing cost [22–24].

Romeo and Hoult first laid the mathematical framework for the design of magnetic fields in free space through the use of current loops and arcs [25]. These simple elements were expanded in a spherical harmonic basis and unwanted field profiles removed by adjusting the relative separations of the discrete coils. Inverse methods based on formulating a current density in terms of simple triangular boundary elements [26–28] enabled the design of coils of arbitrary complexity, giving greater flexibility in the design of systems at the cost of computational power and numerical instability. Pseudoanalytical formulations using a Green's function expansion and harmonic minimization methods have been developed to generate accurate user-specified magnetic fields in free space [29–31] to facilitate the need for fast and accurate design procedures. However, these methods did not incorporate the interaction of the high-permeability passive shielding material, hindering the accurate generation of specified target magnetic field profiles [32] in shielded environments. Consequently, optimization of magnetic field cancelation, or other field shaping, systems in the presence of a material with high magnetic permeability is a long-standing challenge in electromagnetism.

*mark.fromhold@nottingham.ac.uk

 © 2020 American Physical Society

Finite element methods (FEMs) can be used to develop models of hybridized active and passive shielding systems. One method of optimizing active–passive systems using FEMs would be to use genetic algorithms [33,34] to evolve the coil parameters iteratively, including the effect of the passive material on the magnetic field generated actively at each iteration. Because of their computational complexity, however, FEMs can be slow, and, if coupled with forward optimization procedures provide only locally optimal designs since desired magnetic field profiles depend highly nonlinearly on the system parameters. Analytical formulations of the magnetic field generated by hybrid active–passive systems have the distinct advantage that optimal solutions can be calculated at a range of target points with minimal computation [35]. Currently, analytical solutions for coils in high-permeability cylindrical magnetic shields have only been formulated in the specific cases of magnetically shielded solenoids and discrete current loops [36–38]. The geometric parameters of the active structure in these systems, such as the separation distances of wire loops, are adapted to account for the interaction between the active and passive systems. Previously, the method of mirror images [39] has been used to formulate the response of a planar material with high magnetic permeability to a magnetic field generated by a current source [40–43]. In these formulations, Maxwell's equations are solved explicitly by including the reflections of the current source generated by the high-permeability material in order to match the required boundary conditions. More generally, Green's function solutions to boundary value problems have been calculated for an extensive range of electromagnetic systems [44], but have not previously been found generally for the case of a finite closed cylindrical high-permeability shield in the presence of an arbitrary cylindrical coaxial static current source.

To address this, here, we incorporate *ab initio* the effect of a finite length high-permeability cylinder on the magnetic field generated by an arbitrary static current flow on a conducting cylinder, and use our results to determine the flow required to generate specified static target fields optimally. This enables the geometry of the active components on the surface of a cylinder to be determined entirely from a desired magnetic field profile. Guided by previous work [45], we first derive the Green's function for a hybrid active–passive field-generating system described in cylindrical coordinates. We then utilize a modified Fourier basis to define an adjusted current density distribution that accounts for the effect of the high-permeability material. From this, we determine globally optimal current density maps using a quadratic optimization procedure, akin to magnetic field design methodologies used previously in magnetic resonance imaging (MRI) [46,47]. To construct practical current sources from these current density maps, we define the streamfunction of the current continuum and discretize it into a set of closed-loop current-carrying wire geometries. Using this formulation, we present two example coil designs optimized in the interior of a closed cylindrical magnetic shield of finite length and high permeability, $\mu_r \gg 1$, and show that our analytical model agrees well with FEM simulations performed for the optimized current flow patterns. We then show that our design methodology can be used in a real-world situation where the cylindrical magnetic shield has finite thickness and permeability as well as axial entry holes in the end caps to allow experimental access. Using this formulation, we transform the performance of systems designed to generate user-specified magnetic field profiles in the magnetostatic regime, finding globally optimal solutions required for practical, low size, weight, power, and cost technologies for the applications listed above.

II. THEORY

The interface conditions for a magnetic field along a boundary S between two materials are that the normal component of the magnetic field $\mathbf{B}$ and tangential component of the magnetic field strength $\mathbf{H}$ are continuous. Considering the boundary between air and a material, working in the magnetostatic regime, where no eddy currents are induced, and in the case where no surface currents are present, these interface conditions are

$$(\mathbf{B}_{\text{mat.}} - \mathbf{B}_{\text{air}}) \cdot \hat{\mathbf{n}} = 0 \quad \text{on } S \tag{1}$$

and

$$\left(\frac{1}{\mu_r}\mathbf{B}_{\text{mat.}} - \mathbf{B}_{\text{air}}\right) \wedge \hat{\mathbf{n}} = 0 \quad \text{on } S, \tag{2}$$

where $\hat{\mathbf{n}}$ is the unit vector normal to the boundary and μ_r is the relative permeability of the material. In free space, the magnetic field is related to the magnetic field strength and the magnetization $\mathbf{M}$ by

$$\mathbf{B} = \mu_0(\mathbf{H} + \mathbf{M}). \tag{3}$$

Physically, the magnetization of the subdomains of a material change in response to an applied magnetic field to satisfy boundary condition (2) at the material's surface. Here, we choose to formulate this response in terms of a pseudocurrent density $\widetilde{\mathbf{J}}$ confined to the surface of the material, which relates to the curl of the magnetization,

$$\nabla \wedge \mathbf{M} = \widetilde{\mathbf{J}}. \tag{4}$$

The magnetic field strength resulting from a current source $\mathbf{J_c}$ can be expressed using Ampère's law

$$\nabla \wedge \mathbf{H} = \mathbf{J_c}. \tag{5}$$

Substituting Eqs. (4) and (5) into the curl of Eq. (3), noting that $\mathbf{B} = \nabla \wedge \mathbf{A}$, where $\mathbf{A}$ is the vector potential, results in

the Poisson equation in free space

$$\nabla^2 \mathbf{A} = -\mu_0(\mathbf{J_c} + \widetilde{\mathbf{J}}). \tag{6}$$

As shown in many papers and textbooks [39], the solution to the Poisson equation, for an arbitrary current density $\mathbf{J}$ is given by

$$\mathbf{A}(\mathbf{r}) = \mu_0 \int_{r'} d^3\mathbf{r}'\, G(\mathbf{r}, \mathbf{r}')\mathbf{J}(\mathbf{r}'), \tag{7}$$

where $G(\mathbf{r}, \mathbf{r}')$ is the associated Green's function.

Let us now use the boundary condition on the magnetic field, Eq. (2), to examine the effect of a high-permeability material on the magnetic field generated by a specific current distribution. Consider a hollow high-permeability, $\mu_r \to \infty$, cylinder of radius ρ_s, length L_s, and thickness d with high-permeability planar end caps located at $z = \pm L_s/2$ that is surrounded by free space (Fig. 1). An arbitrary static current flows over an internal open coaxial cylinder of radius $\rho_c < \rho_s$ and length $L_1 - L_2 = L_c < L_s$, where $-L_s/2 < L_2 < L_1 < L_s/2$, as shown in Fig. 1. Since high-permeability materials, such as mumetal, can have μ_r values greater than 100 000 times that of air, the magnetic field must abruptly change direction at the boundary between its surface and air to satisfy boundary conditions (1)–(2). When the shield is of sufficient thickness and permeability, the tangential components of the magnetic field at its boundary must be approximately zero. Boundary condition (2) on the interior surface of the exterior closed cylinder for the example depicted in Fig. 1 requires that

$$B_\rho\Big|_{z=\pm L_s/2} \approx 0, \quad B_\phi\Big|_{z=\pm L_s/2, \rho=\rho_s} \approx 0, \quad B_z\Big|_{\rho=\rho_s} \approx 0, \tag{8}$$

where the magnetic field $\mathbf{B} = B_\rho\hat{\boldsymbol{\rho}} + B_\phi\hat{\boldsymbol{\phi}} + B_z\hat{\mathbf{z}}$ is expressed in cylindrical polar coordinates. Previously, it has been found that the response of a high-permeability material deviates from that of a perfect magnetic conductor on the scale of $\mathcal{O}(\mu_r^{-1})$ [48,49]. Therefore, we may assume that, for high-permeability materials, such as mumetal, the response can be approximated to that of a perfect magnetic conductor without introducing significant errors.

Because of the symmetries of the system, it is natural to work in cylindrical coordinates. Following the formulation of Turner [45], we express vector potential (7) due to an arbitrary current distribution $\mathbf{J} = J_\rho(\mathbf{r}')\hat{\boldsymbol{\rho}} + J_\phi(\mathbf{r}')\hat{\boldsymbol{\phi}} + J_z(\mathbf{r}')\hat{\mathbf{z}}$ as

$$A_\rho(\mathbf{r}) = \mu_0 \int_{r'} d^3\mathbf{r}'\, G(\mathbf{r}, \mathbf{r}')[J_\rho(\mathbf{r}')\cos(\phi - \phi') + J_\phi(\mathbf{r}')\sin(\phi - \phi')], \tag{9}$$

$$A_\phi(\mathbf{r}) = -\mu_0 \int_{r'} d^3\mathbf{r}'\, G(\mathbf{r}, \mathbf{r}')[J_\rho(\mathbf{r}')\sin(\phi - \phi') - J_\phi(\mathbf{r}')\cos(\phi - \phi')], \tag{10}$$

$$A_z(\mathbf{r}) = \mu_0 \int_{r'} d^3\mathbf{r}'\, G(\mathbf{r}, \mathbf{r}')J_z(\mathbf{r}'). \tag{11}$$

Since the current has been restricted to flow over an interior cylindrical shell centered radially about the origin, its radial components may be set to zero, resulting in the simplified vector potentials

$$A_\rho(\mathbf{r}) = \mu_0 \int_{r'} d^3\mathbf{r}'\, G(\mathbf{r}, \mathbf{r}')J_\phi(\mathbf{r}')\sin(\phi - \phi'), \tag{12}$$

$$A_\phi(\mathbf{r}) = \mu_0 \int_{r'} d^3\mathbf{r}'\, G(\mathbf{r}, \mathbf{r}')J_\phi(\mathbf{r}')\cos(\phi - \phi'). \tag{13}$$

Substituting the Green's function solution from Eq. (7) in cylindrical coordinates [39],

$$G(\mathbf{r}, \mathbf{r}') = \frac{1}{4\pi^2}\sum_{m=-\infty}^{\infty} e^{im(\phi-\phi')} \int_{-\infty}^{\infty} dk\, e^{ik(z-z')} I_m(|k|\rho_<)K_m(|k|\rho_>), \tag{14}$$

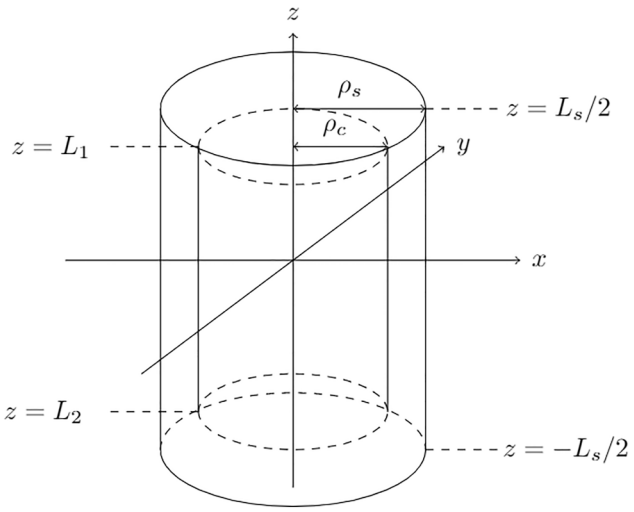


FIG. 1. Schematic diagram showing a high magnetic permeability cylinder of length L_s and radius ρ_s with planar end caps located at $z = \pm L_s/2$. This cylinder encloses an interior conducting open cylindrical shell of length $L_c = L_1 - L_2$ and radius ρ_c.

into Eqs. (11)–(13), the components of the vector potential may be expressed as

$$A_\rho(\rho,\phi,z) = -\frac{i\mu_0\rho'}{4\pi}\sum_{m=-\infty}^{\infty}\int_{-\infty}^{\infty} dk\, e^{im\phi}e^{ikz} \times [I_{m-1}(|k|\rho_<)K_{m-1}(|k|\rho_>) - I_{m+1}(|k|\rho_<)K_{m+1}(|k|\rho_>)]J_\phi^m(k), \quad (15)$$

$$A_\phi(\rho,\phi,z) = \frac{\mu_0\rho'}{4\pi}\sum_{m=-\infty}^{\infty}\int_{-\infty}^{\infty} dk\, e^{im\phi}e^{ikz} \times [I_{m-1}(|k|\rho_<)K_{m-1}(|k|\rho_>) + I_{m+1}(|k|\rho_<)K_{m+1}(|k|\rho_>)]J_\phi^m(k), \quad (16)$$

$$A_z(\rho,\phi,z) = \frac{\mu_0\rho'}{2\pi}\sum_{m=-\infty}^{\infty}\int_{-\infty}^{\infty} dk\, e^{im\phi}e^{ikz} \times I_m(|k|\rho_<)K_m(|k|\rho_>)J_z^m(k), \quad (17)$$

where ρ' is the radius of the cylinder and $\rho_>, \rho_<$ is either ρ, ρ' if $\rho > \rho'$ or ρ', ρ if $\rho < \rho'$. Equations (15)–(17) contain Fourier transforms of the current densities,

$$J_\phi^m(k) = \frac{1}{2\pi}\int_0^{2\pi} d\phi'\, e^{-im\phi'}\int_{-\infty}^{\infty} dz'\, e^{-ikz'}J_\phi(\phi',z'), \quad (18)$$

$$J_z^m(k) = \frac{1}{2\pi}\int_0^{2\pi} d\phi'\, e^{-im\phi'}\int_{-\infty}^{\infty} dz'\, e^{-ikz'}J_z(\phi',z'), \quad (19)$$

with their corresponding inverse transforms given by

$$J_\phi(\phi',z') = \frac{1}{2\pi}\sum_{m=-\infty}^{\infty}\int_{-\infty}^{\infty} dk\, e^{im\phi'}e^{ikz'}J_\phi^m(k), \quad (20)$$

$$J_z(\phi',z') = \frac{1}{2\pi}\sum_{m=-\infty}^{\infty}\int_{-\infty}^{\infty} dk\, e^{im\phi'}e^{ikz'}J_z^m(k). \quad (21)$$

As a result of this formulation, we can now combine methods for matching the boundary conditions at the radial interface, akin to the formulation of passive screening of magnetic field gradients for MRI [50], with the method of mirror images, accounting for the effect of the planar end caps, to determine the effect of the high-permeability material on the overall magnetic field profile. Because of the cylindrical symmetry of the system, the radial boundary condition may be satisfied by matching the azimuthal Fourier modes in the magnetic field, generated by the cylindrical current source, through the use of a pseudocurrent density induced on an infinite cylinder. As the planar end caps are spatially orthogonal to the pseudocurrent generated by the infinite cylinder, any image current formed by applying the method of mirror images continues to satisfy the radial boundary condition. Consequently, we can decouple the boundary conditions on the high-permeability cylinder and at the planar end cap boundaries. This must be done sequentially to generate mirror images of the pseudocurrent density induced on the high-permeability cylindrical shell and, hence, satisfy the boundary conditions over the entire domain of the closed finite high-permeability cylinder. As a result, using Eqs. (15)–(17) and the usual formulation of the method of mirror images with two infinite parallel planes, depicted in Fig. 2, the vector potential in the region $\rho_c \le \rho \le \rho_s$, including the effect of the high-permeability cylinder, may be written in terms of an infinite summation over the reflected image currents,

$$A_\rho(\rho,\phi,z) = -\frac{i\mu_0}{4\pi}\sum_{m=-\infty}^{\infty}\sum_{p=-\infty}^{\infty}\int_{-\infty}^{\infty} dk\, e^{im\phi}e^{ikz} \times \{\rho_c[I_{m-1}(|k|\rho_c)K_{m-1}(|k|\rho) - I_{m+1}(|k|\rho_c)K_{m+1}(|k|\rho)]J_\phi^{mp}(k) + \rho_s[I_{m-1}(|k|\rho)K_{m-1}(|k|\rho_s) - I_{m+1}(|k|\rho)K_{m+1}(|k|\rho_s)]\widetilde{J_\phi^{mp}}(k)\}, \quad (22)$$

$$A_\phi(\rho,\phi,z) = \frac{\mu_0}{4\pi}\sum_{m=-\infty}^{\infty}\sum_{p=-\infty}^{\infty}\int_{-\infty}^{\infty} dk\, e^{im\phi}e^{ikz} \times \{\rho_c[I_{m-1}(|k|\rho_c)K_{m-1}(|k|\rho) + I_{m+1}(|k|\rho_c)K_{m+1}(|k|\rho)]J_\phi^{mp}(k) + \rho_s[I_{m-1}(|k|\rho)K_{m-1}(|k|\rho_s) + I_{m+1}(|k|\rho)K_{m+1}(|k|\rho_s)]\widetilde{J_\phi^{mp}}(k)\}, \quad (23)$$

$$A_z(\rho,\phi,z) = \frac{\mu_0}{2\pi}\sum_{m=-\infty}^{\infty}\sum_{p=-\infty}^{\infty}\int_{-\infty}^{\infty} dk\, e^{im\phi}e^{ikz} \times [\rho_c I_m(|k|\rho_c)K_m(|k|\rho)J_z^{mp}(k) + \rho_s I_m(|k|\rho)K_m(|k|\rho_s)\widetilde{J_z^{mp}}(k)], \quad (24)$$

where

$$J_\phi^{mp}(k) = \frac{1}{2\pi}\int_0^{2\pi} d\phi'\, e^{-im\phi'}\int_{-\infty}^{\infty} dz'\, e^{-ikz'}J_\phi^p(\phi',z'), \quad (25)$$

$$J_z^{mp}(k) = \frac{1}{2\pi}\int_0^{2\pi} d\phi'\, e^{-im\phi'}\int_{-\infty}^{\infty} dz'\, e^{-ikz'}J_z^p(\phi',z') \quad (26)$$

are the Fourier transforms of the pth reflected image current and $\widetilde{J^{mp}_{\phi,z}}(k)$ is the Fourier transform of the pth reflected pseudocurrent induced on the high-permeability cylinder. In Fig. 2 we depict how azimuthal, $J^p_\phi(\phi', z')$, and axial, $J^p_z(\phi', z')$, image currents are generated by two parallel planar perfect magnetic conductors.

Writing the magnetic field in cylindrical coordinates,

$$\mathbf{B} = \nabla \wedge \mathbf{A} = \left(\frac{1}{\rho}\frac{\partial A_z}{\partial \phi} - \frac{\partial A_\phi}{\partial z}\right)\hat{\boldsymbol{\rho}} + \left(\frac{\partial A_\rho}{\partial z} - \frac{\partial A_z}{\partial \rho}\right)\hat{\boldsymbol{\phi}} + \frac{1}{\rho}\left(\frac{\partial}{\partial \rho}(\rho A_\phi) - \frac{\partial A_\rho}{\partial \phi}\right)\hat{\mathbf{z}}, \tag{27}$$

boundary conditions (8) on the magnetic field at $\rho = \rho_s$ are

$$\frac{1}{\rho}\left(\frac{\partial}{\partial \rho}(\rho A_\phi) - \frac{\partial A_\rho}{\partial \phi}\right)\Big|_{\rho=\rho_s} = 0, \tag{28}$$

$$\left(\frac{\partial A_\rho}{\partial z} - \frac{\partial A_z}{\partial \rho}\right)\Big|_{\rho=\rho_s} = 0. \tag{29}$$

Substituting Eqs. (22)–(24) into Eqs. (28)–(29), the Fourier transformed pseudocurrent density on the cylindrical wall of the high-permeability cylinder is found to be

$$\widetilde{J^{mp}_{\phi,z}}(k) = -\frac{\rho_c I'_m(|k|\rho_c)K_m(|k|\rho_s)}{\rho_s I_m(|k|\rho_s)K'_m(|k|\rho_s)} J^{mp}_{\phi,z}(k), \tag{30}$$

where $I'_m(z)$ and $K'_m(z)$ are the derivatives with respect to z of $I_m(z)$ and $K_m(z)$, respectively. Using the continuity equation, Eqs. (20)–(24), and Eq. (30), the magnetic field interior to the conducting cylinder, for all points $\rho < \rho_c$, is given by

$$B_\rho(\rho, \phi, z) = \frac{i\mu_0\rho_c}{2\pi}\sum_{m=-\infty}^{\infty}\sum_{p=-\infty}^{\infty}\int_{-\infty}^{\infty} dk\, k e^{im\phi} e^{ikz} \times I'_m(|k|\rho)R_m(k, \rho_c, \rho_s)J^{mp}_\phi(k), \tag{31}$$

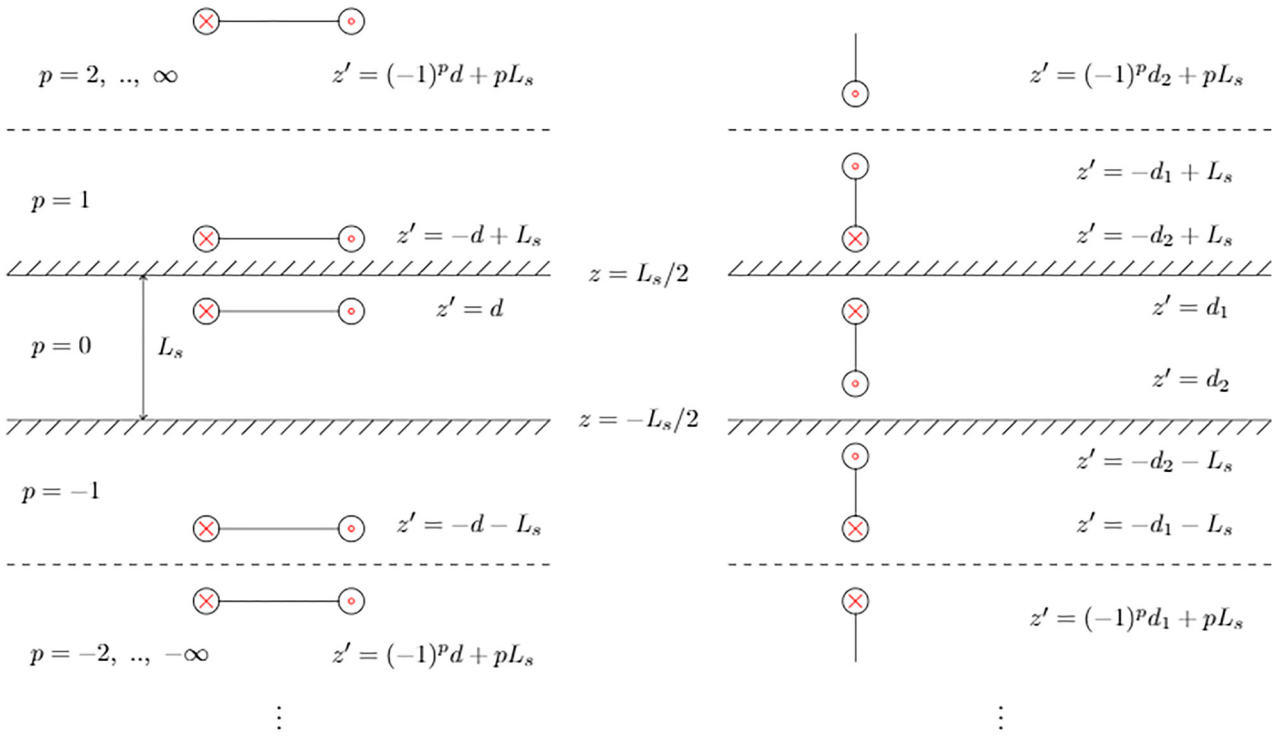


FIG. 2. Schematic diagram showing how azimuthal (left) and axial (right) currents are reflected by two infinite parallel planes (hatched) of infinite extension and permeability (i.e., perfect magnetic conductors) located at $z = \pm L_s/2$. Left: Azimuthal currents located in the $z' = d$ plane are translated, by the reflection process, to the $z' = (-1)^p d + pL_s$ planes. Right: Axial currents flowing from $z' = d_1$ to $z' = d_2$ are reflected to positions $z' = (-1)^p d_1 + pL_s$ and $z' = (-1)^p d_2 + pL_s$, respectively, with odd reflections reversing the initial current flow direction. Black circles show cross sections of wires carrying current into (red crosses) and out of (red circles) the page.

$$B_\phi(\rho,\phi,z) = -\frac{\mu_0\rho_c}{2\pi\rho}\sum_{m=-\infty}^{\infty}\sum_{p=-\infty}^{\infty}\int_{-\infty}^{\infty} dk\, m\frac{|k|}{k}e^{im\phi}e^{ikz} \times I_m(|k|\rho)R_m(k,\rho_c,\rho_s)J_\phi^{mp}(k), \quad (32)$$

$$B_z(\rho,\phi,z) = -\frac{\mu_0\rho_c}{2\pi}\sum_{m=-\infty}^{\infty}\sum_{p=-\infty}^{\infty}\int_{-\infty}^{\infty} dk\, |k|e^{im\phi}e^{ikz} \times I_m(|k|\rho)R_m(k,\rho_c,\rho_s)J_\phi^{mp}(k), \quad (33)$$

where $R_m(k,\rho_c,\rho_s) = K_m'(|k|\rho_c) - I_m'(|k|\rho_c)K_m(|k|\rho_s)/I_m(|k|\rho_s)$. In order to determine the magnetic field generated by an arbitrary cylindrical current source, we must construct an orthogonal basis defined on a finite cylinder, which accounts for the mirror images. To this end, we use a modified Fourier basis, defining the pth reflected azimuthal current to be

$$J_\phi^p(\phi',z') = [T_e^p(z';L_1,L_2,L_s) + T_o^p(z';L_1,L_2,L_s)] \times\left\{\sum_{n=1}^{N} W_{n0}\sin\left(\frac{n\pi[(-1)^p(z'-pL_s)-L_2]}{L_c}\right) + \sum_{n=1}^{N}\sum_{m=1}^{M}[W_{nm}\cos(m\phi') + Q_{nm}\sin(m\phi')] \times\cos\left(\frac{n\pi[(-1)^p(z'-pL_s)-L_2]}{L_c}\right)\right\}, \quad (34)$$

in which

$$T_e^p(z';L_1,L_2,L_s) = [H(z'-L_2-pL_s) - H(z'-L_1-pL_s)]\frac{1+(-1)^p}{2}, \quad (35)$$

$$T_o^p(z';L_1,L_2,L_s) = [H(z'+L_1-pL_s) - H(z'+L_2-pL_s)]\frac{1-(-1)^p}{2}, \quad (36)$$

where $H(x)$ is the Heaviside function and (W_{n0},W_{nm},Q_{nm}) are Fourier coefficients to be determined. Substituting Eq. (34) into Eqs. (31)–(33), we derive a set of governing equations that relate the magnetic field to the set of weighted Fourier coefficients,

$$B_\rho(\rho,\phi,z) = \sum_{n=1}^{N} W_{n0}F_n(\rho,z) + \sum_{n=1}^{N}\sum_{m=1}^{M}[W_{nm}G_{nm}^w(\rho,\phi,z) + Q_{nm}G_{nm}^q(\rho,\phi,z)], \quad (37)$$

$$B_\phi(\rho,\phi,z) = \sum_{n=1}^{N}\sum_{m=1}^{M}[W_{nm}H_{nm}^w(\rho,\phi,z) + Q_{nm}H_{nm}^q(\rho,\phi,z)], \quad (38)$$

$$B_z(\rho,\phi,z) = \sum_{n=1}^{N} W_{n0}D_n(\rho,z) + \sum_{n=1}^{N}\sum_{m=1}^{M}[W_{nm}S_{nm}^w(\rho,\phi,z) + Q_{nm}S_{nm}^q(\rho,\phi,z)], \quad (39)$$

where the functions $F_n(\rho,z)$, $G_{nm}^{w,q}(\rho,\phi,z)$, $H_{nm}^{w,q}(\rho,\phi,z)$, $D_n(\rho,z)$, and $S_{nm}^{w,q}(\rho,\phi,z)$ are defined in Appendix A. Having determined the magnetic field produced by an arbitrary cylindrical current, we may now use an inverse method to solve the system of governing equations, Eqs. (37)–(39), to determine the unknown Fourier coefficients (W_{n0},W_{nm},Q_{nm}) for a specified target magnetic field. Following work done by Carlson *et al.* [46], this may be done by a least-squares minimization with the addition of a penalty term to regularize the problem. This regularization term may take many forms, with individual contributions to it representing, for example, the curvature of a given wire geometry, the power consumption, or any other physical parameter that depends quadratically on the geometry of the coil. In this work we focus on the overall power dissipated in the cylindrical current flow, but this choice is somewhat arbitrary since all of the regularization parameters act to achieve the same general goal. If the regularization term is large, the result is a well-conditioned inverse problem that yields a simple current flow, but reduced field fidelity. On the other hand, if the regularization term is small then the result is a less well-conditioned inverse problem that yields a more intricate pattern of current flow but a higher-fidelity magnetic field. The power dissipation in the conducting cylinder of thickness t and resistivity ϱ is given by

$$P = \frac{\rho_c\varrho}{t}\int_{L_2}^{L_1} dz'\int_0^{2\pi} d\phi'\, |J_z(\phi',z')|^2 + |J_\phi(\phi',z')|^2, \quad (40)$$

which, when integrated over the surface of the cylinder, using the continuity equation and Eq. (34), gives

$$P = \frac{\rho_c\varrho}{t}\left[\sum_{n=1}^{N} W_{n0}^2\pi L_c + \sum_{n=1}^{N}\sum_{m=1}^{M}(W_{nm}^2+Q_{nm}^2) \times\left(\frac{\pi L_c}{2} + \frac{m^2L_c^3}{2\pi n^2\rho_c^2}\right)\right]. \quad (41)$$

We now construct a cost function using a least-squares optimization procedure,

$$\Phi = \sum_k[\mathbf{B}^{\text{desired}}(\mathbf{r}_k) - \mathbf{B}(\mathbf{r}_k)]^2 + \beta P, \quad (42)$$

evaluated at K target field points, where β is a weighting parameter chosen such that the physical parameters may be adjusted to achieve specified physical constraints. The minimization is achieved by taking the derivative of the cost function with respect to the Fourier coefficients,

$$\frac{\partial \Phi}{\partial W_{i0}} = 0, \qquad \frac{\partial \Phi}{\partial W_{ij}} = 0, \qquad \frac{\partial \Phi}{\partial Q_{ij}} = 0, \qquad i,j > 1, \tag{43}$$

allowing the optimal Fourier coefficients to be found by matrix inversion for any physically attainable target magnetic field. The current density is then related, through the continuity equation, to the streamfunction

$$\begin{aligned}\varphi(\phi', z') = {} & [H(z' - L_1) - H(z' - L_2)] \\ & \times \left\{ \sum_{n=1}^{N} \frac{L_c}{n\pi} W_{n0} \cos\left(\frac{n\pi (z' - L_2)}{L_c}\right) \right. \\ & - \sum_{n=1}^{N} \sum_{m=1}^{M} \frac{L_c}{n\pi} [W_{nm} \cos(m\phi') \\ & \left. + Q_{nm} \sin(m\phi')] \sin\left(\frac{n\pi (z' - L_2)}{L_c}\right) \right\}, \end{aligned} \tag{44}$$

on the inner conducting cylindrical surface.

Ideally, the Fourier series would have an infinite number of coefficients. However, truncating the series at a large finite number of terms still provides accurate solutions for sufficiently regularized problems. This is because higher-order terms contribute less at distances much larger than their spatial period. When designing fields in regions close to the conducting surface, if a sufficiently large number of coefficients is chosen, the real-world field fidelity is limited by the accuracy to which the current continuum can be approximated by discretized wire configurations, rather than by the number of Fourier coefficients. Typically, setting $N = 200$ and equating M to the degree of the desired field harmonic is adequate. An approximate solution to the current continuum is then found by discretizing the streamfunction into N_φ values, where $\varphi_j = \min \varphi + (j - 1/2)\Delta\varphi$, $j = 1, \ldots, N_\varphi$, separated by $\Delta\varphi = (\max \varphi - \min \varphi)/N_\varphi$. The number of contours should be maximized according to the constraints in manufacturing because the accuracy of the model depends on the approximation of the continuum. For situations where only coarse discretization is possible, we recommend that a form of discrete optimization is used instead. When physically manufacturing these structures, the distance of the wires from the high-permeability material is important. Without the passive shield, one can determine how accurately the discrete coil represents the current continuum by using the elemental Biot-Savart law to calculate the error as N_φ is adjusted.

III. RESULTS

We now analyze our theoretical model by designing and testing hybrid active–passive magnetic field-generating systems. Regarding the validation of our calculations, we first note that, as expected from previous work [36–38] and shown in Appendix B, our calculations confirm that the optimal coil design for generating a constant axial field inside a closed cylindrical perfect magnetic shield is a perfect solenoid that runs along the full length of the cylindrical shield.

In Figs. 3 and 4 we respectively show active–passive systems for generating a constant transverse field B_x normal to the axis of the cylinder, and a linear transverse field gradient $\mathbf{B} = (z\hat{\mathbf{x}} + x\hat{\mathbf{z}})$ along the axis of the cylinder. Each of these systems has a cylindrical surface of length $L_c = 0.95$ m and radius $\rho_c = 0.245$ m, which carries the coil current distribution. This current distribution is interior to and centered about the origin of a closed perfect magnetically conducting cylinder of length $L_s = 1$ m and radius $\rho_s = 0.25$ m. The field is optimized over the central cylindrical region spanning half the radius and length of the coil cylinder. In Figs. 3(a) and 4(a) we show the respective streamfunctions on the surface of the cylinder and their discretization into wire patterns. The magnetic fields shown in Figs. 3(b)–3(c) and 4(b) are calculated in three ways: analytically, using our theoretical model in Eqs. (37)–(39); numerically, using COMSOL Multiphysics® with the shield treated as a perfect magnetic conductor; and numerically in free space, i.e., excluding the high-permeability material and calculating the magnetic fields by applying the elemental Biot-Savart law directly to the discrete coil geometries in Figs. 3(a) and 4(a). It is clear from Figs. 3–4 that our design methodology is capable of generating highly accurate user-specified target magnetic fields inside the optimized field region with good agreement between the theoretical model and numerical simulations.

We quantify this agreement by analyzing the deviation from the target fields in the optimization region, ΔB_x and $\Delta dB_x/dz$, for the constant transverse field and linear transverse field gradient systems, respectively. Specifically, along the z axis of the optimized region the maximum absolute deviations from the target fields are 0.11% and 0.24%, respectively. Over the same region, the maximum absolute deviations between the numerically simulated and analytically calculated field profiles are 0.002% and 0.003%, respectively. We can also see the hybrid nature of our optimization by the improved performance of the active systems when inside, and coupled to, the passive shield. For example, the strength of the B_x field is nearly doubled, and its uniformity is improved by a factor of 20, when the high-permeability cylinder is added to the constant transverse field-generating system [see Fig. 3(b)].

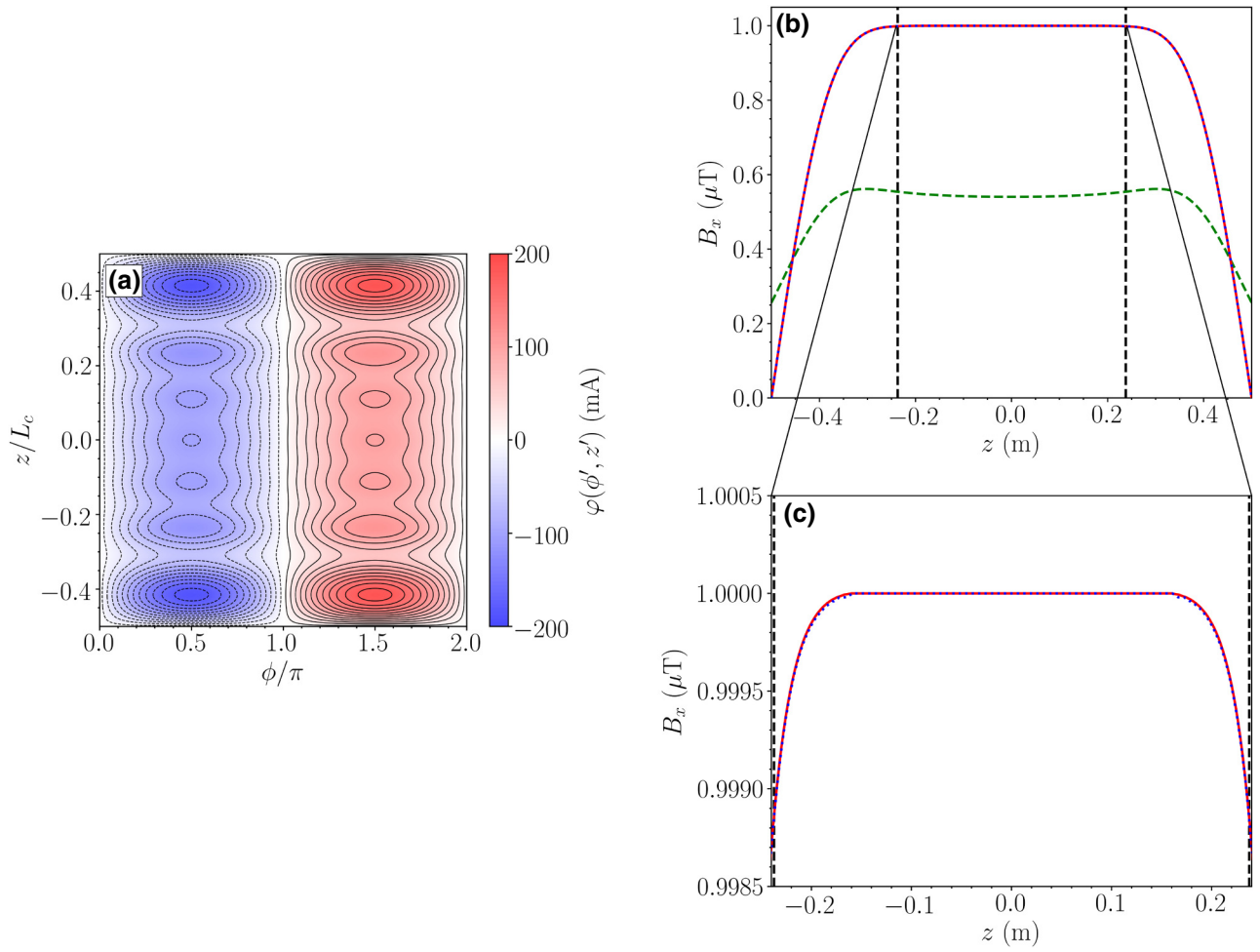


FIG. 3. Wire layouts (a) and performance (b),(c) of an optimized hybrid active–passive constant transverse field-generating system in which current flows on a cylinder of length $L_c = 0.95$ m and radius $\rho_c = 0.245$ m. The wire layouts are optimized to generate a constant transverse field, $B_x = 1$ μT, across the cylinder and normal to its axis of symmetry. The current-carrying cylinder is placed symmetrically inside a perfect closed magnetic shield of length $L_s = 1$ m and radius $\rho_s = 0.25$ m and the magnetic field is optimized between $\rho = [0, \rho_c/2]$ and $z = \pm L_c/4$; see the dashed black lines in (b),(c). The least-squares optimization is performed with parameters $N = 200$, $M = 1$, and $\beta = 5.95 \times 10^{-12}$. (a) Color map of the optimal current streamfunction on the cylinder [blue and red shaded regions correspond to the flow of current in opposite senses and their intensity shows the streamfunction magnitude from low (white) to high (intense color)]. Solid and dashed black curves represent discrete wires with opposite senses of current flow, approximating the current continuum with $N_\varphi = 24$ contour levels. (b) Transverse magnetic field B_x versus axial position z calculated from the current continuum in (a) in three ways: analytically using Eqs. (37)–(39) (solid red curve); numerically using COMSOL Multiphysics version 5.3a and modeling the high-permeability cylinder as a perfect magnetic conductor (blue dotted curve); numerically *without* the high-permeability cylinder and using the Biot-Savart law with $N_\varphi = 100$ contour levels (dashed green). (c) Enlarged section of (b) emphasizing the high level of field uniformity and the agreement between the numerical and analytical results over the optimization region.

In Fig. 5 we show the numerically calculated color maps of the B_x field in the y-z plane generated by the constant transverse field [Fig. 3(a)] and linear transverse field gradient [Fig. 4(a)] systems, using COMSOL Multiphysics with the shield treated as a perfect magnetic conductor. We summarize the performance of both systems in Table I, calculating the cylindrical shield fractions—the ratio of the radial and axial extents of the central region to that of the passive shield—where the maximum deviations from the target fields are less than 0.01%, 0.05%, 0.1%, 0.5%, 1%, and 5%.

When physically constructing active–passive structures for real-world experiments, additional limitations must be taken into consideration in order to generate accurate magnetic fields using our design methodology. These limitations originate either from the theoretical model itself or from experimental practicalities. The limitations in the theoretical model are primarily associated with

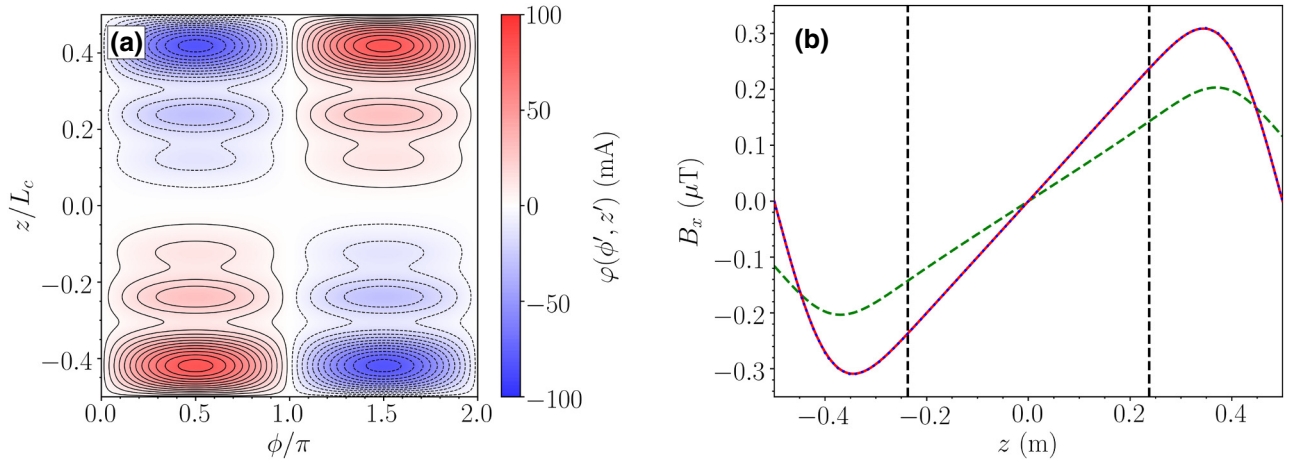


FIG. 4. Wire layouts (a) and performance (b) of an optimized hybrid active–passive linear transverse gradient field-generating system in which current flows on a cylinder of length $L_c = 0.95$ m and radius $\rho_c = 0.245$ m. The wire layouts are optimized to generate a linear transverse field gradient, $dB_x/dz = 1$ μT/m, along the z axis of the cylinder. The current-carrying cylinder is placed symmetrically inside a perfect closed magnetic shield of length $L_s = 1$ m and radius $\rho_s = 0.25$ m and the magnetic field is optimized between $\rho = [0, \rho_c/2]$ and $z = \pm L_c/4$; see the dashed black lines in (b). The least-squares optimization is performed with parameters $N = 200$, $M = 1$, and $\beta = 5.95 \times 10^{-12}$. (a) Color map of the optimal current streamfunction on the cylinder [blue and red shaded regions correspond to the flow of current in opposite senses and their intensity shows the streamfunction magnitude from low (white) to high (intense color)]. Solid and dashed black curves represent discrete wires with opposite senses of current flow, approximating the current continuum with $N_\varphi = 24$ contour levels. (b) Transverse magnetic field B_x versus axial position z calculated from the current continuum in (a) in three ways: analytically using Eqs. (37)–(39) (solid red curve); numerically using COMSOL Multiphysics version 5.3a and modeling the high-permeability cylinder as a perfect magnetic conductor (blue dotted curve); numerically *without* the high-permeability cylinder and using the Biot-Savart law with $N_\varphi = 100$ contour levels (dashed green).

how accurately the high-permeability cylinder approximates a perfect magnetic conductor. This depends on the value of the finite permeability, the thickness of the shielding material, and the required experimental access holes in the shielding system. The errors introduced by these parameters depend on the lengths, radii, and positions of the conducting and high-permeability cylinders relative to the location of the optimization region. The experimental limitations on the field fidelity relate to the stability of the experimental equipment and errors in

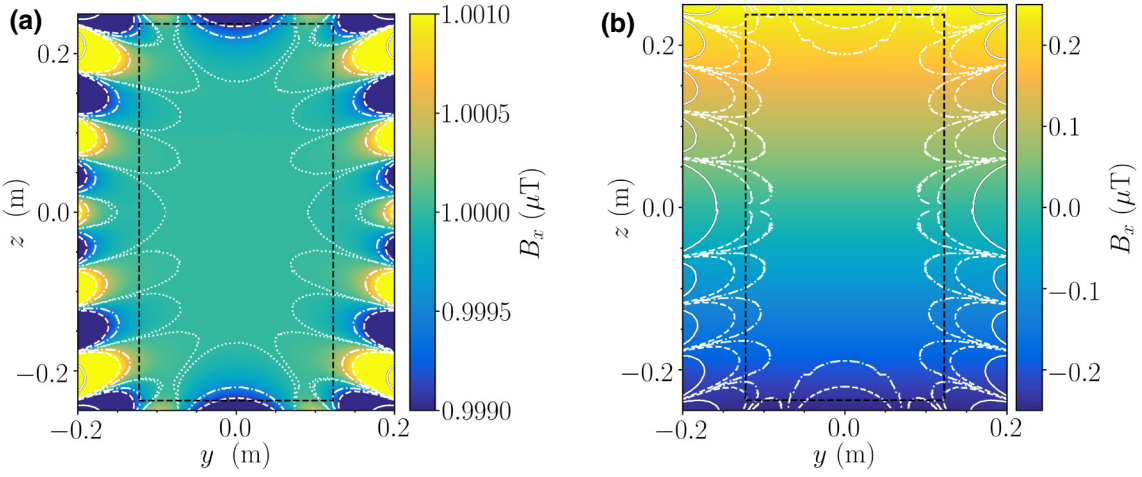


FIG. 5. Color maps showing the magnitude of the transverse magnetic field B_x in the y-z plane inside a closed finite length perfect magnetic conductor generated by two active–passive systems: (a) the constant transverse field-generating system depicted in Fig. 3; (b) the linear transverse gradient field-generating system depicted in Fig. 4. The field profiles are calculated numerically using COMSOL Multiphysics version 5.3a. Contours show where the field deviates from the target field by 1% (solid curves), 0.1% (dashed curves), 0.01% (dash–dot curves), and 0.001% (dotted curves; in (a) only).

TABLE I. Cylindrical shield fractions—defined as the ratio of the radius and length of the central region to those of the passive shield—where the maximum magnetic field deviations are within 0.01%, 0.05%, 0.1%, 0.5%, 1%, and 5% of the target fields generated by the constant transverse, B_x, and linear transverse gradient, dB_x/dz, systems, depicted in Figs. 3(a) and 4(a), respectively. The magnetic field deviations are calculated numerically using COMSOL Multiphysics version 5.3a in two ways: inside a perfect magnetic conductor (perfect case); inside a magnetic shield with finite permeability $\mu_r = 20\,000$, thickness $d = 1$ mm, and a circular entry hole of normalized radius $\rho_h = 0.25\rho_s$ in both end caps (imperfect case).

	Cylindrical shield fraction			
	Perfect		Imperfect	
Maximum field deviation (%)	B_x	dB_x/dz	B_x	dB_x/dz
0.01	0.320	0.237	0.190	0.168
0.05	0.398	0.315	0.350	0.268
0.1	0.437	0.348	0.442	0.320
0.5	0.472	0.448	0.474	0.440
1	0.496	0.470	0.499	0.470
5	0.598	0.553	0.598	0.551

manufacturing an accurate representation of the current continuum. These errors include coarse discretization of the current continuum, inexact wire placement and construction, and imprecise positioning of the active structure inside the high-permeability shield. In practice, highly stable experimental equipment is available, particularly power supplies and current drivers [51], and it is possible to manufacture structures that approximate the current continuum accurately [45]. Consequently, the error introduced in the formulation of our model must be calculated to determine the accuracy of any future potential designs in a real-world experimental setup. Our active–passive systems must, therefore, be analyzed for the case of a high-permeability cylinder that is not a closed perfect magnetic conductor. To do this, we use COMSOL Multiphysics working in the magnetostatic regime, to determine how the uniformity of the B_x field generated by the constant transverse field-generating system in Fig. 3(a) changes when the perfect closed magnetic conductor is replaced by one that is imperfect. To construct an imperfect shield, we define the magnetic permeability $\mu_r = 20\,000$ to match the permeability of industrial standard mumetal regularly used as a passive shield. We then vary the wall thickness d of a closed magnetic shield and determine how small d can be while maintaining high field uniformity. Finally, using this minimum thickness, we introduce a circular axial entry hole of radius ρ_h at the center of each end cap and determine how large the hole can be to preserve field uniformity.

We use the root-mean-square (rms) field deviation $\Delta B_x^{\rm rms}$ of the attained field from the uniform target field, calculated along the z axis of the optimized field region,

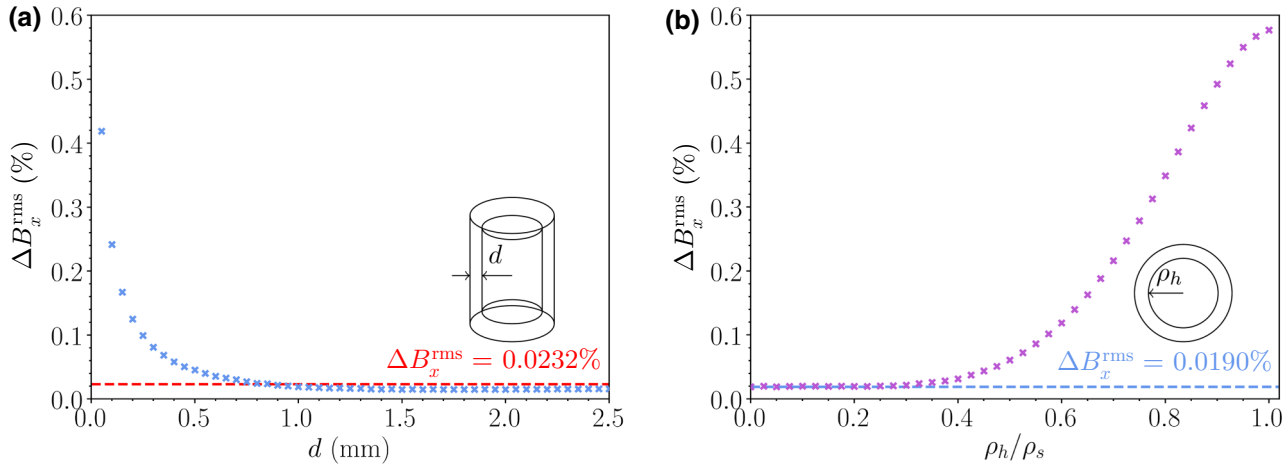


FIG. 6. Plots showing how the performance of the optimized hybrid active–passive constant transverse field-generating system depicted in Fig. 3 depends (a) on the thickness d of the high-permeability cylinder (inset), and (b) on the radius ρ_h of the circular axial entry hole in the two end caps (inset), which allow access to the interior of the system. (a) Root-mean-square deviation $\Delta B_x^{\rm rms}$ evaluated along the axis of the optimized field region, as a function of the high-permeability shield thickness d, taking $\mu_r = 20\,000$ and $\rho_h = 0$. Light blue crosses show $\Delta B_x^{\rm rms}$ values calculated numerically from the current continuum in Fig. 3(a) using COMSOL Multiphysics version 5.3a. Horizontal dashed red line shows the analytical value of $\Delta B_x^{\rm rms} = 0.0232\%$ calculated using Eqs. (37)–(39). (b) Root-mean-square deviation $\Delta B_x^{\rm rms}$ evaluated along the axis of the optimized field region, as a function of the normalized axial hole radius ρ_h/ρ_s, taking $\mu_r = 20\,000$ and $d = 1$ mm. Purple crosses show $\Delta B_x^{\rm rms}$ values calculated numerically from the current continuum in Fig. 3(a) using COMSOL Multiphysics version 5.3a. For comparison, the horizontal dashed light blue line shows the numerical rms deviation $\Delta B_x^{\rm rms} = 0.0190\%$ calculated when $d = 1$ mm and $\rho_h = 0$.

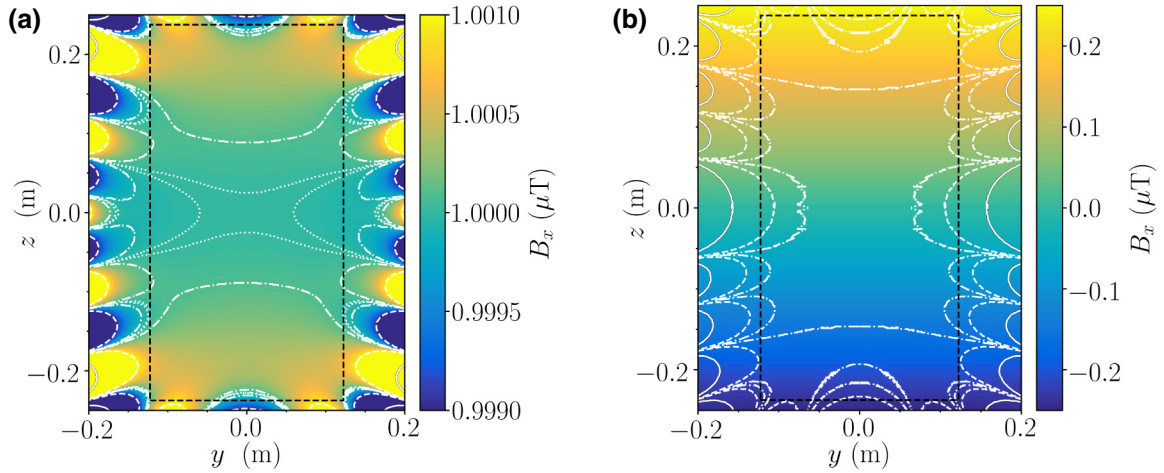


FIG. 7. Color maps showing the magnitude of the transverse magnetic field B_x in the y-z plane inside a magnetic shield with permeability $\mu_r = 20\,000$, thickness $d = 1$ mm, and a circular axial entry hole of normalized radius $\rho_h = 0.25\rho_s$ around the center of each end cap generated by two active–passive systems: (a) the constant transverse field-generating system depicted in Fig. 3; (b) the linear transverse gradient field-generating system depicted in Fig. 4. The field profiles are calculated numerically using COMSOL Multiphysics version 5.3a. Contours show where the field deviates from the target field by 1% (solid curves), 0.1% (dashed curves), 0.01% (dash–dot curves), and 0.001% (dotted curves; in (a) only).

to evaluate the performance of the active–passive system. The light blue crosses in Fig. 6(a) show that ΔB_x^{rms} values calculated numerically from the current continuum in Fig. 3(a) using COMSOL Multiphysics decrease as d increases in the range 0.05–2.5 mm with interval size 0.05 mm, converging to the *thick* material limit where the thickness is assumed to be infinite. The horizontal dashed red line shows the analytical value of $\Delta B_x^{\text{rms}} = 0.0232\%$ calculated using Eqs. (37)–(39). The numerical ΔB_x^{rms} values decrease asymptotically below this analytical limit and approach the difference $\mathcal{O}(\mu_r^{-1}) \approx 0.005\%$ [48,49] that we predicted for our model in Sec. II. This intrinsic error, resulting from the small difference between *thick* high-permeability materials and a perfect magnetic conductor, sets the hard limit on the accuracy of any magnetic field that can by designed using our theoretical model. In reality, however, this limit is so small that, for a thick material with a high permeability, such as mumetal, the errors in manufacturing and construction will be much more significant. As technologies advance that reduce these system errors, such as screen-printed foldable printed circuit boards [52] and three-dimensional printing technologies [53], it may become more relevant to develop a model that accounts *ab initio* for magnetic shields of finite permeability and thickness.

We see from Fig. 6(a) that the asymptotic limit is reached at approximately $d = 1$ mm, where $\Delta B_x^{\text{rms}} = 0.019\%$. At this point, regarding the accuracy of our model, there is little advantage to increasing d further. Consequently, in Fig. 6(b) we take $d = 1$ mm and examine the effect of introducing circular axial entry holes in both end caps of the high-permeability cylinder. Although ΔB_x^{rms} increases as the hole radius ρ_h increases from no hole, $\rho_h = 0$, to when there is no end cap, $\rho_h = \rho_s$, we see that small holes in both end caps allow experimental access without significantly reducing the fidelity of the desired field profile. In particular, for our system, the hole radius can be made as large as $\rho_h = 0.25\rho_s$ while only increasing ΔB_x^{rms} by 0.0012% when compared to the no hole case (horizontal dashed light blue line).

In Fig. 7 we show the numerically calculated color maps of the B_x field in the y-z plane generated by the constant transverse field [Fig. 3(a)] and linear transverse field gradient [Fig. 4(a)] systems. Both of these systems are simulated with the same imperfect high-permeability cylindrical magnetic shield that has had its properties determined in the above analysis: $\mu_r = 20\,000$, $d = 1$ mm, and $\rho_h = 0.25\rho_s$. The performance of both systems in terms of the cylindrical shield fraction is summarized in Table I.

Finally, we see from Table I that this imperfect magnetic shield does not introduce significant magnetic field deviations above 0.1% when compared to a perfect shield with the same geometry. In particular, the maximum difference between the perfect and imperfect cylindrical shield fractions for deviations above 0.1% is only 0.028. Large deviations in the field accuracy below 0.1% can be graphically seen when comparing the color maps for the perfect (Fig. 5) and imperfect (Fig. 7) cases. The contours showing field deviations of 0.01% and 0.001% are strongly perturbed, as expected from the analysis in Fig. 6, demonstrating the *hard* intrinsic limit on our model when

generating target field profiles inside real-world magnetic shields. Similar analysis should be applied when designing other active–passive systems using our theoretical model in order to quantify its accuracy for a specific experimental setup. Further analysis could also be performed to determine the low-frequency limit in which a time-dependent current source could be included. However, if the magnitudes of any induced eddy currents are much less than the magnitude of the coil current, such effects will be negligible. Further designs generating more exotic field profiles can be found in Appendix C. All designs can be found in our open access PYTHON code that can be used to design systems to generate a specific physical target field using our model (see below for more details).

IV. CONCLUSION

In this paper, we develop an analytical model to calculate the total magnetic field generated by an arbitrary current flow on a cylinder that is coaxially nested within a finite closed high-permeability cylinder. We modify Green's function for the magnetic vector potential, match the radial and planar boundary conditions of the magnetic field through the introduction of a pseudocurrent density, and incorporate a harmonic minimization procedure to design optimal user-specified magnetic fields by using a modified cylindrical Fourier basis. We then verify this optimization procedure by designing coils to generate a constant transverse field B_x across the cylinder, and a linear transverse field gradient dB_x/dz along the length of the cylinder. Our analytical calculations of these field profiles agree well with numerical simulations. The optimization procedure generates highly accurate B_x and dB_x/dz field profiles, inside a high-permeability cylinder, with peak-to-peak deviations from the target profiles below 0.11% and 0.24%, respectively. The analytically predicted deviations agree with the numerical simulations to within 0.002% and 0.003% for the constant and linear gradient systems, respectively.

We further investigate the validity of our model by analyzing the behavior of the constant transverse field-generating system inside a magnetic shield of permeability $\mu_r = 20\,000$, finite thickness, and with circular axial entry holes in the end caps. We find a range of parameters where the analytical predictions for a perfect cylindrical magnetic conductor remain close to numerical simulations for a cylindrical shield with finite permeability and thickness that includes entry holes, showing that the designs generated by our model are applicable to real-world magnetic shields. Notably, when the active field-generating systems are enclosed by a passive magnetic shield with realistic experimental parameters ($\mu_r = 20\,000$, thickness 1 mm, and entry holes of radius equal to 25% of the shield's radius), the deviation from the desired constant and linear gradient field profiles are less than 0.1% and 0.5%, respectively, over more than 40% of the central radial and axial extents of this simulated real-world magnetic shield.

Our flexible optimization procedure enables the design of new active–passive magnetic field shaping systems to accurately generate any static magnetic field profile in the interior of a finite closed magnetic shield, subject to satisfying Maxwell's equations in free space and not saturating the shielding material. This facilitates the development and miniaturization of systems and technologies that require such control, including quantum sensors, fundamental physics experiments, and medical technologies. Further investigation could consider an analytical treatment of finite magnetic shield thickness and permeability and interactions with an open magnetic shield topology.

The PYTHON code used to design arbitrary cylindrical coils in a magnetically shielded cylinder is openly available from GitHub [54]. Verification using COMSOL Multiphysics requires a valid license.

ACKNOWLEDGMENTS

We acknowledge support from the UK Quantum Technology Hub Sensors and Timing, funded by the Engineering and Physical Sciences Research Council (EP/M013294/1).

The authors M.P., P.J.H., T.M.F., M.J.B., and R.B. declare that they have a patent pending to the UK Government Intellectual Property Office (Application No. 1913549.0) regarding the magnetic field optimization techniques described in this work. The authors have no other competing financial interests.

APPENDIX A: MATHEMATICAL DEFINITIONS

We have

$$F_n(\rho,z) = \sum_{p=-\infty}^{\infty} \int_{-\infty}^{\infty} dk\, I_0'(|k|\rho) \times \left(K_0'(|k|\rho_c) - \frac{I_0'(|k|\rho_c) K_0(|k|\rho_s)}{I_0(|k|\rho_s)} \right) C_{np}^1(k,z), \tag{A1}$$

$$G_{nm}(\rho,z) = \sum_{p=-\infty}^{\infty} \int_{-\infty}^{\infty} dk\, I_m'(|k|\rho) \times \left(K_m'(|k|\rho_c) - \frac{I_m'(|k|\rho_c) K_m(|k|\rho_s)}{I_m(|k|\rho_s)} \right) C_{np}^2(k,z), \tag{A2}$$

$$G^w_{nm}(\rho,\phi,z) = \cos(m\phi)G_{nm}(\rho,z),$$
$$G^q_{nm}(\rho,\phi,z) = \sin(m\phi)G_{nm}(\rho,z), \tag{A3}$$

$$H_{nm}(\rho,z) = \sum_{p=-\infty}^{\infty}\int_{-\infty}^{\infty} dk\, mI_m(|k|\rho) \times \left(K'_m(|k|\rho_c) - \frac{I'_m(|k|a)K_m(|k|\rho_s)}{I_m(|k|\rho_s)}\right)C^3_{np}(k,z), \tag{A4}$$

$$H^w_{nm}(\rho,\phi,z) = \sin(m\phi)H_{nm}(\rho,z),$$
$$H^q_{nm}(\rho,\phi,z) = -\cos(m\phi)H_{nm}(\rho,z), \tag{A5}$$

$$D_n(\rho,z) = \sum_{p=-\infty}^{\infty}\int_{-\infty}^{\infty} dk\, I_0(|k|\rho) \times \left(K'_0(|k|\rho_c) - \frac{I'_0(|k|\rho_c)K_0(|k|\rho_s)}{I_0(|k|\rho_s)}\right)C^4_{np}(k,z), \tag{A6}$$

$$S_{nm}(\rho,z) = \sum_{p=-\infty}^{\infty}\int_{-\infty}^{\infty} dk\, I_m(|k|\rho) \times \left(K'_m(|k|\rho_c) - \frac{I'_m(|k|\rho_c)K_m(|k|\rho_s)}{I_m(|k|\rho_s)}\right)C^5_{np}(k,z), \tag{A7}$$

$$S^w_{nm}(\rho,\phi,z) = \cos(m\phi)S_{nm}(\rho,z),$$
$$S^q_{nm}(\rho,\phi,z) = \sin(m\phi)S_{nm}(\rho,z), \tag{A8}$$

where

$$C^1_{np}(k,z) = i\mu_0\rho_c nL_c k e^{ik(z-pL_s)} \times \left(\frac{e^{-(-1)^p ikL_2} + (-1)^{n+1}e^{-(-1)^p ikL_1}}{n^2\pi^2 - L_c^2k^2}\right), \tag{A9}$$

$$C^2_{np}(k,z) = \frac{i(-1)^p L_c k}{n\pi}C^1_{np}(k,z), \tag{A10}$$

$$C^3_{np}(k,z) = -\frac{i(-1)^p L_c|k|}{n\pi k\rho}C^1_{np}(k,z), \tag{A11}$$

$$C^4_{np}(k,z) = \frac{i|k|}{k}C^1_{np}(k,z), \tag{A12}$$

$$C^5_{np}(k,z) = -\frac{(-1)^p L_c|k|}{n\pi}C^1_{np}(k,z). \tag{A13}$$

Performing the integrals over k by splitting up the odd and even terms in p while expressing the summation over the infinite pseudocurrent densities through a Fourier series expansion

$$\sum_{p=-\infty}^{\infty} e^{2ikpL_s} = \frac{\pi}{L_s}\sum_{p=-\infty}^{\infty}\delta\left(k - \frac{\pi p}{L_s}\right), \tag{A14}$$

we can simplify the expressions in Eqs. (A1), (A2), (A4), (A6), and (A7) as

$$F_n(\rho,z) = \sum_{p=-\infty}^{\infty} I'_0\left(\left|\frac{\pi p}{L_s}\right|\rho\right)\left[K'_0\left(\left|\frac{\pi p}{L_s}\right|\rho_c\right) - \frac{I'_0(|\pi p/L_s|\rho_c)K_0(|\pi p/L_s|\rho_s)}{I_0(|\pi p/L_s|\rho_s)}\right]C^1_{np}(z), \tag{A15}$$

$$G_{nm}(\rho,z) = \sum_{p=-\infty}^{\infty} I'_m\left(\left|\frac{\pi p}{L_s}\right|\rho\right)\left[K'_m\left(\left|\frac{\pi p}{L_s}\right|\rho_c\right) - \frac{I'_m(|\pi p/L_s|\rho_c)K_m(|\pi p/L_s|\rho_s)}{I_m(|\pi p/L_s|\rho_s)}\right]C^2_{np}(z), \tag{A16}$$

$$H_{nm}(\rho,z) = \sum_{p=-\infty}^{\infty} mI_m\left(\left|\frac{\pi p}{L_s}\right|\rho\right)\left[K'_m\left(\left|\frac{\pi p}{L_s}\right|\rho_c\right) - \frac{I'_m(|\pi p/L_s|\rho_c)K_m(|\pi p/L_s|\rho_s)}{I_m(|\pi p/L_s|\rho_s)}\right]C^3_{np}(z), \tag{A17}$$

$$D_n(\rho,z) = \sum_{p=-\infty}^{\infty} I_0\left(\left|\frac{\pi p}{L_s}\right|\rho\right)\left[K'_0\left(\left|\frac{\pi p}{L_s}\right|\rho_c\right) - \frac{I'_0(|\pi p/L_s|\rho_c)K_0(|\pi p/L_s|\rho_s)}{I_0(|\pi p/L_s|\rho_s)}\right]C^4_{np}(z), \tag{A18}$$

$$S_{nm}(\rho,z) = \sum_{p=-\infty}^{\infty} I_m\left(\left|\frac{\pi p}{L_s}\right|\rho\right)\left[K'_m\left(\left|\frac{\pi p}{L_s}\right|\rho_c\right) - \frac{I'_m(|\pi p/L_s|\rho_c)K_m(|\pi p/L_s|\rho_s)}{I_m(|\pi p/L_s|\rho_s)}\right]C^5_{np}(z), \tag{A19}$$

where

$$C^1_{np}(z) = i\mu_0\rho_c nL_c\frac{pe^{i(\pi pz/L_s)}}{n^2L_s^2 - L_c^2p^2} \times \{[(-1)^p e^{i(\pi pL_2/L_s)} + e^{-i(\pi pL_2/L_s)}] + (-1)^{n+1}[(-1)^p e^{i(\pi pL_1/L_s)} + e^{-i(\pi pL_1/L_s)}]\}, \tag{A20}$$

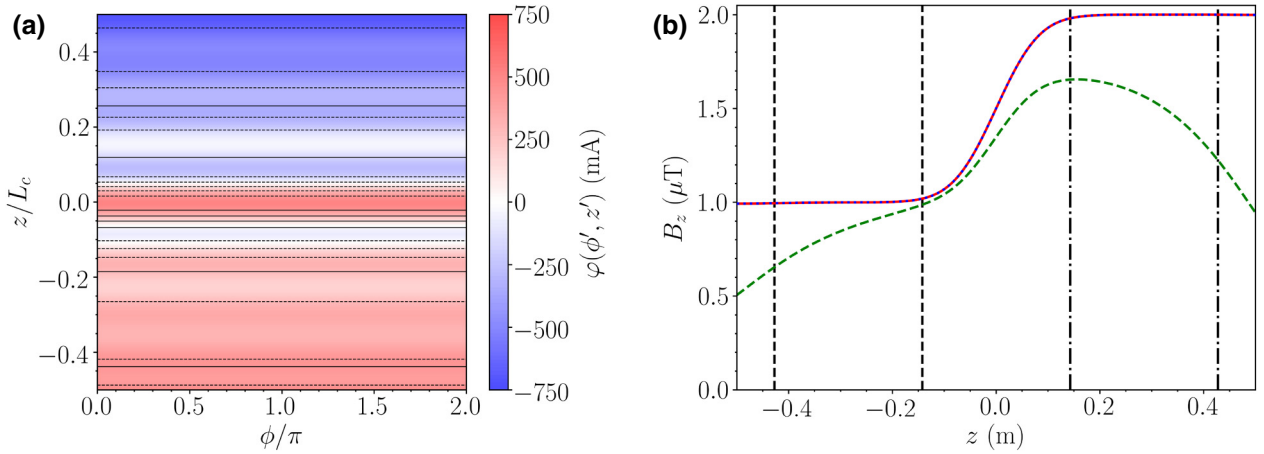


FIG. 8. Wire layouts (a) and performance (b) of an optimized hybrid active–passive uniform axial field-generating system in which current flows on a cylinder of length $L_c = 0.95$ m and radius $\rho_c = 0.245$ m. The wire layouts are optimized to generate axial constant fields B_z of two different magnitudes along the z axis of the cylinder in two separate regions. The current-carrying cylinder is placed symmetrically inside a perfect closed magnetic shield of length $L_s = 1$ m and radius $\rho_s = 0.25$ m and target magnetic field values of $B_z = 1$ μT and $B_z = 2$ μT are optimized between $\rho = [0, \rho_c/2]$ and either $z = [-0.45L_c, 0.15L_c]$ [dashed black lines in (b) where target $B_z = 1$ μT] and $z = [0.15L_c, 0.45L_c]$ [dash–dot black lines in (b) where target $B_z = 2$ μT]. The least-squares optimization is performed with parameters $N = 200$, $M = 0$, and $\beta = 2.97 \times 10^{-11}$. (a) Color map of the optimal current streamfunction on the cylinder [blue and red shaded regions correspond to the flow of current in opposite senses and their intensity shows the streamfunction magnitude from low (white) to high (intense color)]. Solid and dashed black curves represent discrete wires with opposite senses of current flow, approximating the current continuum with $N_\varphi = 8$ contour levels. (b) Axial magnetic field B_z versus axial position z calculated from the current continuum in (a) in three ways: analytically using Eqs. (37)–(39) (solid red curve); numerically using COMSOL Multiphysics version 5.5a and modeling the high-permeability cylinder as a perfect magnetic conductor (blue dotted curve, which essentially overlays the red curve); numerically *without* the high-permeability cylinder and using the Biot-Savart law with $N_\varphi = 250$ contour levels (dashed green curve).

$$C^2_{np}(z) = \frac{\mu_0 \rho_c L_c^2}{L_s} \frac{p^2 e^{i(\pi p z/L_s)}}{n^2 L_s^2 - L_c^2 p^2} \times \{[(-1)^p e^{i(\pi p L_2/L_s)} - e^{-i(\pi p L_2/L_s)}] + (-1)^{n+1}[(-1)^p e^{i(\pi p L_1/L_s)} - e^{-i(\pi p L_1/L_s)}]\}, \tag{A21}$$

$$C^3_{np}(z) = -\frac{|p|L_s}{p^2 \pi \rho} C^2_{np}(z), \tag{A22}$$

$$C^4_{np}(z) = \frac{i|p|}{p} C^1_{np}(z), \tag{A23}$$

$$C^5_{np}(z) = \frac{i|p|}{p} C^2_{np}(z). \tag{A24}$$

APPENDIX B: SOLENOIDAL COIL

As shown in previous work [36–38], a solenoid of the same length as the high-permeability cylinder provides the most optimal solution for generating a constant axial field. Because of the image currents, the finite solenoid effectively acts as one of infinite extension, resulting in the most homogeneously possible magnetic field in the z direction. A perfect finite solenoid of length L_c carries a total current of

$$I_t = \int_{-L_c/2}^{L_c/2} dz'\, I, \tag{B1}$$

where I is the current density, i.e., the current per unit solenoid length, resulting in the azimuthal current I_t/L_c. Using Eq. (25), the Fourier transform of the current through a finite solenoid is given by

$$J^{mp}_\phi(k) = I_t \delta_{m0} e^{-ikpL_c} \mathrm{Sinc}(kL_c/2). \tag{B2}$$

Substituting the above equation into Eq. (33) gives the magnetic field in the z direction:

$$B_z(\rho, \phi, z) = \frac{\mu_0 I_t \rho_c}{2\pi} \sum_{p=-\infty}^{\infty} \int_{-\infty}^{\infty} dk\, |k| e^{ikz} e^{-ikpL} \times \mathrm{Sinc}\left(\frac{kL_c}{2}\right) I_0(|k|\rho) \times \left[K_1(|k|\rho_c) + \frac{I_1(|k|\rho_c) K_0(|k|\rho_s)}{I_0(|k|\rho_s)}\right]. \tag{B3}$$

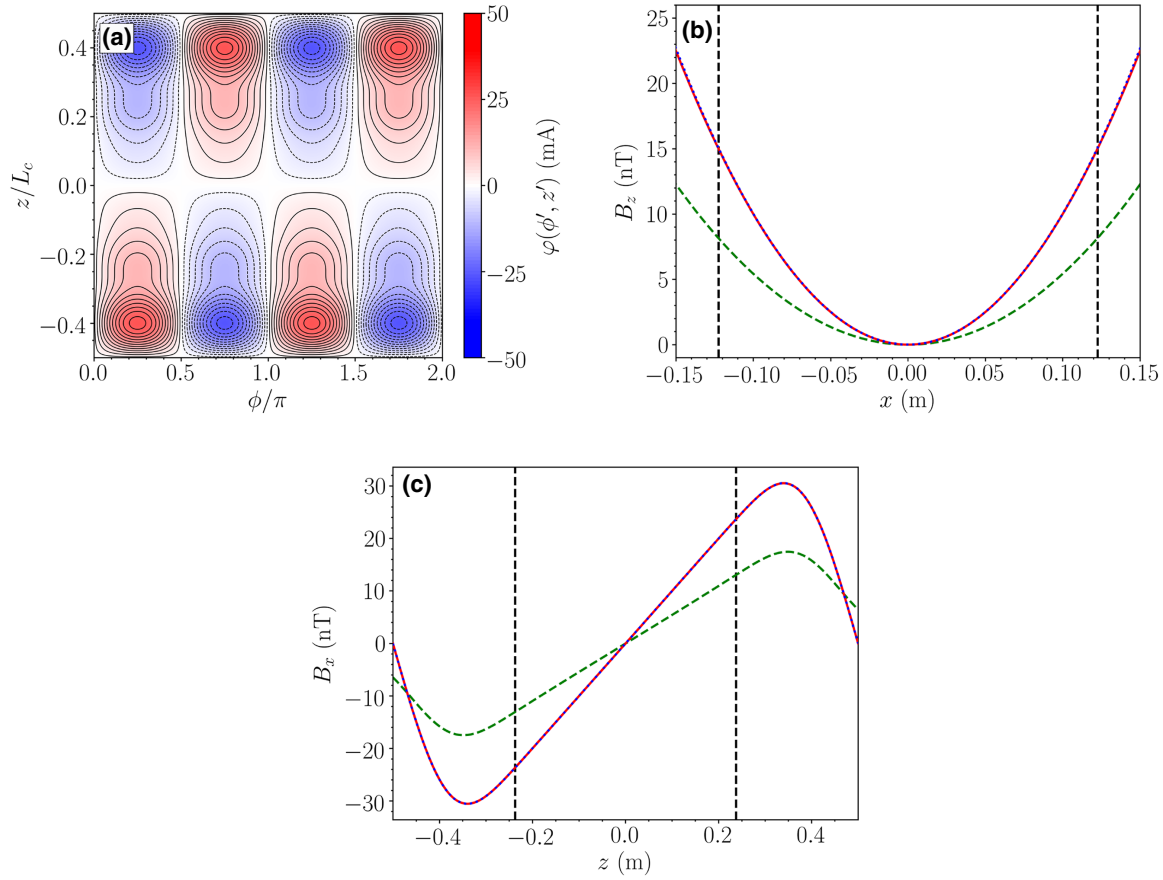


FIG. 9. Wire layouts (a) and performance (b),(c) of an optimized hybrid active–passive quadratic gradient field-generating system in which current flows on a cylinder of length $L_c = 0.95$ m and radius $\rho_c = 0.245$ m. The wire layouts are optimized to generate a quadratic gradient field $\mathbf{B} = (2xz\hat{\mathbf{x}} - 2yz\hat{\mathbf{y}} + (x^2 - y^2)\hat{\mathbf{z}})$ μT. The current-carrying cylinder is placed symmetrically inside a perfect closed magnetic shield of length $L_s = 1$ m and radius $\rho_s = 0.25$ m and the magnetic field is optimized between $\rho = [0, \rho_c/2]$ and $z = \pm L_c/4$; see the dashed black lines in (b) and (c), respectively. The least-squares optimization is performed with parameters $N = 200$, $M = 2$, and $\beta = 5.95 \times 10^{-12}$. (a) Color map of the optimal current streamfunction on the cylinder [blue and red shaded regions correspond to the flow of current in opposite senses and their intensity shows the streamfunction magnitude from low (white) to high (intense color)]. Solid and dashed black curves represent discrete wires with opposite senses of current flow, approximating the current continuum with $N_\varphi = 24$ contour levels. (b) Axial magnetic field B_z versus transverse position x at $z = 0$ calculated from the current continuum in (a) in three ways: analytically using Eqs. (37)–(39) (solid red curve); numerically using COMSOL Multiphysics version 5.5a and modeling the high-permeability cylinder as a perfect magnetic conductor (blue dotted curve, which essentially overlays the red curve); numerically *without* the high-permeability cylinder and using the Biot-Savart law with $N_\varphi = 250$ contour levels (dashed green curve). (c) Transverse magnetic field B_x versus axial position z at $x = 0.05$ m calculated from the current continuum in (a) in the same three ways as (b); labeled as in (b).

Performing the integral over k by expressing the summation over the infinite pseudocurrent reflections through a Fourier series expansion

$$\sum_{p=-\infty}^{\infty} e^{ikpL_s} = \frac{2\pi}{L_s} \sum_{p=-\infty}^{\infty} \delta\left(k - \frac{2\pi p}{L_s}\right), \tag{B4}$$

we find that

$$B_z(\rho, \phi, z) = \frac{\mu_0 I_t \rho_c}{L_c} \sum_{p=-\infty}^{\infty} \left|\frac{2\pi p}{L_c}\right| \cos\left(\frac{2\pi p z}{L_c}\right) \mathrm{Sinc}(\pi p) I_0\left(\left|\frac{2\pi p}{L_c}\right| \rho\right) \left[K_1\left(\left|\frac{2\pi p}{L_c}\right| \rho_c\right) + \frac{I_1(|2\pi p/L_c|\rho_c) K_0(|2\pi p/L_c|\rho_s)}{I_0(|2\pi p/L_c|\rho_s)}\right]. \tag{B5}$$

This summation can be simplified as the only contributing term is $p = 0$, which, when evaluated, results in

$$B_z(\rho, \phi, z) = \frac{\mu_0 I_t}{L_c}. \tag{B6}$$

This result might seem counterintuitive because the magnetic field is identical to a long solenoid in free space with N turns, i.e., $B_z(\rho, \phi, z) = \mu_0 IN/L_c$, with *no* field created by the cylindrical surface of the passive shield. This is, however, entirely physical as an infinite solenoid generates zero magnetic field outside of the solenoid itself. Consequently, there is no response due to the surface of the cylindrical wall and, therefore, no magnetic field generated by the cylindrical surface of the perfect magnetic conductor, i.e., the high-permeability cylinder.

APPENDIX C: EXAMPLE COIL DESIGNS

In Figs. 8 and 9, we present further hybrid active–passive systems, which generate more complex magnetic field landscapes beyond the constant field and field gradient considered in the main body of the paper. The coordinate axes and magnetic field plots are labeled in the same way as the systems presented in the main text. The design in Fig. 8 generates uniform axial magnetic fields B_z with different strengths in two different regions of a magnetic shield. The design in Fig. 9 generates a quadratic gradient field whose spatial variation matches the harmonic $\mathbf{B} = [2xz\hat{\boldsymbol{x}} - 2yz\hat{\boldsymbol{y}} + (x^2 - y^2)\hat{\boldsymbol{z}}]$. Further systems can be designed using the PYTHON code in the GitHub repository [54].

[1] X. Wu, Z. Pagel, B. S. Malek, T. H. Nguyen, F. Zi, D. S. Scheirer, and H. Müller, Gravity surveys using a mobile atom interferometer, Sci. Adv. **5**, 9 (2019).

[2] V. Menoret, P. Vermeulen, N. L. Moigne, S. Bonvalot, P. Bouyer, A. Landragin, and B. Desruelle, Gravity measurements below 10^{-9} g with a transportable absolute quantum gravimeter, Sci. Rep. **8**, 1 (2018).

[3] M. J. Snadden, J. M. McGuirk, P. Bouyer, K. G. Haritos, and M. A. Kasevich, Measurement of the Earth's Gravity Gradient with an Atom Interferometer-Based Gravity Gradiometer, Phys. Rev. Lett. **81**, 971 (1998).

[4] K. Bongs, M. Holynski, J. Vovrosh, P. Bouyer, G. Condon, E. Rasel, C. Schubert, W. P. Schleich, and A. Roura, Taking atom interferometric quantum sensors from the laboratory to real-world applications, Nat. Rev. Phys. **1**, 731 (2019).

[5] B. Patton, E. Zhivun, D. C. Hovde, and D. Budker, All-Optical Vector Atomic Magnetometer, Phys. Rev. Lett. **113**, 013001 (2014).

[6] Y. J. Kim and I. Savukov, Ultra-sensitive magnetic microscopy with an optically pumped magnetometer, Sci. Rep. **6**, 24773 (2016).

[7] H. Zhang, S. Zou, X. Chen, and W. Quan, Parameter modeling analysis and experimental verification on magnetic shielding cylinder of all-optical atomic spin magnetometer, J. Sens. **5**, 491746 (2015).

[8] M. V. Romalis and H. B. Dang, Atomic magnetometers for materials characterization, Mater. Today **14**, 6 (2011).

[9] T. Sander, J. Preusser, R. Mhaskar, J. Kitching, L. Trahms, and S. Knappe, Magnetoencephalography with a chip-scale atomic magnetometer, Biomed. Opt. Express **3**, 5 (2012).

[10] E. Boto, N. Holmes, J. Leggett, G. Roberts, V. Shah, S. S. Meyer, L. D. Muõz, K. J. Mullinger, T. M. Tierney, S. Bestmann, G. R. Barnes, R. Bowtell, and M. J. Brookes, Moving magnetoencephalography towards real-world applications with a wearable system, Nature **555**, 7698 (2018).

[11] I. Altarev, M. Bales, D. H. Beck, T. Chupp, K. Fierlinger, P. Fierlinger, F. Kuchler, T. Lins, M. G. Marino, B. Niessen, G. Petzoldt, U. Schläpfer, A. Schnabel, J. T. Singh, R. Stoepler, S. Stuiber, M. Sturm, B. Taubenheim, and J. Voigt, A large-scale magnetic shield with 10^6 damping at millihertz frequencies, J. Appl. Phys. **117**, 18 (2015).

[12] Y. Sakamoto, C. Bidinosti, Y. Ichikawa, Takefumi Satoh, Y. Ohtomo, S. Kojima, C. Funayama, T. Suzuki, M. Tsuchiya, T. Furukawa, A. Yoshimi, T. Ino, H. Ueno, Y. Matsuo, T. Fukuyama, and K. Asahi, Development of high-homogeneity magnetic field coil for ^{129}Xi EDM experiment, Hyperfine Interact. **230**, 4 (2015).

[13] I. Moric, P. Laurent, P. Chatard, C.-M. de Graeve, S. Thomin, V. Christophe, and O. Grosjean, Magnetic shielding of the cold atom space clock PHARAO, Acta Astronaut. **102**, 287 (2014).

[14] L. Liu, D.-S. Lü, W.-B. Chen, T. Li, Q.-Z. Qu, B. Wang, L. Li, W. Ren, Z.-R. Dong, J.-B. Zhao, W.-B. Xia, X. Zhao, J.-W. Ji, M.-F. Ye, Y.-G. Sun, Y.-Y. Yao, D. Song, Z.-G. Liang, S.-J. Hu, and Y.-Z. Wang, In-orbit operation of an atomic clock based on laser-cooled ^{87}Rb atoms, Nat. Commun. **9**, 2760 (2018).

[15] N. F. Ramsey, Experiments with separated oscillatory fields and hydrogen masers, Rev. Mod. Phys. **62**, 541 (1990).

[16] J. J. Hudson, D. M. Kara, I. J. Smallman, B. E. Sauer, M. R. Tarbutt, and E. A. Hinds, Improved measurement of the shape of the electron, Nature **473**, 493 (2011).

[17] ACME Collaboration, Improved limit on the electric dipole moment of the electron, Nature **562**, 355 (2018).

[18] I. Altarev, P. Fierlinger, T. Lins, M. G. Marino, B. Nießen, G. Petzoldt, M. Reisner, S. Stuiber, M. Sturm, J. Taggart Singh, B. Taubenheim, H. K. Rohrer, and U. Schläpfer, Minimizing magnetic fields for precision experiments, J. Appl. Phys. **117**, 233903 (2015).

[19] J. M. Brown, S. J. Smullin, T. W. Kornack, and M. V. Romalis, New Limit on Lorentz- and CPT-Violating Neutron Spin Interactions, Phys. Rev. Lett. **105**, 151604 (2010).

[20] M. E. Limes, N. Dural, M. V. Romalis, E. L. Foley, T. W. Kornack, A. Nelson, L. R. Grisham, and J. Vaara, Dipolar and scalar ^{3}He-^{1}29Xe frequency shifts in stemless cells, Phys. Rev. A **100**, 010501 (2019).

[21] F. Allmendinger, W. Heil, S. Karpuk, W. Kilian, A. Scharth, U. Schmidt, A. Schnabel, Yu Sobolev, and K. Tullney, New Limit on Lorentz-Invariance and CPT-Violating Neutron Spin Interactions Using a Free-Spin-Precession

^{3}He-^{129}Xe Co-Magnetometer, Phys. Rev. Lett. **112**, 110801 (2014).
[22] A. Mager, Magnetic shielding efficiencies of cylindrical shells with axis parallel to the field, J. Appl. Phys. **39**, 1914 (1968).
[23] S. S. Grabchikov, A. V. Trukhanov, S. V. Trukhanov, I. S. Kazakevich, A. A. Solobay, V. T. Erofeenko, N. A. Vasilenkov, O. S. Volkova, and A. Shakin, Effectiveness of the magnetostatic shielding by the cylindrical shells, J. Magn. Magn. Mater. **398**, 49 (2016).
[24] J. Prat-Camps, C. Navau, D. Chen, and A. Sanchez, Exact analytical demagnetizing factors for long hollow cylinders in transverse field, IEEE Magn. Lett. **3**, 0500104 (2012).
[25] F. Roméo and D. I. Hoult, Magnet field profiling: Analysis and correcting coil design, Magn. Reson. Med. **1**, 1 (1984).
[26] S. Pissanetzky, Minimum energy MRI gradient coils of general geometry, Meas. Sci. Technol. **3**, 7 (1992).
[27] M. Poole and R. Bowtell, Novel gradient coils designed using a boundary element method, Concept. Magn. Reson. B **31B**, 3 (2007).
[28] R. A. Lemdiasov and R. Ludwig, A stream function method for gradient coil design, Concept. Magn. Reson. B **26B**, 1 (2005).
[29] L. K. Forbes and S. Crozier, A novel target-field method for finite-length magnetic resonance shim coils: II. Tesseral shims, J. Phys. D: Appl. Phys. **35**, 9 (2002).
[30] L. K. Forbes and S. Crozier, A novel target-field method for finite-length magnetic resonance shim coils: I. Zonal shims, J. Phys. D: Appl. Phys. **34**, 24 (2001).
[31] N. Holmes, T. M. Tierney, J. Leggett, E. Boto, S. Mellor, G. Roberts, R. M. Hill, V. Shah, G. R. Barnes, M. J. Brookes, and R. Bowtell, Balanced, bi-planar magnetic field and field gradient coils for field compensation in wearable magnetoencephalography, Sci. Rep. **9**, 14196 (2019).
[32] S. Celozzi, R. Araneo, and G. Lovat, *Appendix B: Magnetic Shielding* (John Wiley & Sons Ltd., Hoboken, New Jersey, 2008).
[33] S. Celozzi and F. Garzia, Active shielding for power-frequency magnetic field reduction using genetic algorithms optimisation, IEE Proc. A – Sci. Mes. Technol. **151**, 1 (2004).
[34] K. F. Man, K. S. Tang, and S. Kwong, Genetic algorithms: Concepts and applications [in engineering design], IEEE Trans. Ind. **43**, 5 (1996).
[35] A. Caciagli, R. J. Baars, A. P. Philipse, and B. W. M. Kuipers, Exact expression for the magnetic field of a finite cylinder with arbitrary uniform magnetization, J. Magn. Magn. Mater. **456**, 423 (2018).
[36] C.-Y. Liu, T. Andalib, D. C. M. Ostapchuk, and C. P. Bidinosti, Analytic models of magnetically enclosed spherical and solenoidal coils, Nucl. Instrum. Methods Phys. Res. **949**, 162837 (2020).
[37] R. Lambert and C. Uphoff, Magnetically shielded solenoid with field of high homogeneity, Rev. Sci. Instrum. **46**, 3 (1975).
[38] R. J. Hanson and F. M. Pipkin, Magnetically shielded solenoid with field of high homogeneity, Rev. Sci. Instrum. **36**, 2 (1965).
[39] J. D. Jackson, *Classical Electrodynamics* (Wiley, New York, 1998), 3rd ed.
[40] Q. Cao, D. Pan, J. Li, Y. Jin, Z. Sun, S. Lin, G. Yang, and L. Li, Optimization of a coil system for generating uniform magnetic fields inside a cubic magnetic shield, Energies **11**, 3 (2018).
[41] N. Holmes, J. Leggett, E. Boto, G. Roberts, R. M. Hill, T. M. Tierney, V. Shah, G. R. Barnes, M. J. Brookes, and R. Bowtell, A bi-planar coil system for nulling background magnetic fields in scalp mounted magnetoencephalography, NeuroImage **181**, 1 (2018).
[42] T. Liu, J. Voigt, Z. Sun, A. Schnabel, K. Grueneberg, I. Fan, and L. Li, in *Conference on Precision Electromagnetic Measurements* (Paris, 2018), p. 1.
[43] T. Liu, A. Schnabel, Z. Sun, J. Voigt, and L. Li, Approximate expressions for the magnetic field created by circular coils inside a closed cylindrical shield of finite thickness and permeability, J. Magn. Magn. Mater. **507**, 166846 (2020).
[44] L.-W. Li, M.-S. Leong, T.-S. Yeo, and P.-S. Kooi, Electromagnetic dyadic Green's functions in spectral domain for multilayered cylinders, J. Electromagnet. Wave **14**, 961 (2000).
[45] R. Turner, A target field approach to optimal coil design, J. Phys. D: Appl. Phys. **19**, 8 (1986).
[46] J. W. Carlson, K. A. Derby, K. C. Hawryszko, and M. Weideman, Design and evaluation of shielded gradient coils, Magn. Reson. Med. **26**, 2 (1992).
[47] D. I. Hoult and R. Deslauriers, Accurate shim-coil design and magnet-field profiling by a power-minimization-matrix method, J. Magn. Reson. **108**, 1 (1994).
[48] P. Hammond, Electric and magnetic images, Proc. IEE Part C Monogr. **107**, 306 (1960).
[49] P. Hammond, Effect of finite thickness of magnetic substrate on planar inductors, IEEE Trans. Magn. **26**, 270 (1990).
[50] R. Turner and R. M. Bowley, Passive screening of switched magnetic field gradients, J. Phys. E Sci. Instrum. **19**, 876 (1986).
[51] A. Acín, I. Bloch, H. Buhrman, T. Calarco, C. Eichler, J. Eisert, D. Esteve, N. Gisin, S. J. Glaser, F. Jelezko, S. Kuhr, M. Lewenstein, M. F. Riedel, P. O. Schmidt, R. Thew, A. Wallraff, I. Walmsley, and F. K. Wilhelm, The quantum technologies roadmap: A European community view, New J. Phys. **20**, 080201 (2018).
[52] J. R. Corea, A. M. Flynn, B. Lechene, G. Scott, G. D. Reed, P. J. Shin, M. Lustig, and A. C. Ariasb, Screen-printed flexible MRI receive coils, Nat. Commun. **7**, 10839 (2016).
[53] T. D. Ngo, A. Kashani, G. Imbalzano, K. T. Q. Nguyen, and D. Hui, Additive manufacturing (3D printing): A review of materials, methods, applications and challenges, Compos. B. Eng. **143**, 172 (2018).
[54] https://github.com/peterjhobson/fields_in_shields.

Chapter 4

Planar Coil Optimization in a Magnetically Shielded Cylinder

Planar Coil Optimization in a Magnetically Shielded Cylinder

M. Packer,[1] P.J. Hobson,[1] N. Holmes,[1,2] J. Leggett,[1,2] P. Glover,[1,2] M.J. Brookes,[1,2] R. Bowtell,[1,2] and T.M. Fromhold[1,*]

[1] *School of Physics and Astronomy, University of Nottingham, Nottingham NG7 2RD, United Kingdom*
[2] *Sir Peter Mansfield Imaging Centre, School of Physics and Astronomy, University of Nottingham, Nottingham NG7 2RD, United Kingdom*

(Received 18 January 2021; revised 5 May 2021; accepted 13 May 2021; published 2 June 2021)

Hybrid magnetic shields with both active field generating components and high-permeability magnetic shielding are increasingly needed for various technologies and experiments that require precision-controlled magnetic field environments. However, the fields generated by the active components interact with the passive magnetic shield, distorting the desired field profiles. Consequently, optimization of the active components needed to generate user-specified target fields must include coupling to the high-permeability passive components. Here, we consider the optimization of planar active systems, on which an arbitrary static current flows, coupled to a closed high-permeability cylindrical shield. We modify the Green's function for the magnetic vector potential to match boundary conditions on the shield's interior surface, enabling us to construct an inverse optimization problem to design planar coils that generate user-specified magnetic fields inside high-permeability shields. We validate our methodology by designing two biplanar hybrid active-passive systems, which generate a constant transverse field, $\mathbf{B} = \hat{\mathbf{x}}$, and a linear field gradient, $\mathbf{B} = (-x\hat{\mathbf{x}} - y\hat{\mathbf{y}} + 2z\hat{\mathbf{z}})$, respectively. For both systems, the inverse-optimized magnetic field profiles agree well with forward numerical simulations. Our design methodology is accurate and flexible, facilitating the miniaturization of high-performance hybrid magnetic field generating technologies with strict design constraints and spatial limitations.

DOI: 10.1103/PhysRevApplied.15.064006

I. INTRODUCTION

Tailored, high-precision, low magnetic field environments are required for many applications, devices, and experiments. Examples include magnetic field control in quantum sensing of gravity for underground surveying and mapping [1–4], magnetic field cancelation for atomic magnetometry [5] with applications in medical imaging such as magnetoencephalography [6–9] and neonatal and fetal magnetocardiography [10–12], and noise suppression in fundamental physics experiments [13–15]. Usually, these systems are enclosed by a shield formed from high-permeability material, which reduces stray external magnetic fields that can limit the accuracy and sensitivity of the measurements. In particular, cylindrical shield geometries are often used because the dimensions and spacing of multiple cylindrical shield layers can be optimized to generate a large interior shielded region [16,17]. The magnetic field interior to the shield can then be adjusted by active field generating components to either cancel background fields further or to define a specific field environment. However, the surrounding passive shielding material deforms the magnetic field profiles generated by the active components, making it hard to design wire patterns that accurately generate specified target magnetic field profiles [18].

Boundary element methods (BEMs) can be used to optimize magnetic fields generated by surface currents on a triangular mesh [19–22] to generate arbitrary target magnetic fields. BEMs are extremely powerful and flexible since they can be used to define active systems with complex geometries inside passive shields. They are, however, limited by computational power with results depending on mesh size and on the distance of the active components from the shielding material. Alternatively, analytical methods for optimizing hybrid active-passive systems are advantageous since they provide intuition and understanding of how magnetic fields are distorted by the presence of high-permeability material. Analytical formulations also provide a fast and efficient route to determine the best system for generating a bespoke user-specified magnetic field profile.

Currently, analytical models for hybrid active-passive systems are restricted to a limited number of scenarios. Simple discrete coil geometries have been formulated in cylindrical high-permeability magnetic shields, where the magnetic field is decomposed into azimuthal Fourier modes [23–25] and matched at the shield boundary.

*mark.fromhold@nottingham.ac.uk

 © 2021 American Physical Society

Planar high-permeability materials have been incorporated into optimization procedures using the method of mirror images [26,27] to determine the total magnetic field generated by a static current source inside a magnetically shielded room [28–31]. Similar work in magnetic resonance imaging has investigated the interaction of switched magnetic field gradients with high-conductivity materials used for passive shielding [32]. These formulations incorporate the effect of the shielding material by explicitly solving Maxwell's equations by matching the required boundary conditions on the surface interface to find the total magnetic field generated by the system. More recently, solutions for the interaction between a static current source and a finite-length closed cylindrical high-permeability shield have been formulated for the specific case of cylindrical coaxial surface current geometries [33]. The boundary conditions at the shield's surface were approximated to those of a perfect magnetic conductor and the response of the shield was calculated by matching the azimuthal Fourier modes and using the method of mirror images. The magnetic field generated by the entire system was then calculated in terms of the initial current source and used in conjunction with a least squares optimization to determine globally optimal cylindrical currents to generate arbitrary magnetic field profiles. However, coaxial cylindrical coils are not appropriate to all systems because of length and optical access limitations.

In this work, by applying the same approach as Packer *et al.* [33], we analytically determine the effect of a finite-length closed cylindrical high-permeability shield on the magnetic field generated by an arbitrary static current distribution on an interior circular plane, oriented perpendicular to the axis of the cylinder. We calculate the effect of the high-permeability cylinder on the magnetic field produced by current flow on the plane, which enables us to determine optimal current paths to generate user-specified target fields inside the cylinder. We first derive the vector potential generated by an arbitrary planar current source. Then, we calculate a pseudocurrent density induced on the cylindrical surface of the high-permeability material in response to the planar current source, and, hence, derive a Green's function for our system. Finally, we implement a Fourier decomposition of the current paths to calculate the total magnetic field in terms of a set of weighted Fourier coefficients. This formulation allows the incorporation of a quadratic optimization procedure to determine globally optimal designs that generate user-specified target magnetic field profiles. Through the use of this optimization procedure, we design two example biplanar coil systems optimized for operation inside a finite-length closed high-permeability cylindrical magnetic shield. In both cases, we confirm that our analytical model agrees well with the result of numerical finite element simulations. Our work extends the range of coil geometries that can be efficiently optimized to generate static user-specified target magnetic fields in the presence of high-permeability materials, expanding design flexibility for systems that require precision-controlled magnetic field environments.

II. THEORY

In Ref. [33] the interaction between an arbitrary static current flow on a cylinder and an exterior finite-length closed high-permeability cylindrical magnetic shield was formulated analytically. The vector potential in free space was related to an arbitrary current on the cylinder $\mathbf{j_c}$, and a bound pseudocurrent on the shield's cylindrical surface $\widetilde{\mathbf{j}}$, which is equivalent to the induced magnetization of the shield, resulting in

$$\nabla^2\mathbf{A} = -\mu_0(\mathbf{j_c} + \widetilde{\mathbf{j}}), \tag{1}$$

with integral solution in terms of an arbitrary current density

$$\mathbf{A}(\mathbf{r}) = \mu_0 \int_{r'} d^3\mathbf{r}' G(\mathbf{r},\mathbf{r}')\mathbf{j}(\mathbf{r}'), \tag{2}$$

where $G(\mathbf{r},\mathbf{r}')$ is the associated Green's function for the system [26]. It was then shown that the high-permeability magnetic shield could be assumed to be a perfect magnetic conductor with minimal error, meaning a combination of methods could be used to satisfy the boundary conditions at the shield's surface. From this, the total magnetic field generated by the entire system could be efficiently calculated in terms of the initial current source. An orthogonal current density basis was then used in conjunction with a least squares optimization to determine globally optimal current flow patterns in a cylindrical basis. The subsequent example designs were verified using numerical finite element software, showing deviations from the analytical model of $\mathcal{O}(\mu^{-1})$, in line with previous findings [34,35]. Here, we use the same methodology to find optimal current flow patterns on a planar basis interior to a finite-length closed high-permeability cylindrical magnetic shield.

We consider a closed cylindrical magnetic shield surrounded by free space, as shown in Fig. 1. This cylinder has relative permeability, $\mu_r \gg 1$, radius ρ_s, and length L_s, with planar end caps located at $z = \pm L_s/2$. Inside this cylinder, an arbitrary current flows on a circular planar surface of radius $\rho_c < \rho_s$, centered on the z axis and lying in the $z = z'$ plane where $|z'| < L_s/2$.

The boundary conditions on the surface of the shield, illustrated in Fig. 1, are approximated to that of a perfect magnetic conductor

$$B_\rho\big|_{z=\pm L_s/2} = 0, \quad B_\phi\big|_{z=\pm L_s/2,\rho=\rho_s} = 0, \quad B_z\big|_{\rho=\rho_s} = 0, \tag{3}$$

provided the material permeability and thickness are sufficiently large [33].

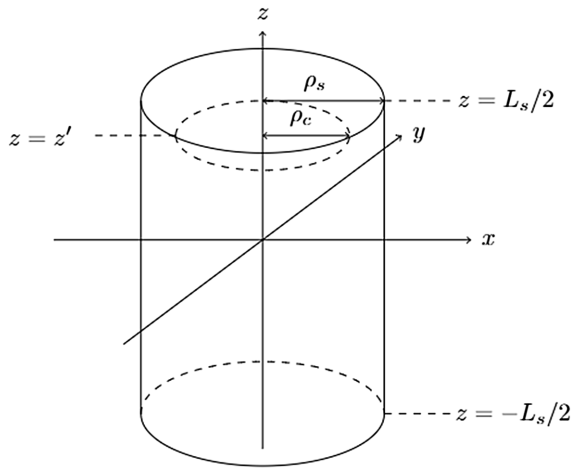


FIG. 1. A cylindrical hollow high-permeability magnetic shield of length L_s, radius ρ_s, and with planar end caps located at $z = \pm L_s/2$ encloses an interior circular current source (bounded by the upper dashed curve) of radius $\rho_c < \rho_s$, which lies in the $z = z'$ plane.

The vector potential generated by a current source in cylindrical coordinates can be expressed as

$$A_\rho(\mathbf{r}) = \mu_0 \int_{r'} d^3\mathbf{r}' G(\mathbf{r},\mathbf{r}')[j_\rho(\mathbf{r}')\cos(\phi-\phi') + j_\phi(\mathbf{r}')\sin(\phi-\phi')], \tag{4}$$

$$A_\phi(\mathbf{r}) = -\mu_0 \int_{r'} d^3\mathbf{r}' G(\mathbf{r},\mathbf{r}')[j_\rho(\mathbf{r}')\sin(\phi-\phi') - j_\phi(\mathbf{r}')\cos(\phi-\phi')], \tag{5}$$

$$A_z(\mathbf{r}) = \mu_0 \int_{r'} d^3\mathbf{r}' G(\mathbf{r},\mathbf{r}') j_z(\mathbf{r}'). \tag{6}$$

Since there is no current flow in the z direction for a planar current source perpendicular to the axis of the cylindrical shield, the continuity equation can be used to express the planar current flow in terms of a single scalar streamfunction defined on the planar surface

$$j_\rho(\mathbf{r}') = \frac{1}{\rho'}\frac{\partial\varphi(\mathbf{r}')}{\partial\phi'}, \qquad j_\phi(\mathbf{r}') = -\frac{\partial\varphi(\mathbf{r}')}{\partial\rho'}, \tag{7}$$

where $\varphi(\mathbf{r}') = \varphi(\rho',\phi')$. To exploit the radial symmetries of the system, we choose to decompose the Green's function in cylindrical coordinates in terms of Bessel functions of the first kind,

$$G(\mathbf{r},\mathbf{r}') = \frac{1}{4\pi}\sum_{m=-\infty}^{\infty} e^{im(\phi-\phi')} \times \int_0^\infty dk\, e^{-k|z-z'|} J_m(k\rho)J_m(k\rho'), \tag{8}$$

allowing the vector potential to be expressed in terms of cylindrical harmonics defined on a circular plane. Using Eqs. (4)–(8), we cast the vector potential in a simplified form

$$A_\rho(\mathbf{r}) = \frac{i\mu_0}{2\rho}\sum_{m=-\infty}^{\infty} e^{im\phi}\int_0^\infty dk\, m e^{-k|z-z'|} J_m(k\rho)\varphi^m(k), \tag{9}$$

$$A_\phi(\mathbf{r}) = -\frac{\mu_0}{2}\sum_{m=-\infty}^{\infty} e^{im\phi}\int_0^\infty dk\, k e^{-k|z-z'|} J'_m(k\rho)\varphi^m(k), \tag{10}$$

$$A_z(\mathbf{r}) = 0, \tag{11}$$

where $J'_m(z)$ is the derivative of $J_m(z)$ with respect to z, and $\varphi^m(k)$ is defined as the mth order Hankel transform

$$\varphi^m(k) = \frac{1}{2\pi}\int_0^\infty d\rho' \int_0^{2\pi} d\phi'\, e^{-im\phi'}\rho' J_m(k\rho')\varphi(\rho',\phi). \tag{12}$$

We now consider the vector potential generated by the magnetic shield. We seek a Fourier representation of the bound pseudocurrent density, $\tilde{\mathbf{j}} = \tilde{j_\phi}(\phi',z')\,\hat{\boldsymbol{\phi}} + \tilde{j_z}(\phi',z')\hat{\mathbf{z}}$, which satisfies the boundary condition over the entire domain of the shield. In particular, we wish to equate the shared azimuthal Fourier modes at the radial boundary of the shield cylinder. This is achieved using a combination of methods that must be applied sequentially, since each method satisfies the condition at an orthogonal boundary. The radial condition is satisfied by equating the magnetic field generated by the cylindrical pseudocurrent density and planar current flow, generating a relation between the response of an infinite cylindrical shield and the initial current source. Then, the boundary condition at the end caps can simultaneously be satisfied by applying the method of mirror images [26]. These methods can be combined because the infinite pseudocurrent density and planar current flow are spatially orthogonal to the end caps, meaning that any reflections generated by the application of the method of mirror images continue to satisfy the radial condition. The components of the vector potential generated by a pseudocurrent density induced on an infinite cylinder [32] in the region $\rho < \rho_s$ are given by

$$A_\rho(\rho,\phi,z) = -\frac{i\mu_0\rho_s}{4\pi}\sum_{m=-\infty}^{\infty}\int_{-\infty}^{\infty} dk\, e^{im\phi}e^{ikz} \times [I_{m-1}(|k|\rho)K_{m-1}(|k|\rho_s) - I_{m+1}(|k|\rho)K_{m+1}(|k|\rho_s)]\tilde{j}^m_\phi(k), \tag{13}$$

$$A_\phi(\rho,\phi,z) = \frac{\mu_0\rho_s}{4\pi}\sum_{m=-\infty}^{\infty}\int_{-\infty}^{\infty} dk\, e^{im\phi}e^{ikz} \times [I_{m-1}(|k|\rho)K_{m-1}(|k|\rho_s) + I_{m+1}(|k|\rho)K_{m+1}(|k|\rho_s)]\tilde{j}_\phi^m(k), \quad (14)$$

$$A_z(\rho,\phi,z) = \frac{\mu_0\rho_s}{2\pi}\sum_{m=-\infty}^{\infty}\int_{-\infty}^{\infty} dk\, e^{im\phi}e^{ikz} \times I_m(|k|\rho)K_m(|k|\rho_s)\tilde{j}_z^m(k), \quad (15)$$

where the Fourier transforms of the pseudocurrents are defined by

$$j_\phi^m(k) = \frac{1}{2\pi}\int_0^{2\pi} d\phi'\, e^{-im\phi'}\int_{-\infty}^{\infty} dz'\, e^{-ikz'}\tilde{j}_\phi(\phi',z'), \quad (16)$$

$$j_z^m(k) = \frac{1}{2\pi}\int_0^{2\pi} d\phi'\, e^{-im\phi'}\int_{-\infty}^{\infty} dz'\, e^{-ikz'}\tilde{j}_z(\phi',z'). \quad (17)$$

The corresponding inverse transforms are given by

$$\tilde{j}_\phi(\phi',z') = \frac{1}{2\pi}\sum_{m=-\infty}^{\infty}\int_{-\infty}^{\infty} dk\, e^{im\phi'}e^{ikz'}j_\phi^m(k), \quad (18)$$

$$\tilde{j}_z(\phi',z') = \frac{1}{2\pi}\sum_{m=-\infty}^{\infty}\int_{-\infty}^{\infty} dk\, e^{im\phi'}e^{ikz'}j_z^m(k). \quad (19)$$

Therefore, adding the contributions from the planar current flow, Eqs. (9)–(10), and the infinite pseudocurrent density, Eqs. (13)–(15), while using Eqs. (16)–(19), and applying the method of mirror images for two infinitely large parallel planes, we can write the total magnetic field generated by the system in the region $\rho < \rho_s$ as

$$B_\rho(\rho,\phi,z) = -\frac{\mu_0}{2\pi}\sum_{p=-\infty}^{\infty}\sum_{m=-\infty}^{\infty} e^{im\phi} \times\left[\int_0^{\infty} dk\, k^2\frac{z-(-1)^p z'+pL_s}{|z-(-1)^p z'+pL_s|} \times e^{-k|z-(-1)^p z'+pL_s|}J_m'(k\rho)\varphi^m(k) - \frac{i\rho_s}{\pi}\int_{-\infty}^{\infty} dk\, ke^{ikz}I_m'(|k|\rho)K_m'(|k|\rho_s)j_\phi^{mp}(k)\right], \quad (20)$$

$$B_\phi(\rho,\phi,z) = -\frac{i\mu_0}{2\rho}\sum_{p=-\infty}^{\infty}\sum_{m=-\infty}^{\infty} me^{im\phi} \times\left[\int_0^{\infty} dk\, k\frac{z-(-1)^p z'+pL_s}{|z-(-1)^p z'+pL_s|} \times e^{-k|z-(-1)^p z'+pL_s|}J_m(k\rho)\varphi^m(k) - \frac{i\rho_s}{\pi}\int_{-\infty}^{\infty} dk\,\frac{|k|}{k}e^{ikz}I_m(|k|\rho)K_m'(|k|\rho_s)j_\phi^{mp}(k)\right], \quad (21)$$

$$B_z(\rho,\phi,z) = \frac{\mu_0}{2}\sum_{p=-\infty}^{\infty}\sum_{m=-\infty}^{\infty} e^{im\phi} \times\left[\int_0^{\infty} dk\, k^2e^{-k|z-(-1)^p z'+pL_s|}J_m(k\rho)\varphi^m(k) - \frac{\rho_s}{\pi}\int_{-\infty}^{\infty} dk\,|k|e^{ikz}I_m(|k|\rho)K_m'(|k|\rho_s)j_\phi^{mp}(k)\right], \quad (22)$$

where $j_\phi^{mp}(k)$ is the pth reflected Fourier-transformed azimuthal pseudocurrent density induced on the cylindrical surface of the magnetic shield with $I_m'(z)$ and $K_m'(z)$ defined as the derivatives with respect to z of the modified Bessel functions of the first and second kinds, $I_m(z)$ and $K_m(z)$, respectively. By applying the boundary condition at the radial surface, Eq. (3), we can match the shared mth azimuthal Fourier mode generated by each pth reflected pseudocurrent and streamfunction, resulting in the relation

$$\int_{-\infty}^{\infty} dk\,|k|e^{ikz}I_m(|k|\rho_s)K_m'(|k|\rho_s)j_\phi^{mp}(k) = \frac{\pi}{\rho_s}\int_0^{\infty} dk\, k^2e^{-k|z-(-1)^p z'+pL_s|}J_m(k\rho_s)\varphi^m(k). \quad (23)$$

Physically, due to the formulation of the response in terms of a pseudocurrent density, there must be a unique solution that is independent of the axial position that satisfies the boundary condition over the infinite domain of the cylindrical shield. Therefore, we perform an inverse Fourier transform with respect to z to generate an integral representation of the pth reflected Fourier pseudocurrent density, $j_\phi^{mp}(k)$, in terms of the mth-order Hankel transform of the streamfunction defined on the planar surface, $\varphi^m(k)$,

$$j_\phi^{mp}(k) = \frac{e^{-ik[(-1)^p z'+pL_s]}}{\rho_s|k|I_m(|k|\rho_s)K_m'(|k|\rho_s)} \times\int_0^{\infty} d\tilde{k}\,\frac{\tilde{k}^3}{\tilde{k}^2+k^2}J_m(\tilde{k}\rho_s)\varphi^m(\tilde{k}). \quad (24)$$

This expression for $j_\phi^{mp}(k)$ can now be substituted into Eqs. (20)–(22) to determine the total magnetic field in

terms of $\varphi^m(k)$. Next, we must choose an appropriate expansion of the streamfunction, $\varphi(\rho', \phi')$. Although the choice of orthogonal basis for the expansion of the streamfunction is somewhat arbitrary, a choice of basis that considers the symmetries between the Hankel transform, coordinate system, and the integral representation of the pseudocurrent yields a simpler solution. Here, we choose to decompose the radial component of the planar current flow into a Fourier-Bessel series while using a Fourier series representation of the azimuthal dependence,

$$\varphi(\rho', \phi') = [H(\rho') - H(\rho - \rho_c)]\rho_c \sum_{n=1}^{N}\sum_{m'=0}^{M} J_{m'}\left(\frac{\rho_{nm'}\rho'}{\rho_c}\right)[W_{nm'}\cos(m'\phi') + Q_{nm'}\sin(m'\phi')], \tag{25}$$

where $(W_{nm'}, Q_{nm'})$ are Fourier coefficients and $\rho_{nm'}$ is the nth zero of the m'th Bessel function of the first kind, $J_{m'}(\rho_{nm'}) = 0$. Therefore, using Eqs. (20)–(22), (24), and (25), the total magnetic field generated by an arbitrary current flow on the planar surface inside the closed finite high-permeability cylinder can be written as

$$B_\rho(\rho, \phi, z) = \frac{\mu_0\rho_c^3}{2}\sum_{n=1}^{N}\sum_{m=0}^{M}\rho_{nm}J'_m(\rho_{nm})[W_{nm}\cos(m\phi) + Q_{nm}\sin(m\phi)]B_\rho^{nm}(\rho, z), \tag{26}$$

$$B_\phi(\rho, \phi, z) = \frac{\mu_0\rho_c^3}{2\rho}\sum_{n=1}^{N}\sum_{m=0}^{M}m\rho_{nm}J'_m(\rho_{nm})[W_{nm}\sin(m\phi) - Q_{nm}\cos(m\phi)]B_\phi^{nm}(\rho, z), \tag{27}$$

$$B_z(\rho, \phi, z) = \frac{\mu_0\rho_c^3}{2}\sum_{n=1}^{N}\sum_{m=0}^{M}\rho_{nm}J'_m(\rho_{nm})[W_{nm}\cos(m\phi) + Q_{nm}\sin(m\phi)]B_z^{nm}(\rho, z), \tag{28}$$

where

$$B_\rho^{nm}(\rho, z) = -\int_0^\infty dk\, k^2\sigma(k; z, z', L_s)\frac{J'_m(k\rho)J_m(k\rho_c)}{k^2\rho_c^2 - \rho_{nm}^2} - \sum_{p=1}^{\infty}\tilde{p}\,|\tilde{p}|\lambda_p(z, z', L_s)\frac{I'_m(|\tilde{p}|\rho)I_m(|\tilde{p}|\rho_c)K_m(|\tilde{p}|\rho_s)}{I_m(|\tilde{p}|\rho_s)(|\tilde{p}|^2\rho_c^2 + \rho_{nm}^2)}, \tag{29}$$

$$B_\phi^{nm}(\rho, z) = \int_0^\infty dk\, k\sigma(k; z, z', L_s)\frac{J_m(k\rho)J_m(k\rho_c)}{k^2\rho_c^2 - \rho_{nm}^2} + \sum_{p=1}^{\infty}\tilde{p}\,\lambda_p(z, z', L_s)\frac{I_m(|\tilde{p}|\rho)I_m(|\tilde{p}|\rho_c)K_m(|\tilde{p}|\rho_s)}{I_m(|\tilde{p}|\rho_s)(|\tilde{p}|^2\rho_c^2 + \rho_{nm}^2)}, \tag{30}$$

$$B_z^{nm}(\rho, z) = \int_0^\infty dk\, k^2\gamma(k; z, z', L_s)\frac{J_m(k\rho)J_m(k\rho_c)}{k^2\rho_c^2 - \rho_{nm}^2} - \sum_{p=1}^{\infty}\tilde{p}^2\tau_p(z, z', L_s)\frac{I_m(|\tilde{p}|\rho)I_m(|\tilde{p}|\rho_c)K_m(|\tilde{p}|\rho_s)}{I_m(|\tilde{p}|\rho_s)(|\tilde{p}|^2\rho_c^2 + \rho_{nm}^2)}, \tag{31}$$

and

$$\gamma(k; z, z', L_s) = e^{-k|z-z'|} + \frac{2}{e^{2kL_s} - 1}\{e^{kL_s}\cosh[k(z + z')] + \cosh[k(z - z')]\}, \tag{32}$$

$$\sigma(k; z, z', L_s) = \frac{z - z'}{|z - z'|}e^{-k|z-z'|} - \frac{2}{e^{2kL_s} - 1}\{e^{kL_s}\sinh[k(z + z')] + \sinh[k(z - z')]\}, \tag{33}$$

$$\lambda_p(z, z', L_s) = \frac{2}{L_s}\{(-1)^p\sin[\tilde{p}(z + z')] + \sin[\tilde{p}(z - z')]\}, \tag{34}$$

$$\tau_p(z, z', L_s) = \frac{2}{L_s}\{(-1)^p\cos[\tilde{p}(z + z')] + \cos[\tilde{p}(z - z')]\}, \tag{35}$$

with $\tilde{p} = p\pi/L_s$. A full derivation of these expressions is given in Appendix A. Here, as in Ref. [33], we solve for the unknown Fourier coefficients, (W_{nm}, Q_{nm}), using a least squares minimization with the addition of the power as the regularization parameter. The power P dissipated by a circular planar current source of thickness t and resistivity ϱ is given by

$$P = \frac{\varrho}{t}\int_0^{\rho_c} d\rho'\rho' \int_0^{2\pi} d\phi' |J_\rho(\rho',\phi')|^2 + |J_\phi(\rho',\phi')|^2. \tag{36}$$

Substituting Eq. (25) into Eq. (7) and then Eq. (36), and integrating over the planar surface we find that, for $m = 0$,

$$P = \frac{\varrho}{t}\pi\rho_c^2 \sum_{n=1}^{N} W_{n0}^2 \rho_{n0}^2 J_1(\rho_{n0})^2, \tag{37}$$

and, for $m \in \mathbb{Z}^+$,

$$P = \frac{\varrho}{t}\pi\rho_c^2 \sum_{n=1}^{N}\sum_{m=1}^{M}(W_{nm}^2 + Q_{nm}^2)\left(\frac{\rho_{nm}}{2}\right)^{2m} \frac{1}{m!\,(m-1)!}\left[{}_2\tilde{F}_3\left(m, m+\frac{1}{2}; m+1, m+1, 2m+1; -\rho_{nm}^2\right)\right.$$
$$\left. - \frac{\rho_{nm}^2}{2(m+1)^2}\,{}_3\tilde{F}_4\left(m+\frac{1}{2}, m+1, m+1; m, m+2, m+2, 2m+1; -\rho_{nm}^2\right)\right], \tag{38}$$

where ${}_i\tilde{F}_j$ is the regularized hypergeometric function; see Appendix B for a full derivation. The cost function for the least squares minimization is thus given by

$$\Phi = \sum_{k}^{K}[\mathbf{B}^{\text{desired}}(\mathbf{r}_k) - \mathbf{B}(\mathbf{r}_k)]^2 + \beta P, \tag{39}$$

where β is a weighting parameter chosen to adjust the physical constraints of the system. The cost function is minimized using a least squares fitting to calculate the optimal Fourier coefficients to generate the desired magnetic field at K target points. The minimization is achieved by taking the differential of the cost function with respect to the Fourier coefficients,

$$\frac{\partial\Phi}{\partial W_{ij}} = 0, \qquad \frac{\partial\Phi}{\partial Q_{ij}} = 0, \quad \text{for } i \geq 1, j \geq 0, \tag{40}$$

which enables the optimal Fourier coefficients to be found for any given physical target magnetic field profile through matrix inversion. The inversion process yields the optimal continuous streamfunction defined on the planar surface for a finite number of Fourier coefficients. The number of Fourier coefficients should be chosen and the streamfunction discretized in accordance with previous work [33]. Other optimization methods, such as linear programming, could be used to determine optimal designs to allow for more direct constraints on the field fidelity at specific target points [21,22]. Alternatively, the optimal Fourier coefficients for a specific target region could be found using a numerical procedure such as a particle swarm optimization [36].

III. RESULTS

We now verify our analytical model by designing hybrid active-passive systems composed of biplanar coils inside a closed high-permeability magnetic shield and compare the resulting magnetic field profiles with forward numerical simulations of each optimized system. We consider two distinct systems, each containing current confined to two disks of radius $\rho_c = 0.45$ m and symmetrically placed at $z' = \pm 0.45$ m. Both systems are interior to a perfect closed cylindrical magnetic shield of radius $\rho_s = 0.5$ m and length $L_s = 1$ m centered on the origin, as shown in Fig. 2. The first system is designed to generate a constant transverse field, $\mathbf{B} = B_0\hat{\mathbf{x}}$, and the second system creates a linear field gradient, $\mathbf{B} = (-x\hat{\mathbf{x}} - y\hat{\mathbf{y}} + 2z\hat{\mathbf{z}})$, within an optimization region defined by $-z'/2 \leq z \leq z'/2$ and $0 \leq \rho \leq \rho_c/4$. The magnetic field profiles chosen, i.e., the uniform transverse and linear gradient fields, are examples of tesseral ($m \neq 0$) and zonal ($m = 0$) harmonics,

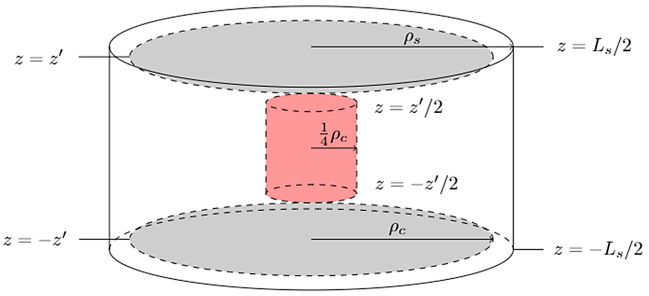


FIG. 2. Schematic diagram showing the areas occupied by the biplanar coils (light gray) inside a cylindrical closed high-permeability magnetic shield (black outline). The high-permeability shield is of length $L_s = 1$ m and radius $\rho_s = 0.5$ m, with planar end caps located at $z = \pm L_s/2$. The shield encloses interior conducting planes of radius $\rho_c = 0.45$ m that are located at $z' = \pm 0.45$ m. The optimization region (red) is bounded along the z axis between the coil planes with top and bottom positions $z = \pm z'/2$, respectively, and extends radially between $\rho = [0, \rho_c/4]$.

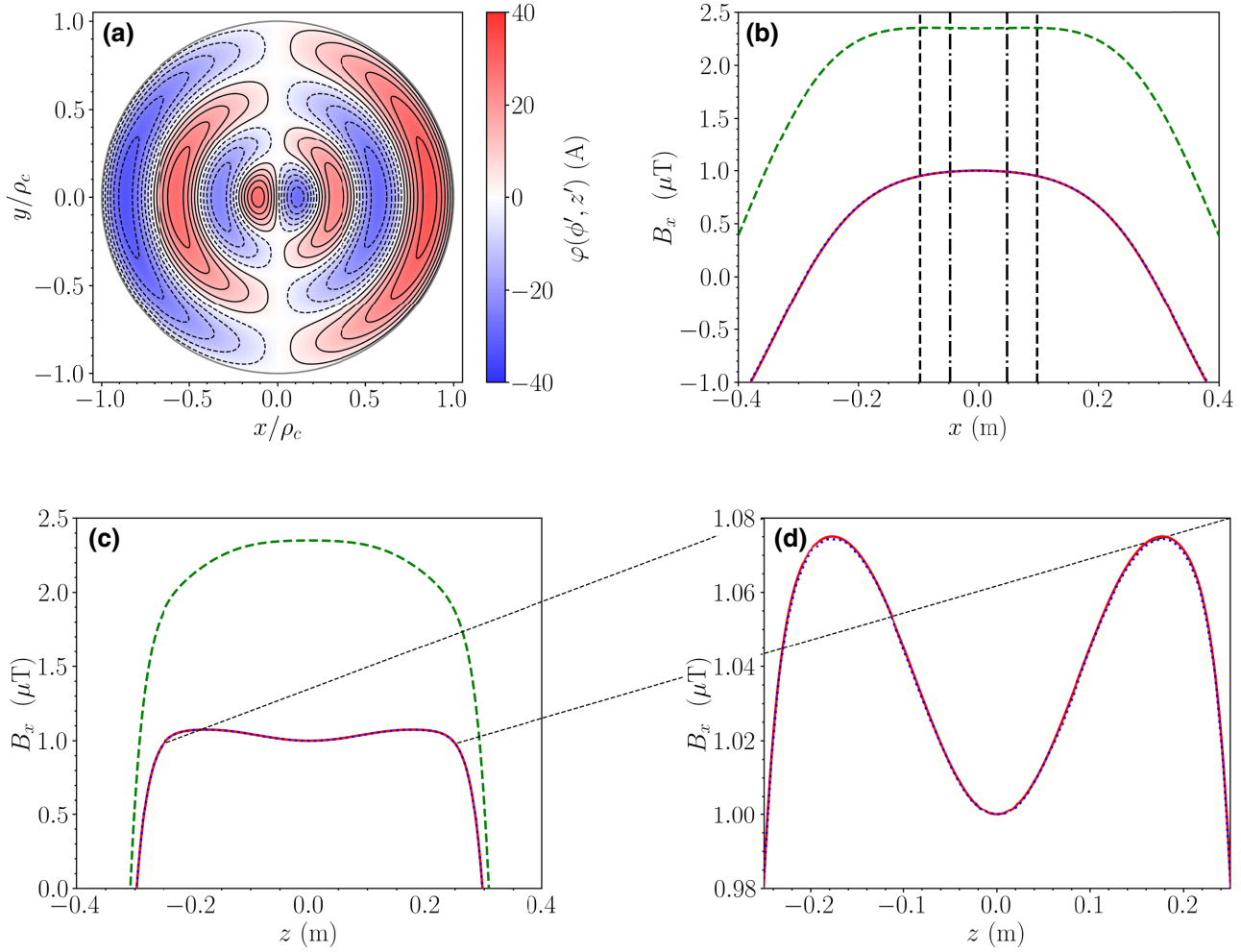


FIG. 3. Wire layouts (a) and performance (b)–(d) of a hybrid active-passive system optimized to generate a constant transverse magnetic field, B_x. Current flows on the surface of two disks of radius $\rho_c = 0.45$ m, which are separated symmetrically from the origin and lie at $z' = \pm 0.45$ m. The wire layouts are optimized to generate a constant transverse field, $B_0 = 1$ μT, across the cylinder and normal to its axis of symmetry. The current-carrying planes are placed symmetrically inside a perfect closed magnetic shield of radius $\rho_s = 0.5$ m and length $L_s = 1$ m and the magnetic field is optimized between $\rho = [0, \rho_c/4]$ and $z = \pm z'/2$, as shown in Fig. 2. The least squares optimization is performed with parameters $N = 50$, $M = 1$, $\beta = 1.77 \times 10^{-9}$ T^2/W, $t = 0.5$ mm, and $\rho = 1.68 \times 10^{-8}$ Ωm. (a) Color map of the optimal current streamfunction calculated for the upper current-carrying plane in Fig. 2. Blue and red shaded regions correspond to current counterflows and their intensity shows the streamfunction magnitude from low (white) to high (intense color). Solid and dashed black curves represent discrete wires with opposite senses of current flow, approximating the current continuum with $N_\varphi = 12$ global contour levels. Streamfunction on the lower light gray plane in Fig. 2 is geometrically identical but the current direction is reversed. (b) Transverse magnetic field, B_x, calculated versus transverse position, x, for $y = z = 0$, from the current continuum in (a) in three ways: analytically using Eqs. (26)–(28) (solid red curve); numerically using COMSOL Multiphysics version 5.5a, modeling the high-permeability cylinder as a perfect magnetic conductor (blue dotted curve); numerically *without* the high-permeability cylinder and using the Biot-Savart law with $N_\varphi = 100$ contour levels (dashed green curve). Black lines enclose the regions where the calculated field deviates from the target field by 5% (dashed) and 1% (dash-dot). (c) Transverse magnetic field, B_x, calculated versus axial position, z, for $x = y = 0$, from the current continuum in the same three ways as for (b). (d) Enlarged section of (c) showing good agreement between the numerical and analytical results throughout the optimization region.

respectively, which exhibit m-fold and complete azimuthal symmetry [37], which facilitates analysis of the shield's particular response to tesseral and zonal harmonic fields generated by planar current sources. The two systems that we consider here are chosen to illustrate targeted magnetic field compensation in situations where compact systems are required, but space inside the central cylindrical cavity of the system is limited by the presence of experimental equipment (e.g., magnetic sensors). Coil designs generating other field profiles, for example using

combinations of planar coils with varying sizes, can be found in Appendix C. All designs can be replicated using our open-access PYTHON code [38].

In Figs. 3(a) and 5(a), we show the optimized contoured streamfunctions for the constant transverse and linear field gradient systems, respectively. Because of the symmetric placement of the biplanar coil systems and optimized field regions within the shield (see Fig. 2), the magnitudes of the streamfunctions defined on both coils are identical. The current flow directions, however, are opposite, due to the form of the desired fields. Figures 3(b)–3(d) show the transverse magnetic field, $B_0 = 1\ \mu$T, along the x axis and z axis, respectively, generated by the biplanar coil design shown in Fig. 3(a) calculated in three different ways: analytically using Eqs. (26)–(28) (solid red curves); numerically using COMSOL Multiphysics® with the shield treated as a perfect magnetic conductor (blue dotted curves); numerically in free space, i.e., excluding the high-permeability material and evaluating the magnetic fields through the Biot-Savart law for discretized biplanar coils with $N_\varphi = 100$ (dashed green curve). Furthermore, color maps of the transverse and axial magnetic field components in the $x - z$ plane are presented in Figs. 4(a) and 4(b), respectively, calculated numerically using COMSOL Multiphysics with the shield treated as a perfect magnetic conductor. Similarly, Figs. 5(b) and 5(c) show the field gradients, $dB_x/dx = -1\ \mu$T/m and $dB_z/dz = 2\ \mu$T/m, along the x axis and z axis, respectively, generated by the biplanar coil system shown in Fig. 5(a) in the same three cases with similar color maps of the magnetic field components in the x-z plane shown in Figs. 6(a) and 6(b). For both designs, the analytical field profiles agree well with numerical simulations. The maximum errors between the analytical model and numerical simulation are 0.052% and 0.043% for the constant transverse field and the gradient of the linear gradient field, respectively, along the z axis of the optimization region. The error between these results could be decreased by reducing the mesh size at a cost of increased computational effort. Here, the mesh size has been adapted so that the maximum difference between the analytical and numerical results is minimized, in line with previous work [33], and, crucially, is below the error introduced from the perfect magnetic conducting shield approximation [34,35].

To quantify the performance of our optimization procedure, we can analyze the deviations between the magnetic fields generated by our theoretical model and the desired target fields. Examining the fidelity of the fields generated by both systems along the x axis of the optimization region, the maximum absolute deviations from the constant transverse and linear axial gradient fields are 6.78% and 0.380%, respectively. Along the z axis of the optimization region, the maximum deviations are 7.50% and 0.306%, respectively. Clearly, the axial field gradient is generated more accurately than the uniform transverse

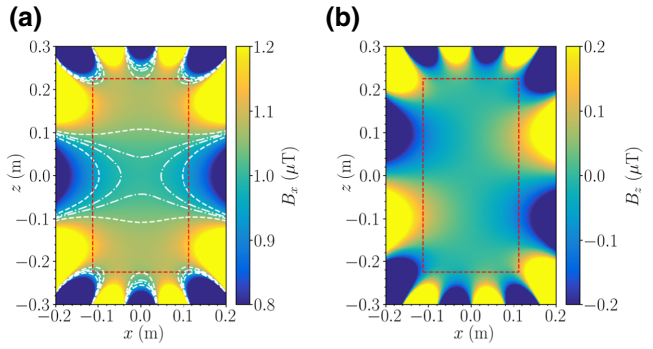


FIG. 4. Color maps showing the magnitude of the magnetic field, in the x-z plane inside a closed finite-length perfect magnetic conductor generated by the active-passive system depicted in Fig. 3: (a) transverse component, B_x, and (b) axial component, B_z. The field profiles are calculated numerically using COMSOL Multiphysics version 5.5a. The magnetic field is optimized between $\rho = [0, \rho_c/4]$ and $z = \pm z'/2$; dashed red lines in (a),(b). Contours, in (a) only, show where the field deviates from the target field by 5% (dashed curves) and 1% (dash-dot curves).

field. This can be seen from Fig. 3(d), which reveals small oscillations in the transverse field along the z axis of the optimization region. To understand the difference between the fidelity of the field profiles generated by the two systems, we must analyze how the passive magnetic shield affects the fields from the planar current distributions, decomposing its response into zonal ($m = 0$) and tesseral ($m \neq 0$) harmonic components. These harmonic responses relate to the variations in the induced pseudocurrent density, corresponding to the planar streamfunction (24), required to satisfy the boundary condition at the shield wall. Schematic approximations of the surface currents for the $m = 0$ zonal and $m = 1$ tesseral harmonic responses can be seen in Fig. 7. For the boundary condition on the cylindrical surface to be satisfied, the induced azimuthal pseudocurrents must mirror azimuthal current paths on the planar coil surfaces, so that the associated fields cancel in the region $\rho_s > \rho > \rho_c$. Since zonal responses are composed of simple circular loops, which can be formed in either a cylindrical or planar basis, the response of the magnetic shield enhances the magnetic field in the optimization region. Consequently, the shield amplifies the axial magnetic field by a factor of 2.39 at the shield's center, as shown in Figs. 5(b) and 5(c). The uniform field gradient therefore exhibits superior fidelity because the continuum response of the passive shield approximates a distributed cylindrical coil. The resulting system, composed of both the coil and shield, completely encloses the interior region, producing a high-fidelity magnetic field gradient.

The tesseral responses are more complicated, with the cylindrical surface of the magnetic shield acting to oppose the magnetic field generated by the planar system in the region $\rho < \rho_s$ due to the formation of saddle-type currents

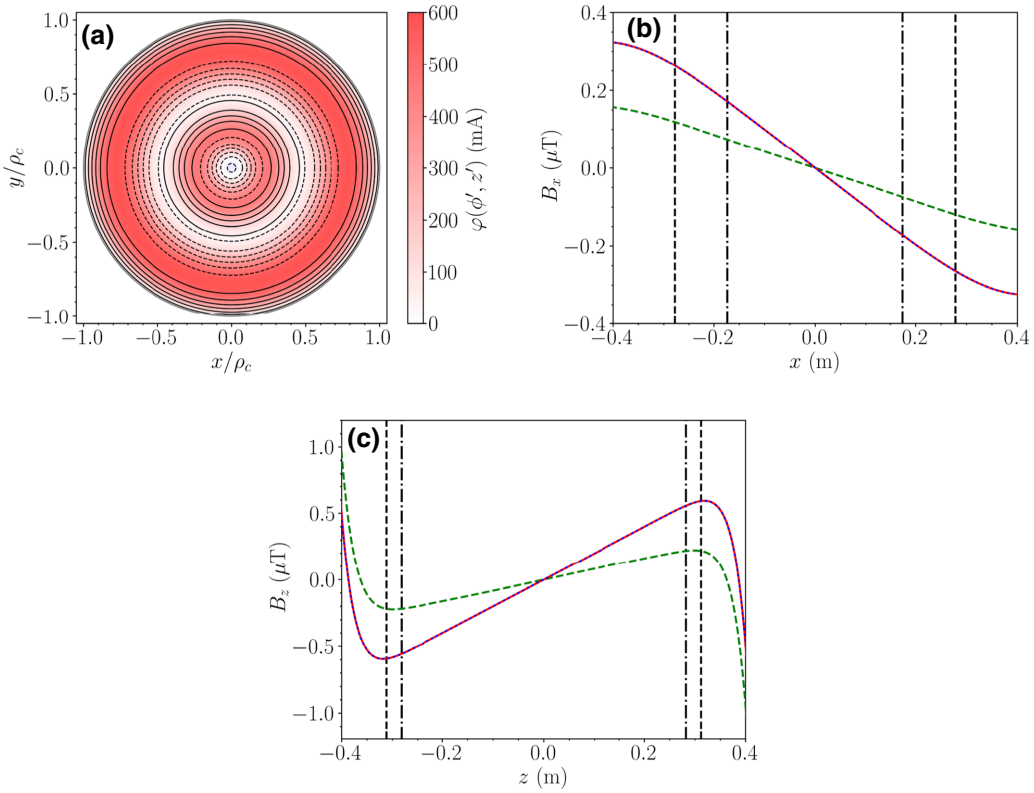


FIG. 5. Wire layouts (a) and performance (b),(c) of a hybrid active-passive system optimized to generate a linear variation of B_z with z position. Current flows on the surface of two disks of radius $\rho_c = 0.45$ m, which are separated symmetrically from the origin and lie at $z' = \pm 0.45$ m. The wire layouts are optimized to generate a linear axial field gradient, $dB_z/dz = 2$ μT/m, along the z axis of the cylinder through the harmonic $\mathbf{B} = (-x\hat{\mathbf{x}} - y\hat{\mathbf{y}} + 2z\hat{\mathbf{z}})$. The current-carrying planes are placed symmetrically inside a perfect closed magnetic shield of radius $\rho_s = 0.5$ m and length $L_s = 1$ m and the magnetic field is optimized between $\rho = [0, \rho_c/4]$ and $z = \pm z'/2$, as shown in Fig. 2. The least squares optimization is performed with parameters $N = 50$, $M = 0$, $\beta = 1.77 \times 10^{-9}$ T^2/W, $t = 0.5$ mm, and $\rho = 1.68 \times 10^{-8}$ Ωm. (a) Color map of the optimal current streamfunction calculated for the upper current-carrying plane in Fig. 2. Intensity of red shaded regions shows the streamfunction magnitude from low (white) to high (intense color). Solid and dashed black curves represent discrete wires with opposite senses of current flow, approximating the current continuum with $N_\varphi = 12$ global contour levels. Streamfunction on the lower light gray plane in Fig. 2 is geometrically identical but the current direction is reversed. (b) Transverse magnetic field, B_x, calculated versus transverse position, x, for $y = z = 0$, from the current continuum in (a) in three ways: analytically using Eqs. (26)–(28) (solid red curve); numerically using COMSOL Multiphysics version 5.5a, modeling the high-permeability cylinder as a perfect magnetic conductor (blue dotted curve); numerically *without* the high-permeability cylinder and using the Biot-Savart law with $N_\varphi = 100$ contour levels (dashed green curve). Black lines enclose the regions where the calculated field deviates from the target field by 5% (dashed) and 1% (dash-dot). (c) Axial magnetic field, B_z, calculated versus axial position, z, for $x = y = 0$, from the current continuum in (a) in the same three ways as for (b).

[37]. These currents result from the required continuity of the induced azimuthal pseudocurrent density in a cylindrical basis. Because of the restricted current flow on the planar surface, the only way to mitigate the opposing field generated by the cylindrical surface of the shield is to minimize the magnetic field at the boundary, resulting in field coil designs that are oscillatory, as seen in Fig. 3(a). The response of the passive shield, for this configuration, reduces the magnetic field by a factor of 2.41 at the shield's center, as shown in Figs. 3(b) and 3(c).

The shield's response not only makes the optimization of tesseral harmonic fields more difficult in regions close to the cylindrical surface of the magnetic shield, but also has an effect on the level of fidelity that can be achieved over any region when the coils are in close proximity to the magnetic shield. To demonstrate this, we investigate the fidelity of the constant transverse field generated by optimized biplanar coils, similar to those in Fig. 3, within a magnetic shield whose radius varies over the range $\rho_s = [\rho_c, 3\rho_c]$. In Fig. 8(a) we plot field profiles at selected shield radii to show how the uniformity of the transverse field along the x axis improves as the radius of the shield increases, as expected, due to the reduced inhomogeneities introduced by the cylindrical surface of the magnetic shield at distances further from the field coils. To evaluate the deviation in the field uniformity, we can calculate the mean

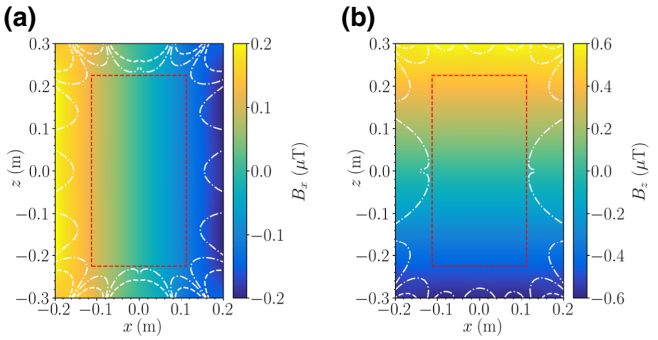


FIG. 6. Color maps showing the magnitude of the magnetic field, in the x-z plane inside a closed finite-length perfect magnetic conductor generated by the active-passive system depicted in Fig. 5: (a) transverse component, B_x, and (b) axial component, B_z. The field profiles are calculated numerically using COMSOL Multiphysics version 5.5a. The magnetic field is optimized between $\rho = [0, \rho_c/4]$ and $z = \pm z'/2$; dashed red lines in (a),(b). Contours show where the field deviates from the target field by 5% (dashed curves) and 1% (dash-dot curves).

rms error, which represents the averaged deviation of the transverse field from perfect uniformity. In Fig. 8(b), we evaluate the mean rms error in the transverse field along the z axis of the optimization region as the radius of the magnetic shield increases. The uniformity of the optimized fields in Figs. 8(a) and 8(b) initially decreases rapidly as the radius of the magnetic shield increases, but approaches the wide shield limit when $\rho_s \sim 2\rho_c$, at which point the field generated by the cylindrical surface of the magnetic shield becomes negligible. In the wide shield limit the predominant contribution from the magnetic shield can then be approximated through the use of the method of mirror images from two infinite parallel perfect magnetic conductors.

Although the pseudocurrents do not exist physically, analysis of the magnetic fields generated by the shield in response to the planar coils gives insight into how such coils should be designed in order to best realize a specified target field. For example, generating magnetic fields that require coil geometries with m-fold azimuthal symmetry causes the cylindrical surface of the magnetic shield to oppose the magnetic field generated by the planar coil. Consequently, if a tesseral field is required over a large radial region, the distance from this region to the planar coils and from the cylindrical shield surface should be minimized and maximized, respectively. The opposite is true for the fields generated by the planar end caps of the shield. When the biplanar coils are located near the end caps, where $-L_s/2 < -z' < z < z' < L_s/2$, but radially distant from the cylindrical surface of the magnetic shield, the reflected pseudocurrents generated by the method of mirror

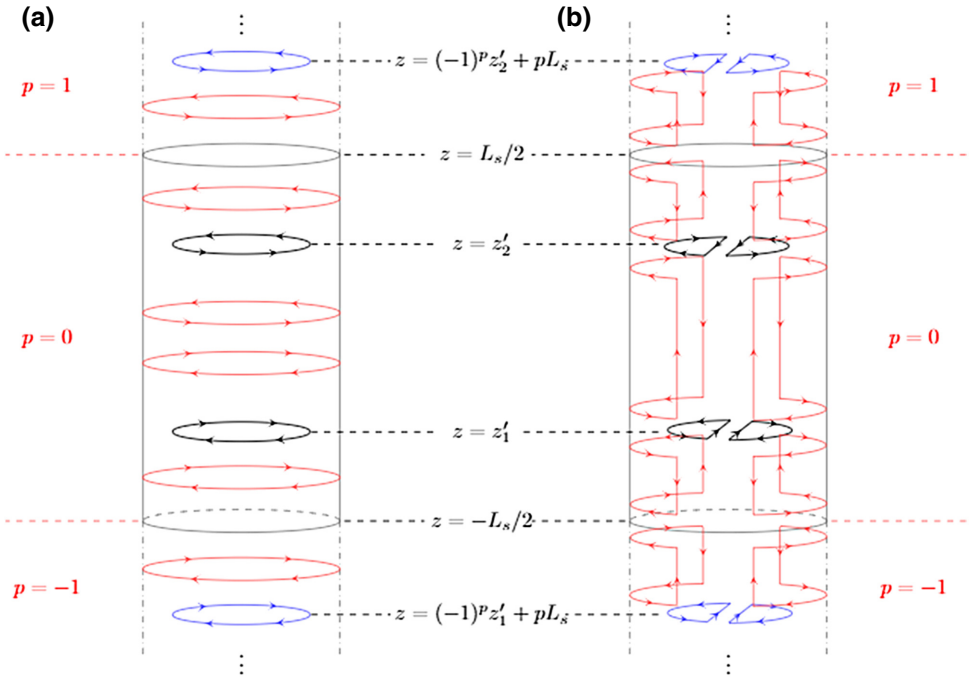


FIG. 7. Schematic diagram showing how the approximate zonal (a) and tesseral (b) harmonic responses are generated by simple current loops with cylindrical and m-fold azimuthal symmetries, respectively. The discrete current loops (black) are located at $z = z_1'$ and $z = z_2'$ with their pth reflected pseudoimage currents (red) generated by the surface of the cylindrical shield at $\rho = \rho_s$ and by the planar end caps at $z = \pm L_s/2$, in accordance with the method of images described by Eq. (24). Images of the two planar (black) coils resulting from the end caps are located at $z = (-1)^p z_1' + pL_s$ and $z = (-1)^p z_2' + pL_s$, respectively, where $p \in \mathbb{Z}$ (two such image coils are shown blue). For all odd reflections, the axial current direction is reversed.

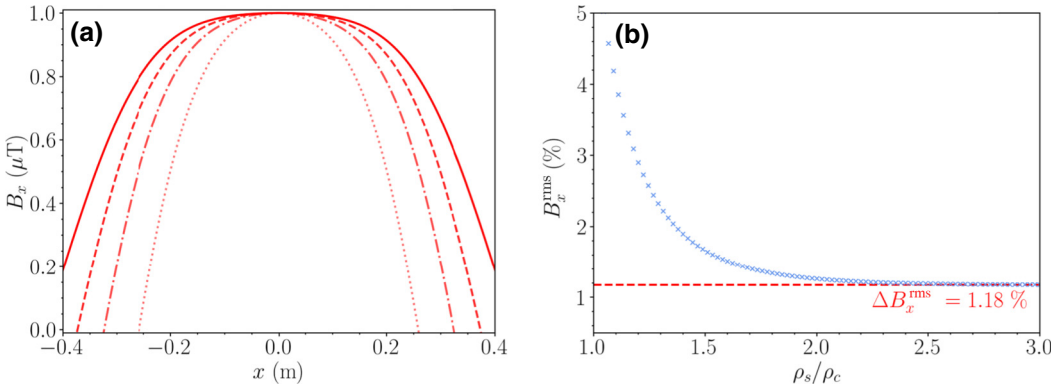


FIG. 8. Improvement in the performance of a hybrid active-passive system, optimized to generate a constant transverse field $B_0 = 1\ \mu$T, upon increasing the radius of the passive shield. Current flows on the surface of two disks of radius $\rho_c = 0.45$ m, which are separated symmetrically from the origin and lie at $z' = \pm 0.45$ m. The wire layouts are optimized to generate constant $B_0 = 1\ \mu$T between $\rho = [0, \rho_c/4]$ and $z = \pm z'/2$, as shown in Fig. 2. The current-carrying planes lie within the bore of a perfect closed magnetic shield of radius $\rho_s = [\rho_c, 3\rho_c]$ and length $L_s = 1$ m. Each least squares optimization is performed with parameters $N = 50$, $M = 1$, $\beta = 1.77 \times 10^{-9}$ T^2/W, $t = 0.5$ mm, and $\rho = 1.68 \times 10^{-8}$ Ωm. (a) Transverse magnetic field, B_x, calculated analytically versus transverse position, x, using Eqs. (26)–(28) (red curves), where $\rho_s/\rho_c = 1.01$ (dotted curve), $\rho_s/\rho_c = 1.25$ (dash-dot curve), $\rho_s/\rho_c = 1.5$ (dashed curve), and $\rho_s/\rho_c = 2.5$ (solid curve). (b) Root mean square (rms) deviation, $\Delta B_x^{\rm rms}$, between the calculated and target fields evaluated along the axis of the optimized field region and plotted as a function of ρ_s/ρ_c. Light blue crosses show $\Delta B_x^{\rm rms}$ values calculated analytically using Eqs. (26)–(28). Horizontal dashed red line shows the analytical value of $\Delta B_x^{\rm rms} = 1.18\%$ obtained in the wide shield limit ($\rho_s/\rho_c \gg 1$).

images provide a field similar to that of the planar coils, resulting in a field that is magnified. Consequently, biplanar coils are desirable in magnetic shields with large radii and small aspect ratios, $L_s/(2\rho_s) < 0.5$. In comparison, the magnetic field generated by the shield in response to coils contained on a *cylindrical* surface [33] shows the opposite effect. Tesseral fields generated by cylindrical coils are enhanced by the cylindrical surface and are reduced by the planar end caps, favoring long magnetic shields with $L_s/(2\rho_s) > 0.5$. Because of the conflicting conditions on the geometries (i.e., planar or cylindrical) of the coils and the magnetic shield, a system composed of coupled planar and cylindrical coils may have advantages for generating desired tesseral field profiles with the greatest accuracy.

Intrinsic inaccuracies in calculating the optimum current density and approximating the current continuum by discrete wires are not the only sources of error that must be considered when designing fields using our method. Particularly for the tesseral harmonic field generating coils, wire patterns may be highly meandering, making them hard to manufacture and, due to their high resistance, power consuming. When manufacturing these systems, the achievable field fidelity is limited by the discretization of the continuum current flow pattern and by the creation of magnetic dipoles via the interaction between separate current streamlines and the wires that follow them. Fortunately, new ways to realize the current continuum are emerging due to advances in foldable printed circuit boards [39] and three-dimensional printing technologies [40], which enable more complex coils to be made accurately. It should also be noted that approximating a perfect magnetic shield by a material of finite permeability $\mu_r = 20\,000$ and thickness $d = 1$ mm only introduces small deviations in the model of 0.005% [33], which is much less than the error introduced in the desired field by the coil designs. As a result, given an accurate representation of the current continuum, our methodology can be used reliably to generate target magnetic fields in high-permeability environments. The PYTHON code used to design arbitrary the planar coils in a magnetically shielded cylinder is openly available from GitHub and can be cited at Ref. [38]. Verification using COMSOL Multiphysics requires a valid license.

IV. CONCLUSION

Here we formulate an analytical model to calculate the magnetic field generated by an arbitrary static current distribution confined to a plane whose normal is parallel to the axis of a finite closed high-permeability cylinder. Our formalism is based on a Green's function expansion of the vector potential generated by a planar coil system. To satisfy the boundary conditions at the surface of the cylinder, we assume that it is a perfect magnetic conductor and express the induced magnetization in terms of a pseudocurrent density. Because of the shared azimuthal symmetries of the planar current flows and the induced pseudocurrent on the cylindrical surface of the magnetic shield, the response of the magnetic shield can be expressed in terms of the planar current distribution. We use this formalism to enable *a priori* optimization of the planar current

distribution required to generate specified target magnetic field profiles by combining a Fourier-Bessel decomposition of the current flow with a quadratic minimization procedure.

We demonstrate this optimization methodology by using it to design biplanar coils that accurately generate a constant transverse field, B_x, across the cylinder, and a linear gradient field, dB_z/dz, along the axis of the cylinder. Predictions from our analytical model agree well with subsequent forward finite element simulations, validating our methodology. We quantify the interaction of planar systems with a closed finite high-permeability cylinder and find that all coil designs without complete azimuthal symmetry induce magnetic fields in the cylindrical surface of the shield that opposed the field generated by the planar current source. Conversely, planar end caps have the opposite effect and amplify the field from the planar current source.

Our analytical model and optimization procedure extends the range of current geometries that can be tailored within finite closed cylindrical magnetic shields in order to accurately generate specified target field profiles. This enables the development of systems that require the best magnetic field control that can be achieved subject to size, weight, power, and cost constraints. It may also enable hybrid active-passive planar coils to be retrofitted to existing cylindrical magnetic shields in order to improve their performance for a low cost and without disrupting existing experimental setups. In the future, combining planar and cylindrical coils could enable ultraprecise magnetic fields to be generated through even larger interior fractions of magnetic shields.

ACKNOWLEDGMENTS

We acknowledge support from the UK Quantum Technology Hub Sensors and Timing, funded by the Engineering and Physical Sciences Research Council (EP/M013294/1). M.P., P.J.H., T.M.F., M.J.B., and R.B. declare that they have a patent pending to the UK Government Intellectual Property Office (Application No. 1913549.0) regarding the magnetic field optimization techniques described in this work. N.H., M.J.B., and R.B. also declare financial interests in a University of Nottingham spin-out company, Cerca. The authors have no other competing financial interests.

APPENDIX A: MAGNETIC FIELD DERIVATION

In order to calculate the magnetic field, we must first determine both the Fourier transform of the streamfunction and the induced Fourier pseudocurrent density. Substituting Eq. (25) into Eq. (12) and integrating over the azimuthal angle yields

$$\varphi^m(k) = \frac{\rho_c}{2}\sum_{n=1}^{N}\sum_{m'=0}^{M}[W_{nm'}(\delta_{mm'}+\delta_{m,-m'}) - iQ_{nm'}(\delta_{mm'}-\delta_{m,-m'})]\int_0^{\rho_c} d\rho'\,\rho' J_m(k\rho')J_{m'}\left(\frac{\rho_{nm'}\rho'}{\rho_c}\right). \tag{A1}$$

Upon substituting Eq. (A1) into the expressions for the magnetic field, Eqs. (20)–(22), the δ functions collapse the infinite summation, resulting in every Bessel function of order m being replaced by one of order m'. Hence, without loss of generality, applying a Bessel function product identity (Eq. 5.54.1 in Ref. [41]), we may now write

$$\varphi^m(k) = \frac{\rho_c^3}{2}\sum_{n=1}^{N}\sum_{m'=0}^{M}[W_{nm'}(\delta_{mm'}+\delta_{m,-m'}) - iQ_{nm'}(\delta_{mm'}-\delta_{m,-m'})]\frac{\rho_{nm'}}{k^2\rho_c^2-\rho_{nm'}^2}J_{m'}(k\rho_c)J'_{m'}(\rho_{nm'}). \tag{A2}$$

Similarly, we may also calculate the induced Fourier pseudocurrent density. Substituting Eq. (25) into Eq. (24) and integrating over the azimuthal coordinate yields

$$\begin{aligned} J_\phi^{mp}(k) = {} & \frac{\rho_c e^{-ik[(-1)^p z'+pL_s]}}{2\rho_s|k|I_m(|k|\rho_s)K'_m(|k|\rho_s)}\sum_{n=1}^{N}\sum_{m'=0}^{M}[W_{nm'}(\delta_{mm'}+\delta_{m,-m'}) - iQ_{nm'}(\delta_{mm'}-\delta_{m,-m'})] \\ & \times\int_0^{\infty} d\tilde{k}\frac{\tilde{k}^3}{\tilde{k}^2+k^2}J_m(\tilde{k}\rho_s)\int_0^{\rho_c} d\rho'\rho' J_{m'}(\tilde{k}\rho')J_{m'}\left(\frac{\rho_{nm'}\rho'}{\rho_c}\right). \end{aligned} \tag{A3}$$

To simplify these expressions, we evaluate the integral over $\tilde{k}$ first and then separate the integrand using partial fractions to yield

$$\int_0^{\infty} d\tilde{k}\frac{\tilde{k}^3}{\tilde{k}^2+k^2}J_m(\tilde{k}\rho_s)J_m(\tilde{k}\rho') = \int_0^{\infty} d\tilde{k}\,\tilde{k}J_m(\tilde{k}\rho_s)J_m(\tilde{k}\rho') - k^2\int_0^{\infty} d\tilde{k}\,\frac{\tilde{k}}{\tilde{k}^2+k^2}J_m(\tilde{k}\rho_s)J_m(\tilde{k}\rho'). \tag{A4}$$

Inspecting Eq. (A4) we see that the first component is simply the orthogonality relation between Bessel functions, and the second has a known solution (Eq. 6.541.1 in [41]). Hence, we can state that

$$\int_0^\infty d\tilde{k}\,\frac{\tilde{k}^3}{\tilde{k}^2+k^2}J_m(\tilde{k}\rho_s)J_m(\tilde{k}\rho') = \frac{\delta(\rho'-\rho_s)}{\rho'} - k^2 I_{m'}(|k|\rho')K_{m'}(|k|\rho_s). \tag{A5}$$

However, since $\rho' < \rho_s$, the first term in Eq. (A5) can be neglected. Inserting Eq. (A5) into Eq. (A3) and integrating over ρ' results in the expression

$$\begin{aligned} J_\phi^{mp}(k) = {} & \frac{\rho_c k^2 e^{-ik[(-1)^p z' + pL_s]}}{2\rho_s|k|I_m(|k|\rho_s)K_m'(|k|\rho_s)} \sum_{n=1}^{N}\sum_{m'=0}^{M}[W_{nm'}(\delta_{mm'}+\delta_{m,-m'}) - iQ_{nm'}(\delta_{mm'}-\delta_{m,-m'})] \\ & \times \frac{\rho_{nm'}}{k^2\rho_c^2+\rho_{nm'}^2} J_{m'}'(\rho_{nm'})I_{m'}(|k|\rho_c)K_{m'}(|k|\rho_s). \end{aligned} \tag{A6}$$

Substituting Eqs. (A2) and (A6) into Eqs. (20)–(22), we can express the summation over the exponentials associated with the infinite reflections of the planar streamfunction as

$$\sum_{p=-\infty}^{\infty} e^{-k|z-(-1)^p z'+pL_s|} = e^{-k|z-z'|} + \frac{2}{e^{2kL}-1}\{e^{kL}\cosh[k(z+z')] + \cosh[k(z-z')]\} \tag{A7}$$

and

$$\begin{aligned} & \sum_{p=-\infty}^{\infty} \frac{z-(-1)^p z'+pL_s}{|z-(-1)^p z'+pL_s|} e^{-k|z-(-1)^p z'+pL_s|} \\ & \quad = \frac{z-z'}{|z-z'|}e^{-k|z-z'|} - \frac{2}{e^{2kL}-1}\{e^{kL}\sinh[k(z+z')] + \sinh[k(z-z')]\}. \end{aligned} \tag{A8}$$

Similarly, the summation over the infinite pseudocurrent reflections can be written as a Fourier series expansion,

$$\sum_{p=-\infty}^{\infty} e^{ik[z-(-1)^p z'+pL_s]} = \frac{\pi}{L}\sum_{p=-\infty}^{\infty}\delta\left(k-\frac{p\pi}{L}\right)(e^{ik(z+z'-L)} + e^{ik(z-z')}). \tag{A9}$$

Using these expansions, we may finally write

$$B_\rho(\rho,\phi,z) = \frac{\mu_0\rho_c^3}{2}\sum_{n=1}^{N}\sum_{m=0}^{M}\rho_{nm}J_m'(\rho_{nm})[W_{nm}\cos(m\phi) + Q_{nm}\sin(m\phi)]B_\rho^{nm}(\rho,z), \tag{A10}$$

$$B_\phi(\rho,\phi,z) = \frac{\mu_0\rho_c^3}{2\rho}\sum_{n=1}^{N}\sum_{m=0}^{M}m\rho_{nm}J_m'(\rho_{nm})[W_{nm}\sin(m\phi) - Q_{nm}\cos(m\phi)]B_\phi^{nm}(\rho,z), \tag{A11}$$

$$B_z(\rho,\phi,z) = \frac{\mu_0\rho_c^3}{2}\sum_{n=1}^{N}\sum_{m=0}^{M}\rho_{nm}J_m'(\rho_{nm})[W_{nm}\cos(m\phi) + Q_{nm}\sin(m\phi)]B_z^{nm}(\rho,z), \tag{A12}$$

where

$$B_\rho^{nm}(\rho,z) = -\int_0^\infty dk\,k^2\sigma(k;z,z',L_s)\frac{J_m'(k\rho)J_m(k\rho_c)}{k^2\rho_c^2-\rho_{nm}^2} - \sum_{p=1}^{\infty}\tilde{p}|\tilde{p}|\lambda_p(z,z',L_s)\frac{I_m'(|\tilde{p}|\rho)I_m(|\tilde{p}|\rho_c)K_m(|\tilde{p}|\rho_s)}{I_m(|\tilde{p}|\rho_s)(|\tilde{p}|^2\rho_c^2+\rho_{nm}^2)}, \tag{A13}$$

$$B_{\phi}^{nm}(\rho,z) = \int_0^{\infty} dk\, k\sigma(k;z,z',L_s)\frac{J_m(k\rho)J_m(k\rho_c)}{k^2\rho_c^2-\rho_{nm}^2} + \sum_{p=1}^{\infty}\tilde{p}\lambda_p(z,z',L_s)\frac{I_m(|\tilde{p}|\rho)I_m(|\tilde{p}|\rho_c)K_m(|\tilde{p}|\rho_s)}{I_m(|\tilde{p}|\rho_s)(|\tilde{p}|^2\rho_c^2+\rho_{nm}^2)}, \tag{A14}$$

$$B_{z}^{nm}(\rho,z) = \int_0^{\infty} dk\, k^2\gamma(k;z,z',L_s)\frac{J_m(k\rho)J_m(k\rho_c)}{k^2\rho_c^2-\rho_{nm}^2} - \sum_{p=1}^{\infty}\tilde{p}^2\tau_p(z,z',L_s)\frac{I_m(|\tilde{p}|\rho)I_m(|\tilde{p}|\rho_c)K_m(|\tilde{p}|\rho_s)}{I_m(|\tilde{p}|\rho_s)(|\tilde{p}|^2\rho_c^2+\rho_{nm}^2)}, \tag{A15}$$

where

$$\gamma(k;z,z',L_s) = e^{-k|z-z'|} + \frac{2}{e^{2kL_s}-1}\{e^{kL_s}\cosh[k(z+z')] + \cosh[k(z-z')]\}, \tag{A16}$$

$$\sigma(k;z,z',L_s) = \frac{z-z'}{|z-z'|}e^{-k|z-z'|} - \frac{2}{e^{2kL_s}-1}\{e^{kL_s}\sinh[k(z+z')] + \sinh[k(z-z')]\}, \tag{A17}$$

$$\lambda_p(z,z',L_s) = \frac{2}{L_s}\{(-1)^p\sin[\tilde{p}(z+z')] + \sin[\tilde{p}(z-z')]\}, \tag{A18}$$

$$\tau_p(z,z',L_s) = \frac{2}{L_s}\{(-1)^p\cos[\tilde{p}(z+z')] + \cos[\tilde{p}(z-z')]\}, \tag{A19}$$

and $\tilde{p} = p\pi/L_s$.

APPENDIX B: POWER DISSIPATION

The power dissipated in the surface of a circular planar current source of thickness t and resistivity ϱ is given by

$$P = \frac{\varrho}{t}\int_0^{\rho_c} d\rho'\rho'\int_0^{2\pi} d\phi'\ |J_\rho(\rho',\phi')|^2 + |J_\phi(\rho',\phi')|^2. \tag{B1}$$

We can substitute the streamfunction (25) into the continuity relations (7) to obtain

$$J_\rho(\rho',\phi') = [H(\rho'-\rho_c) - H(\rho')]\frac{\rho_c}{\rho'}\sum_{n=1}^{N}\sum_{m=0}^{M} mJ_m\left(\frac{\rho_{nm}\rho'}{\rho_c}\right)[W_{nm}\sin(m\phi') - Q_{nm}\cos(m\phi')], \tag{B2}$$

$$J_\phi(\rho',\phi') = [H(\rho'-\rho_c) - H(\rho')]\sum_{n=1}^{N}\sum_{m=0}^{M}\rho_{nm}J'_m\left(\frac{\rho_{nm}\rho'}{\rho_c}\right)[W_{nm}\cos(m\phi') + Q_{nm}\sin(m\phi')]. \tag{B3}$$

Inserting Eqs. (B2) and (B3) into Eq. (B1) and integrating over the azimuthal component results in

$$\begin{aligned} P = {} & \frac{\varrho}{t}\pi\rho_c^2\sum_{n=1}^{N}\sum_{m=0}^{M}[(1+\delta_{m0})W_{nm}^2 + (1-\delta_{m0})Q_{nm}^2] \\ & \times\int_0^1 d\tilde{\rho}\left[\frac{2m^2}{\tilde{\rho}}J_m(\rho_{nm}\tilde{\rho})^2 - \rho_{nm}^2\tilde{\rho}J_{m-1}(\rho_{nm}\tilde{\rho})J_{m+1}(\rho_{nm}\tilde{\rho})\right], \end{aligned} \tag{B4}$$

which, when integrated over the radial component, can be expressed as

$$P = \frac{\varrho}{t}\pi\rho_c^2\sum_{n=1}^{N}W_{n0}^2\rho_{n0}^2J_1(\rho_{n0})^2 \tag{B5}$$

for $m = 0$, and

$$\begin{aligned} P = {} & \frac{\varrho}{t}\pi\rho_c^2\sum_{n=1}^{N}\sum_{m=1}^{M}(W_{nm}^2+Q_{nm}^2)\left(\frac{\rho_{nm}}{2}\right)^{2m}\frac{1}{m!\,(m-1)!}\left[{}_2\tilde{F}_3\left(m,m+\frac{1}{2};m+1,m+1,2m+1;-\rho_{nm}^2\right)\right. \\ & \left. - \frac{\rho_{nm}^2}{2(m+1)^2}\,{}_3\tilde{F}_4\left(m+\frac{1}{2},m+1,m+1;m,m+2,m+2,2m+1;-\rho_{nm}^2\right)\right] \end{aligned} \tag{B6}$$

for $m \in \mathbb{Z}^+$, where ${}_i\tilde{F}_j$ is the regularized hypergeometric function. Some specific evaluations of Eq. (B6) are

$$P = \frac{\varrho}{2t}\pi\rho_c^2 \sum_{n=1}^{N}(W_{n1}^2 + Q_{n1}^2)\rho_{n1}^2 J_0(\rho_{n1})^2 \quad \text{for } m = 1, \tag{B7}$$

$$P = \frac{\varrho}{2t}\pi\rho_c^2 \sum_{n=1}^{N}(W_{n2}^2 + Q_{n2}^2)\left[(\rho_{n2}^2 - 4)J_0(\rho_{n2})^2 - \frac{2(\rho_{n2}^2 - 8)}{\rho_{n2}}J_0(\rho_{n2})J_1(\rho_{n2}) + \frac{\rho_{n2}^4 - 16}{\rho_{n2}^2}J_1(\rho_{n2})^2\right] \quad \text{for } m = 2, \tag{B8}$$

$$P = \frac{\varrho}{2t}\pi\rho_c^2 \sum_{n=1}^{N}(W_{n3}^2 + Q_{n3}^2)\left[\frac{\rho_{n3}^4 - 96}{\rho_{n3}^2}J_0(\rho_{n3})^2 - 48(\rho_{n3}^2 - 8)\rho_{n3}^3 J_0(\rho_{n3})J_1(\rho_{n3}) + \frac{\rho_{n3}^6 - 10\rho_{n3}^4 + 96\rho_{n3}^2 - 384}{\rho_{n3}^4}J_1(\rho_{n3})^2\right]$$
$$\text{for } m = 3. \tag{B9}$$

APPENDIX C: EXAMPLE COIL DESIGNS

To further validate our design process, in Figs. 9 and 10 we show additional biplanar hybrid active-passive systems and analyze their behavior. These systems are designed using our open-access PYTHON code [38]. The coordinate axes and magnetic field plots are labeled in the same way as the systems presented in the main text. For both systems, the coils lie in the $z' = \pm 0.45$ m planes, as in the main text and shown in Fig. 2, and the fields are optimized along the z axis between $z = \pm z'/2$. The design in Fig. 9 generates a linear transverse field gradient, dB_x/dz, whose spatial variation matches the harmonic $\mathbf{B} = (z\hat{\mathbf{x}} + x\hat{\mathbf{z}})$ between two

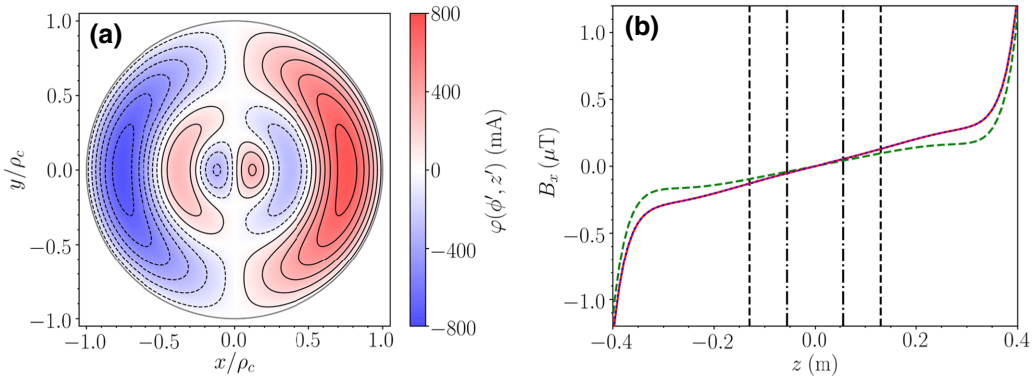


FIG. 9. Wire layouts (a) and performance (b) of a hybrid active-passive system optimized to generate a linear variation of B_x with z position. Current flows on the surface of two disks of radius $\rho_c = 0.45$ m, which are separated symmetrically from the origin and lie at $z' = \pm 0.45$ m. The wire layouts are optimized to generate a linear transverse field gradient, $dB_x/dz = 1$ μT/m, along the z axis of the cylinder through the harmonic field profile $\mathbf{B} = (z\hat{\mathbf{x}} + x\hat{\mathbf{z}})$. The current-carrying planes are placed symmetrically inside a perfect closed magnetic shield of radius $\rho_s = 0.5$ m and length $L_s = 1$ m and the magnetic field is optimized along the z axis between $z = \pm z'/2$. The least squares optimization is performed with parameters $N = 100$, $M = 1$, $\beta = 1.77 \times 10^{-8}$ T^2/W, $t = 0.5$ mm, and $\rho = 1.68 \times 10^{-8}$ Ωm. (a) Color map of the optimal current streamfunction calculated for the upper current-carrying plane in Fig. 2 [blue and red shaded regions correspond to current counterflows and their intensity shows the streamfunction magnitude from low (white) to high (intense color)]. Solid and dashed black curves represent discrete wires with opposite senses of current flow, approximating the current continuum with $N_\varphi = 12$ global contour levels. Streamfunction on the lower light brown plane in Fig. 2 is geometrically identical but the current direction is reversed. (b) Transverse magnetic field, B_x, calculated versus axial position, z, from the current continuum in (a) in three ways: analytically using Eqs. (26)–(28) (solid red curve); numerically using COMSOL Multiphysics version 5.5a, modeling the high-permeability cylinder as a perfect magnetic conductor (blue dotted curve); numerically *without* the high-permeability cylinder and using the Biot-Savart law with $N_\varphi = 100$ contour levels (dashed green curve). Black lines enclose the regions where the axial field gradient deviates by 5% (dashed) and 1% (dash-dot).

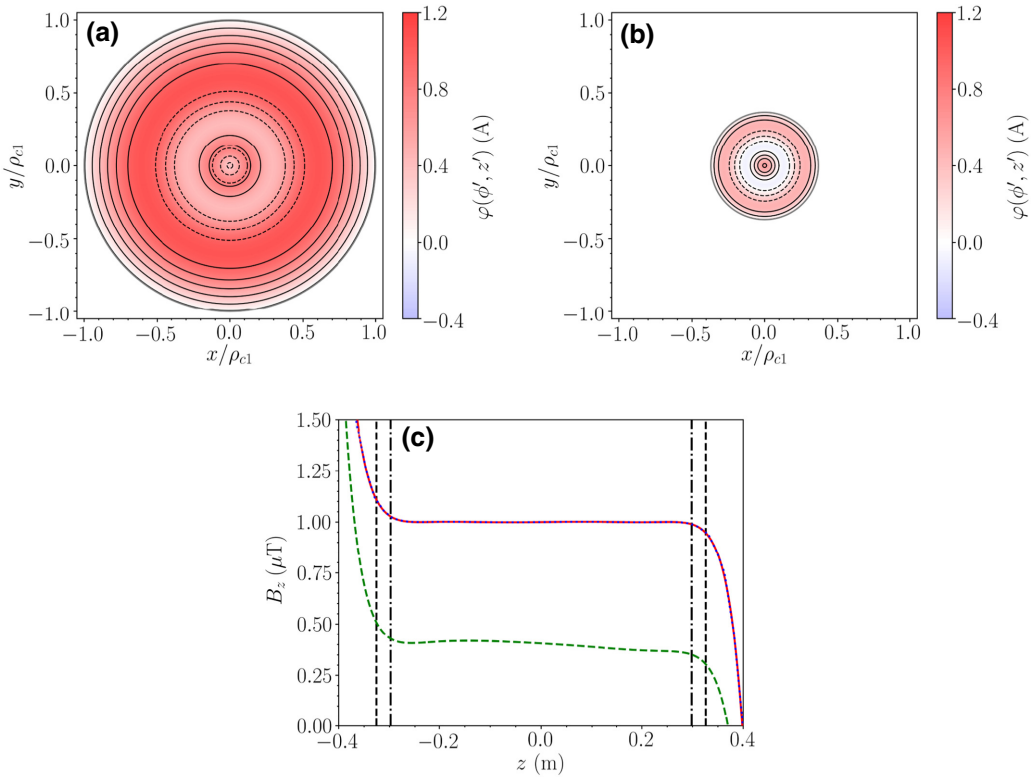


FIG. 10. Wire layouts (a),(b) and performance (c) of a hybrid active-passive linear system optimized to generate a constant axial field, B_z. Current flows on the surface of two disks of radii $\rho_{c1} = 0.95$ m (on the upper current-carrying plane in Fig. 2) and $\rho_{c2} = 0.35$ m (on the lower current-carrying plane in Fig. 2), respectively, which are separated symmetrically from the origin and lie at $z' = \pm 0.45$ m. The wire layouts are optimized to generate a constant axial field, $B_0 = 1$ μT, along the cylinder and parallel to its axis of symmetry. The current-carrying planes are placed symmetrically inside a perfect closed magnetic shield of radius $\rho_s = 1$ m and length $L_s = 1$ m and the magnetic field is optimized along the z axis between $z = \pm z'/2$. The least squares optimization is performed with parameters $N = 100$, $M = 0$, $\beta = 1.77 \times 10^{-8}$, $T^2/W, t = 0.5$ mm, and $\rho = 1.68 \times 10^{-8}$ Ωm. (a),(b) Color maps of the optimal current streamfunction on the upper and lower planar disks, respectively [blue and red shaded regions correspond to current counterflows and their intensity shows the streamfunction magnitude from low (white) to high (intense color)]. Solid and dashed black curves represent discrete wires with opposite senses of current flow, approximating the current continuum with $N_\varphi = 6$ global contour levels. (c) Axial magnetic field, B_z, versus axial position, z, calculated from the current continuum in (a),(b) in three ways: analytically using Eqs. (26)–(28) (solid red curve); numerically using COMSOL Multiphysics version 5.5a, modeling the high-permeability cylinder as a perfect magnetic conductor (blue dotted curve); numerically *without* the high-permeability cylinder and using the Biot-Savart law with $N_\varphi = 100$ contour levels (dashed green curve). Black lines enclose the regions where the axial field gradient deviates by 5% (dashed) and 1% (dash-dot).

identical plates of radius $\rho_c = 0.45$ m, inside a magnetic shield of radius $\rho_s = 0.5$ m and length $L_s = 1$ m. The field gradient is amplified by a factor of 1.06 at the shield's center. If the shield is lengthened, the field gradient is diminished to 0.81 at the shield's center in the long shield limit, as expected from our analysis in the main body of the text. The design in Fig. 10 generates a uniform field, B_z, in the z direction and extending between two planes of different sizes, with upper and lower coil sizes $\rho_{c1} = 0.95$ m and $\rho_{c2} = 0.35$ m, respectively, inside a magnetic shield of radius $\rho_s = 1$ m and length $L_s = 1$ m. Since the shield and coils have a relatively wide form factor, the field is highly uniform, with the region of axial field deviation below 1% extending over more than 70% of the distance between the planes.

[1] X. Wu, Z. Pagel, B. S. Malek, T. H. Nguyen, F. Zi, D. S. Scheirer, and H. Müller, Gravity surveys using a mobile atom interferometer, Sci. Adv. **5**, 9 (2019).

[2] V. Menoret, P. Vermeulen, N. L. Moigne, S. Bonvalot, P. Bouyer, A. Landragin, and B. Desruelle, Gravity measurements below $10^{-}9$ g with a transportable absolute quantum gravimeter, Sci. Rep. **8**, 1 (2018).

[3] M. J. Snadden, J. M. McGuirk, P. Bouyer, K. G. Haritos, and M. A. Kasevich, Measurement of the Earth's Gravity Gradient with an Atom Interferometer-Based Gravity Gradiometer, Phys. Rev. Lett. **81**, 971 (1998).

[4] K. Bongs, M. Holynski, J. Vovrosh, P. Bouyer, G. Condon, E. Rasel, C. Schubert, W. P. Schleich, and A. Roura, Taking atom interferometric quantum sensors from the

laboratory to real-world applications, Nat. Rev. Phys. **1**, 731 (2019).
[5] V. K. Shah and R. T. Wakai, A compact, high performance atomic magnetometer for biomedical applications, Phys. Med. Biol. **58**, 8153 (2013).
[6] E. Boto, N. Holmes, J. Leggett, G. Roberts, V. Shah, S. S. Meyer, L. D. Muñoz, K. J. Mullinger, T. M. Tierney, S. Bestmann, G. R. Barnes, R. Bowtell, and M. J. Brookes, Moving magnetoencephalography towards real-world applications with a wearable system, Nature **555**, 657 (2018).
[7] R. M. Hill, E. Boto, M. Rea, N. Holmes, J. Leggett, L. A. Coles, M. Papastavrou, S. K. Everton, B. A. E. Hunt, D. Sims, J. Osborne, V. Shah, R. Bowtell, and M. J. Brookes, Multi-channel whole-head OPM-MEG: Helmet design and a comparison with a conventional system, NeuroImage **219**, 116995 (2020).
[8] T. M. Tierney, N. Holmes, S. Mellor, J. D. López, G. Roberts, R. M. Hill, E. Boto, J. Leggett, V. Shah, M. J. Brookes, R. Bowtell, and G. R. Barnes, Optically pumped magnetometers: From quantum origins to multi-channel magnetoencephalography, NeuroImage **199**, 598 (2019).
[9] A. Borna, T. R. Carter, A. P. Colombo, Y.-Y. Jau, J. McKay, M. Weisend, S. Taulu, J. M. Stephen, and P. D. D. Schwindt, Non-invasive functional-brain-imaging with an OPM-based magnetoencephalography system, PLoS ONE **15**, 1 (2020).
[10] H. Eswaran, D. Escalona-Vargas, E. H. Bolin, J. D. Wilson, and C. L. Lowery, Fetal magnetocardiography using optically pumped magnetometers: A more adaptable and less expensive alternative? Prenat Diagn. **37**, 193 (2017).
[11] S. Lew, M. S. Hämäläinen, and Y. Okada, Toward noninvasive monitoring of ongoing electrical activity of human uterus and fetal heart and brain, Clin. Neurophysiol. **128**, 2470 (2017).
[12] S. Strand, W. Lutter, J. F. Strasburger, V.k. Shah, O. Baffa, and R. T. Wakai, Low-cost fetal magnetocardiography: A comparison of superconducting quantum interference device and optically pumped magnetometers, J. Am. Heart. Assoc. **8**, 16 (2019).
[13] L. Liu, *et al.*, In-orbit operation of an atomic clock based on laser-cooled ^{87}Rb atoms, Nat. Commun. **9**, 16 (2018).
[14] T. E. Chupp, P. Fierlinger, M. J. Ramsey-Musolf, and J. T. Singh, Electric dipole moments of atoms, molecules, nuclei, and particles, Rev. Mod. Phys. **91**, 015001 (2019).
[15] I. Altarev, *et al.*, A magnetically shielded room with ultra low residual field and gradient, Rev. Sci. Instrum. **85**, 075106 (2014).
[16] J. Li, W. Quan, B. Han, Z. Wang, and J. Fang, Design and optimization of multilayer cylindrical magnetic shield for SERF atomic magnetometer application, IEEE Sens. J. **20**, 1793 (2020).
[17] J. Li, Z. Wang, and W. Quan, Multi-objective optimization of multilayer passive magnetic shield based on genetic algorithm, AIP Adv. **9**, 125210 (2019).
[18] S. Celozzi, R. Araneo, and G. Lovat, *Appendix B: Magnetic Shielding* (John Wiley & Sons Ltd, New York, 2008).
[19] S. Pissanetzky, Minimum energy MRI gradient coils of general geometry, Meas. Sci. Technol. **3**, 7 (1992).
[20] M. Poole and R. Bowtell, Novel gradient coils designed using a boundary element method, Concept Magn. Reson. B **3**, 162 (2007).
[21] R. Zettera, A. J. Mäkinen, J. Iivanainen, K. C. J. Zevenhoven, R. J. Ilmoniemi, and L. Parkkonen, Magnetic field modeling with surface currents. Part II. Implementation and usage of bfieldtools, J. Appl. Phys. **128**, 063905 (2020).
[22] A. J. Mäkinen, R. Zetter, J. Iivanainen, K. C. J. Zevenhoven, L. Parkkonen, and R. J. Ilmoniemi, Magnetic field modeling with surface currents. Part I. Implementation and usage of bfieldtools, J. Appl. Phys. **128**, 063906 (2020).
[23] C.-Y. Liu, T. Andalib, D. C. M. Ostapchuk, and C. P. Bidinosti, Analytic models of magnetically enclosed spherical and solenoidal coils, Nucl. Instrum. Methods Phys. Res. **949**, 162837 (2020).
[24] R. Lambert and C. Uphoff, Magnetically shielded solenoid with field of high homogeneity, Rev. Sci. Instrum. **46**, 3 (1975).
[25] R. J. Hanson and F. M. Pipkin, Magnetically shielded solenoid with field of high homogeneity, Rev. Sci. Instrum. **36**, 2 (1965).
[26] J. D. Jackson, *Classical Electrodynamics* (Wiley, New York, 1998), 3rd ed.
[27] A. Kordyuk, Magnetic levitation for hard superconductors, J. Appl. Phys. **83**, 610 (1985).
[28] Q. Cao, D. Pan, J. Li, Y. Jin, Z. Sun, S. Lin, G. Yang, and L. Li, Optimization of a coil system for generating uniform magnetic fields inside a cubic magnetic shield, Energies **11**, 3 (2018).
[29] T. Liu, J. Voigt, Z. Sun, A. Schnabel, K. Grueneberg, I. Fan, and L. Li, in *Conference on Precision Electromagnetic Measurements* (2018), p. 1.
[30] T. Liu, A. Schnabel, Z. Sun, J. Voigt, and L. Li, Approximate expressions for the magnetic field created by circular coils inside a closed cylindrical shield of finite thickness and permeability, J. Magn. Magn. Mater. **507**, 166846 (2020).
[31] N. Holmes, T. M. Tierney, J. Leggett, E. Boto, S. Mellor, G. Roberts, R. M. Hill, V. Shah, G. R. Barnes, M. J. Brookes, and R. Bowtell, Balanced, bi-planar magnetic field and field gradient coils for field compensation in wearable magnetoencephalography, Sci. Rep. **9**, 14196 (2019).
[32] R. Turner and R. M. Bowley, Passive screening of switched magnetic field gradients, J. Phys. E Sci. Instrum. **19**, 876 (1986).
[33] M. Packer, P. J. Hobson, N. Holmes, J. Leggett, P. Glover, M. J. Brookes, R. Bowtell, and T. M. Fromhold, Optimal Inverse Design of Magnetic Field Profiles in a Magnetically Shielded Cylinder, Phys. Rev. Appl. **14**, 054004 (2020).
[34] P. Hammond, Electric and magnetic images, Proc. IEE Part C Monogr. **107**, 306 (1960).
[35] W. A. Roshen, Effect of finite thickness of magnetic substrate on planar inductors, IEEE Trans. Magn. **26**, 270 (1990).
[36] J. Kennedy and R. Eberhart, in *Proceedings of ICNN'95—International Conference on Neural Networks* (1995), Vol. 4, p. 1942.

[37] F. Roméo and D. I. Hoult, Magnet field profiling: Analysis and correcting coil design, Magn. Reson. Med. **1**, 1 (1984).
[38] http://doi.org/10.5281/zenodo.4442661.
[39] J. R. Corea, A. M. Flynn, B. Lechene, G. Scott, G. D. Reed, P. J. Shin, M. Lustig, and A. C. Ariasb, Screen-printed flexible MRI receive coils, Nat. Commun. **7**, 10839 (2016).
[40] T. D. Ngo, A. Kashani, G. Imbalzano, K. T. Q. Nguyen, and D. Hui, Additive manufacturing (3D printing): A review of materials, methods, applications and challenges, Compos. B Eng. **143**, 172 (2018).
[41] I. S. Gradshteyn and I. M. Ryzhik, *Table of Integrals, Series, and Products* Vol. 7 (Academic Press, Amsterdam, 2007), p. 1

Chapter 5

Magnetic Field design in a Cylindrical High Permeability Shield: The Combination of Simple Building Blocks and a Genetic Algorithm

Magnetic Field design in a Cylindrical High Permeability Shield: The Combination of Simple Building Blocks and a Genetic Algorithm

M. Packer[1], P. J. Hobson[1], A. Davis[1], N. Holmes[1,2], J. Leggett[1,2],
P. Glover[1,2], M. J. Brookes[1,2], R. Bowtell[1,2], and T. M. Fromhold[1]
[1]*School of Physics and Astronomy, University of Nottingham, Nottingham, NG7 2RD, UK.*
[2]*Sir Peter Mansfield Imaging Centre, School of Physics and Astronomy,*
University of Nottingham, Nottingham, NG7 2RD, UK.
(Dated: July 8, 2021)

Magnetically-sensitive experiments and newly-developed quantum technologies with integrated high-permeability magnetic shields require increasing control of their magnetic field environment and reductions in size, weight, power and cost. However, magnetic fields generated by active components are distorted by high-permeability magnetic shielding, particularly when they are close to the shield's surface. Here, we present an efficient design methodology for creating target static magnetic field profiles by using discrete coils electromagnetically-coupled to a cylindrical passive magnetic shield. We utilize a modified Green's function solution that accounts for the interior boundary conditions on a closed finite-length high-permeability cylindrical magnetic shield, and determine simplified expressions when a cylindrical coil approaches the interior surface of the shield. We use simple discrete building blocks to provide a complete discrete coil basis to generate any physically-attainable magnetic field in free space. We then use a genetic algorithm to find optimized discrete coil structures composed of this basis. We use our methodology to generate an improved linear axial gradient field, $\mathrm{d}B_z/\mathrm{d}z$, and transverse bias field, B_x. These optimized structures increase, by a factor of seven and three compared to the standard configurations, the volume in which the target and achieved fields agree within 1% accuracy, respectively. This coil design method can be used to optimize active–passive magnetic field shaping systems that are compact and simple to manufacture, enabling accurate magnetic field control in spatially-confined experiments at low cost.

I. INTRODUCTION

The mathematical framework for magnetic field design was first formalized by Romeo and Hoult, who used discrete loops and arcs as the building blocks of a coil basis to generate accurate fields for MRI shimming coils [1]. These magnetic field profiles produced by these simple coil building blocks were expanded in a spherical harmonic basis and the harmonic fields related to the geometry, position, and current of the coil basis elements. The geometries were selected, and their positions adjusted, to minimize unwanted signals and, therefore, maximize the fidelity of a desired magnetic field profile. It was subsequently found that inverse methods based on a continuum representation of the current density could allow the design of higher-fidelity magnetic fields, albeit with more computational effort. Pissanetzky first formulated arbitrary current densities on triangular boundary elements [2], allowing optimal designs to be found through an entirely numerical method. This formulation was later improved upon by Poole [3], enabling the flexible design of MRI gradient coils on surfaces of arbitrary geometry using sophisticated 3D-contouring methods. Pseudo-analytical techniques have also been developed on specific surface geometries using Green's function expansions and quadratic optimization methods that enable the rapid design of accurate user-specified magnetic fields in free space [4–7].

Newly-developed quantum technologies with greater performance and reduced size have further increased the demand for state-of-the-art magnetically-controlled environments. These technologies include: quantum sensing of gravity for geological survey [8–11], atomic clocks for precision timing [12, 13], and atomic magnetometry [14–16] for material characterization [17] and biomedical imaging [18–24]. Magnetic field control is required in many of these devices to trap and manipulate atoms. To translate these laboratory experiments to usable devices in real-world settings, high-permeability passive magnetic shields are used to attenuate stray magnetic fields caused by nearby electronic equipment and/or the local Earth's magnetic field. Specifically, cylindrical and cubic magnetic shields are often used in these systems as they are simple to manufacture, provide good shielding, and can accommodate equipment easily inside them [25–27]. However, previous longstanding methods of magnetic field design do not incorporate the interaction of active current-carrying coils with the high-permeability passive shielding materials. Consequently, if these methods are used to design coils to generate specific magnetic fields in shielded environments, the magnetic shield will distort the field profile, prohibiting the desired level of field control [28].

Motivated by this problem, several novel numerical and analytical methods have recently been developed that incorporate high-permeability passive shielding material into their design methodologies. The numerical methods use an equipotential scalar field to enforce the boundary condition on the shield's surface, and then account for this in the

design of surface currents using boundary elements on arbitrary geometries inside the shield [29, 30]. The analytical methods rely on modifying the Green's function to satisfy the boundary condition on the shield's surface. The currents are then decomposed into an orthogonal basis set where the magnetic fields generated by the combined system can be calculated [31, 32]. These methods can design complex current distributions that generate extremely accurate magnetic fields inside shielded environments. However, to realize these high fidelity fields physically, the designs must be carefully discretized and accurately represented in real systems. In many of these systems, magnetic field control is not the only area of concern. Optical access, miniaturization, and cost also constrain the development of many of these technologies. Consequently, field design methods in shielded environments must accommodate these additional constraints. In this context, using optimally-placed discrete coil designs could allow for simplistic, cost-effective, and accurate generation of magnetic fields with greater optical access at a much lower cost. Some simple discrete coil geometries have been formulated that allow the design optimization of magnetic field-generating systems in shielded environments. However, these are restricted to circular loops and simple transverse fields [33–36]. Currently, no generalized discrete coil optimization method exists that incorporates the interaction with high-permeability shielding; partly due to the multitude of free parameters associated with discrete coils and their complex electromagnetic interaction with an exterior magnetic shield.

Alongside this, multi-objective optimization procedures, such as genetic algorithms, particle swarm optimizations, and differential evolution algorithms, have garnered considerable attention over the past decade because of their ability to find optimal solutions to complicated problems with mixed constraints [37, 38]. Advances in computational power and code accessibility have made these algorithms much easier to implement [39]. In this paper, using the analytical formulation of cylindrical coils in a cylindrical magnetic shield [31], the framework of Romeo and Hoult [1], and a genetic algorithm optimization procedure [40], we present a widely-applicable design methodology that enables the construction of optimized discrete coils in cylindrical magnetic shields. Firstly, we expand on the analytical formulation by determining an approximate form of the magnetic field when the coil is close to the surface of the magnetic shield. Secondly, we formulate a complete coil basis in cylindrical coordinates that allows the simple construction of harmonic fields using discrete coils. Finally, we find optimal configurations of multiple nested sets of the discrete coil basis to generate specified harmonic fields utilizing a genetic algorithm. By incorporating these different elements, our method enables the simple design of specified magnetic field profiles in high-permeability cylindrical magnetic shields constrained by optical access, cost, and size, thereby enabling the miniaturization and commercialization of technologies that require precisely-controlled magnetic field environments.

II. MODEL

Let us consider a region of air completely enclosed by a magnetic shield with a magnetic field incident on the shield. As a direct result of Ampere's law and Gauss's law for magnetism, the tangential and normal components of the magnetic field strength, $\mathbf{H}$, and flux density, $\mathbf{B}$, respectively, must be continuous across a surface interface, S. Working in the magnetostatic regime, where no current exists on the surface of the magnetic shield, these boundary conditions take the form

$$\left(\frac{1}{\mu_r}\mathbf{B}_{\text{mat.}} - \mathbf{B}_{\text{air}}\right) \wedge \hat{\mathbf{n}} = 0 \qquad \text{on } S, \tag{1}$$

and

$$(\mathbf{B}_{\text{mat.}} - \mathbf{B}_{\text{air}}) \cdot \hat{\mathbf{n}} = 0 \qquad \text{on } S, \tag{2}$$

where $\hat{\mathbf{n}}$ is the unit vector normal to S and μ_r is the relative permeability of the shielding material. At the surface of materials with very high permeability, the condition (1) dictates that the parallel component of the flux density in air near the surface is approximately zero. Thus, the field in air is directed almost entirely perpendicular to the material surface. Within the material, however, from (2), the perpendicular component of the field strength is reduced by a factor of μ_r and the field therefore runs almost parallel to the surface. This mechanism diverts external flux away from the interior shielded region and is also responsible for the deviations introduced when using standard field design methods in shielded environments.

The permeability of standard high-permeability magnetic shields has been shown experimentally to be in excess of 100000 once properly treated [41]. Consequently, for these materials, the boundary conditions can be approximated as

$$\mathbf{B}(\mathbf{r})_{\parallel} \approx 0 \quad \text{on } S. \tag{3}$$

Here, we consider a closed high-permeability cylinder of inner radius ρ_s and length L_s, with planar end caps located at $z = \pm L_s/2$. Inside this cylindrical shield a current, $\mathbf{J}$, flows on a co-axially nested cylindrical surface of radius ρ_c, thickness $2\rho_w$, and length L_s, as shown in Fig. 1, such that $\rho_c + \rho_w \leq \rho_s$. In the high-permeability regime, the boundary conditions at the shield's surface can be approximated as

$$B_\rho\Big|_{z=\pm L_s/2} = 0, \quad B_\phi\Big|_{z=\pm L_s/2, \rho=\rho_s} = 0, \quad B_z\Big|_{\rho=\rho_s} = 0. \tag{4}$$

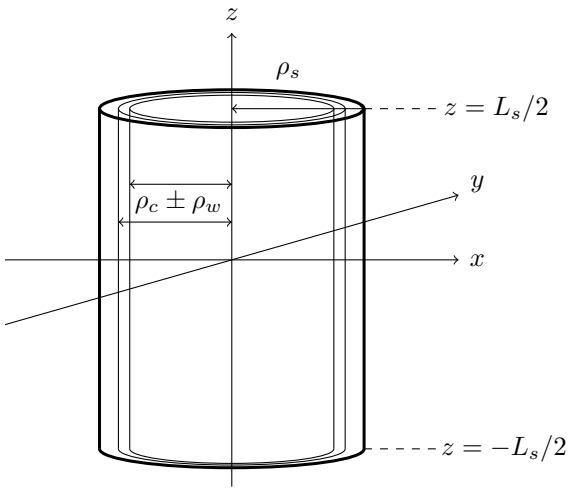


FIG. 1: Cylindrical magnetic shield with high permeability, $\mu_r \gg 1$, of length L_s and inner radius ρ_s with planar end caps located at $z = \pm L_s/2$. A coil of radius ρ_c and equal length to the shield is placed symmetrically inside the shield, and the coils are formed of wire of radius ρ_w.

The magnetic field in free space can be calculated using the magnetic field strength generated by a current source and the magnetization, $\mathbf{M}$, induced within the shield,

$$\mathbf{B} = \mu_0(\mathbf{H} + \mathbf{M}). \tag{5}$$

The magnetization can be represented as a mathematically-equivalent surface pseudo-current, $\boldsymbol{\nabla} \wedge \mathbf{M} = \widetilde{\mathbf{J}}$, which can then be related to the vector potential, $\mathbf{B} = \boldsymbol{\nabla} \wedge \mathbf{A}$, to generate the Poisson equation,

$$\nabla^2 \mathbf{A} = -\mu_0(\mathbf{J} + \widetilde{\mathbf{J}}). \tag{6}$$

In previous works [31, 32], a Green's function solution for Poisson's equation, (6), is formulated using a surface pseudo-current to satisfy the boundary condition, (4), over the interior surface of the magnetic shield. The radial boundary condition is satisfied by equating the magnetic field generated by an arbitrary cylindrical current and pseudo-current on the surface of a shield of infinite length at $\rho = \rho_s$. The boundary conditions on the end caps can then be satisfied by using the method of mirror images [42] to generate images of the current and pseudo-current. Due to the orthogonality of the planar end caps, the reflected image currents continue to satisfy the radial boundary condition, therefore satisfying the boundary condition over the entire domain of the magnetic shield. The total field, in a region within the cylinder $\rho < \rho_c$, is then given by [31]

$$B_\rho(\rho, \phi, z) = \frac{i\mu_0\rho_c}{2\pi} \sum_{m=-\infty}^{\infty} \sum_{p=-\infty}^{\infty} \int_{-\infty}^{\infty} \mathrm{d}k \; k e^{im\phi} e^{ikz} I'_m(|k|\rho) R_m(k, \rho_c, \rho_s) J_\phi^{mp}(k), \tag{7}$$

$$B_\phi(\rho, \phi, z) = -\frac{\mu_0\rho_c}{2\pi\rho} \sum_{m=-\infty}^{\infty} \sum_{p=-\infty}^{\infty} \int_{-\infty}^{\infty} \mathrm{d}k \; m\frac{|k|}{k} e^{im\phi} e^{ikz} I_m(|k|\rho) R_m(k, \rho_c, \rho_s) J_\phi^{mp}(k), \tag{8}$$

$$B_z(\rho,\phi,z) = -\frac{\mu_0\rho_c}{2\pi}\sum_{m=-\infty}^{\infty}\sum_{p=-\infty}^{\infty}\int_{-\infty}^{\infty}\mathrm{d}k\ |k|e^{im\phi}e^{ikz}I_m(|k|\rho)R_m(k,\rho_c,\rho_s)J_\phi^{mp}(k), \tag{9}$$

where $R_m(k,\rho_c,\rho_s) = K_m'(|k|\rho_c) - I_m'(|k|\rho_c)K_m(|k|\rho_s)/I_m(|k|\rho_s)$, and $J_\phi^{mp}(k)$ is the Fourier transform with respect to z and ϕ of the p^{th} reflected image current determined via the method of mirror images, where the $p=0$ term represents the Fourier transform of the actual current distribution which is confined to the region $|z'| < L_s/2$

$$J_\phi^{mp}(k) = \frac{1}{2\pi}\int_0^{2\pi}\mathrm{d}\phi'\ e^{-im\phi'}\int_{-\infty}^{\infty}\mathrm{d}z'\ e^{-ikz'}J_\phi\left(\phi',(-1)^p\left(z'+pL_s\right)\right), \tag{10}$$

where (ϕ',z') specify position on the current-carrying surface.

Previously, this formulation has been used to design coils through a harmonic minimization method with a continuum representation of the current. The optimal continuum solution can be found using a quadratic programming algorithm wherein the continuum solution is discretized into a physical wire pattern that approximates the continuous current distribution. The errors introduced in this method result either from assuming that the shield is a perfect magnetic conductor, which doesn't saturate, or from inaccurately discretizing the current continuum such that both the coil and, consequently, the magnetic shield introduce erroneous fields. For most real-world applications, the perfect magnetic conductor approximation introduces extremely small errors that are far less significant than the errors introduced in manufacturing. For example, assuming $\mu_r > 20000$ and material thickness $d_s = 1$ mm, the typical deviation from the analytical solution is $< 0.005\%$ [31, 43, 44]. Furthermore, high-grade annealed cylindrical mumetal shields have been experimentally shown to effectively shunt internal fields up to $H = 40$ A/m before complete saturation [41], which is more than enough for the micro-Tesla field applications required for the majority of shielded experiments. Therefore, in many systems, the dominant error is generated by discretization of the current continuum, which is hard to quantify *a priori* as it is design dependent. The discretization error can only be alleviated by better representing the current continuum with a higher wire density. Although technologies like flex-PCBs [45] and 3D-printers [46] offer the capability to represent the continuum very accurately, such coils are expensive, time-consuming to manufacture, and hard to repair if there is a breakage. Moreover, the required wire positions and high wire density may block experimental access to the interior of the shield, for example blocking easy optical access. Thus, it follows that applying a formulation to design fields using simple discrete coils that are robust and easy to manufacture will benefit numerous systems with design challenges.

To maximize the available interior volume of the system, as often required for real-world applications, we consider discrete coils that are positioned at the shield's inner surface, $\rho_c = \rho_s - \rho_w$, and determine their parameters using forward numerical optimization techniques, thereby circumventing discretization error entirely. When the coil is pressed against the inner surface of the shield, we can expand the magnetic field as a power series of the (small) wire radius such that

$$\mathbf{B}(\rho,\phi,z) = \mathbf{B}^0(\rho,\phi,z) + \rho_w\mathbf{B}^1(\rho,\phi,z) + \rho_w^2\mathbf{B}^2(\rho,\phi,z) + \ldots, \tag{11}$$

where the $\mathbf{B}^\nu$ terms are ν^{th} order field perturbations for $\nu \in \mathbb{Z}^{0+}$. If the radius of wire is sufficiently small compared to the radius of the magnetic shield, the magnetic field can be approximated while only introducing small deviations. Here, we give the example of a simple loop placed at the center of a shield with aspect ratio $L_s/(2\rho_s) = 1$ and wire radii $\rho_w < 0.01\rho_s$. The error between the zeroth-order term and the complete solution is less than 0.06% at the center, as shown by Fig. 2, but, moving away from the origin, this error increases dramatically. This increase is due to a zero in the axial field caused by the magnetic shield's interaction, disproportionately skewing the error. Discounting this region, the error within a radial position $\rho < 0.8\rho_s$ is less than 0.5%. Henceforth, in this paper, we assume that $\rho_w < 0.01\rho_s$ and use only the zeroth-order term to design coils in this regime. The magnetic field components are then approximated, through the use of the Wronskian, resulting in the governing equations

$$B_\rho(\rho,\phi,z) = -\frac{i\mu_0}{2\pi}\sum_{m=-\infty}^{\infty}\sum_{p=-\infty}^{\infty}\int_{-\infty}^{\infty}\mathrm{d}k\ \frac{k}{|k|}e^{im\phi}e^{ikz}\frac{I_m'(|k|\rho)}{I_m(|k|\rho_s)}J_\phi^{mp}(k), \tag{12}$$

$$B_\phi(\rho,\phi,z) = \frac{\mu_0}{2\pi\rho}\sum_{m=-\infty}^{\infty}\sum_{p=-\infty}^{\infty}\int_{-\infty}^{\infty}\mathrm{d}k\ \frac{m}{k}e^{im\phi}e^{ikz}\frac{I_m(|k|\rho)}{I_m(|k|\rho_s)}J_\phi^{mp}(k), \tag{13}$$

$$B_z(\rho,\phi,z) = \frac{\mu_0}{2\pi}\sum_{m=-\infty}^{\infty}\sum_{p=-\infty}^{\infty}\int_{-\infty}^{\infty} \mathrm{d}k\; e^{im\phi}e^{ikz}\frac{I_m(|k|\rho)}{I_m(|k|\rho_s)}J_\phi^{mp}(k). \tag{14}$$

For a set-up where the $\rho_w > 0.01\rho_s$, the validity of the approximation should be determined for each individual scenario and adjusted appropriately for a given field design tolerance and experimental system.

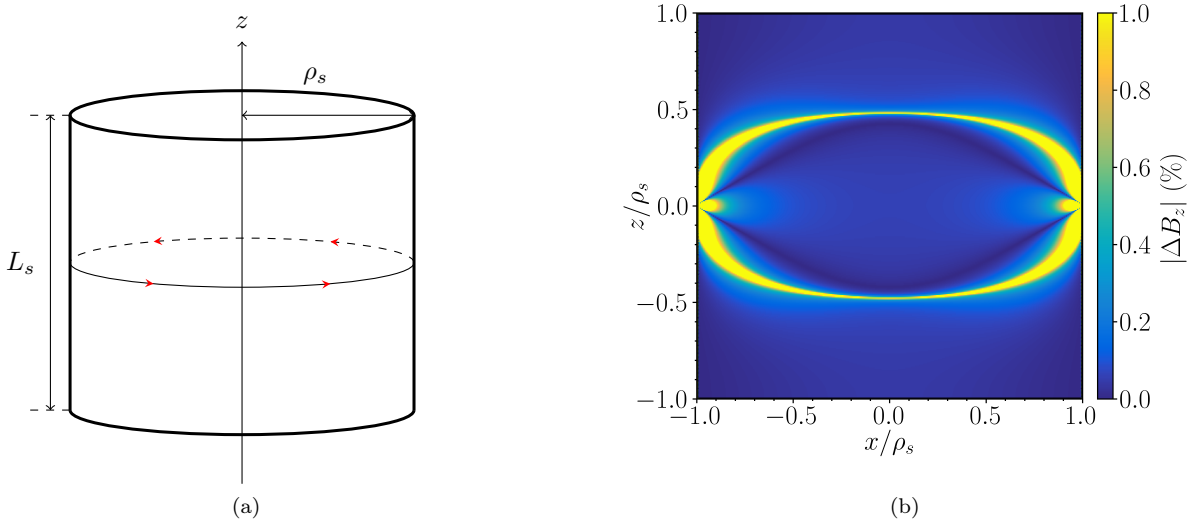


FIG. 2: (a) Schematic diagram of a loop of radius ρ_s at position $z = 0$ in a closed magnetic shield of radius ρ_s and length $L_s = 2\rho_s$. (b) Color map showing the absolute error, $|\Delta B_z|$, between the axial zeroth-order contribution in (14) and the exact solution in (9) for the example depicted in (a).

III. COIL BASIS

To here Decomposing the magnetic field into a complete set of orthogonal eigenfunctions, with associated eigenvalue magnitudes, allows the desired field profile to be selected while minimizing erroneous contributions.

In free space, the magnetic field can be represented as the gradient of a scalar potential, $\mathbf{B} = -\nabla\Psi$. The scalar potential and magnetic field, (5), both satisfy Laplace's equation and can be represented as a sum of orthogonal functions in an orthogonal curvilinear coordinate system. In this work, following Romeo and Hoult [1], we represent the scalar potential as the set of real spherical harmonics in spherical polar coordinates, and, therefore, the magnetic field by

$$\mathbf{B}(r,\theta,\phi) = \boldsymbol{\nabla}\sum_{n=0}^{\infty}\sum_{m=-n}^{n} C_{n,m}r^n P_{n|m|}(\cos\theta)\begin{pmatrix}\cos(|m|\phi)\\ \sin(|m|\phi)\end{pmatrix}, \quad \begin{matrix} m\geq 0\\ m<0\end{matrix} \tag{15}$$

where the harmonic fields are classified through their order, n, and degree, m. Each harmonic has a magnitude, $C_{n,m}$, and shows a variation with respect to θ that is described by one of the Ferrer's associated Legendre polynomials, $P_{n|m|}(\cos\theta)$. The harmonics are mutually orthogonal on the surface of a sphere, with high-order n and m harmonics representing higher frequency variations in the field along the zenith and azimuthal, respectively. Due to their relation with the associated Legendre polynomials, the axial symmetry of the spherical harmonics depends on the parity of $(n + m)$. The degree is then divided into two cases, $m = 0$ and $|m| > 0$. The $m = 0$ harmonic fields exhibit total azimuthal symmetry and are known as zonal harmonics, Z_n. The $|m| > 0$ harmonic fields exhibit m-fold azimuthal symmetry and are known as tesseral harmonics, $T_{n,m}$, where negative $m < 0$ harmonic fields are $\pi/2m$ azimuthal rotations of their positive $m > 0$ counterparts. Using this basis any magnetic field in free space can be simply decomposed into the combination of axially odd and even, zonal and tesseral harmonic fields.

Due to the link between the magnetic field and the scalar potential, every vector component of the magnetic field

must depend on a single scalar function. However, some scalar fields are not present in every vector component of the magnetic field. This is most clearly seen though the spherical harmonic decomposition of the axial magnetic field

$$B_z(r,\theta,\phi) = \sum_{n=1}^{\infty}\sum_{m=-n+1}^{n-1} C_{n,m}(n+m)r^{n-1}P_{n-1,|m|}\left(\cos\theta\right)\begin{pmatrix}\cos\left(|m|\phi\right) & m\geq 0\\ \sin\left(|m|\phi\right) & m<0\end{pmatrix}, \tag{16}$$

as derived in Appendix A. Again, due to the associated Legendre polynomials, the axial parity of the axial field is odd, if $(n+m-1)=2\nu+1$, and even, if $(n+m-1)=2\nu$, respectively, for $\nu\in\mathbb{Z}^{0+}$. Here, no axial field exists where $m=n$. Although the complete set of harmonic fields do not exist within the axial field, any harmonic can be indirectly selected using it. This requires the correct current density basis to be chosen such that the harmonics that are not present in the axial field can be removed independently. Here, we consider the appropriate cylindrical basis for discrete currents placed symmetrically inside a cylindrical magnetic shield to efficiently construct the complete set of harmonic fields using only the axial field. It should be noted that this could be performed with any vector component of the magnetic field. However, using any other component it is more complicated [1].

As the axial magnetic field (9) is directly related to the Fourier transform of the azimuthal current density, the axial parity and azimuthal symmetry in the magnetic field must mirror those in the azimuthal current density. As the current density can be written as a product of two terms - one varying with z and one varying with ϕ, their variations can be decoupled to independently maximize harmonics of a specific n and m, respectively. To generate zonal harmonics this requires closed circular loops with complete azimuthal symmetry. To maximize the strength of a specific tesseral harmonic, an arc with the same azimuthal periodicity as the desired harmonic is needed. Then, to match the axial parity of a desired harmonic field, pairs of axially separated axially symmetric and anti-symmetric, loops and arcs are used. These combinations of zonal and tesseral, symmetric and anti-symmetric pairs constitute the coil basis that will be used to construct any arbitrary harmonic field, and, therefore, any physical magnetic field in free space. Additionally, because arcs are not continuous, they must be connected with axial connections, forming saddle-like systems [47]. These axial wires contribute to off axis field components, but, due to the formulation of the magnetic field, these variations are accounted for and encoded within the azimuthal Fourier transform. Symmetric arc pairs, therefore, require twice the number of axially separated arcs to satisfy the continuity of current. Hence, these systems must be composed of double saddle Golay-type coils [48].

For simplicity, we formulate these building blocks centered about the origin, maintaining parity symmetry within the magnetic shield. It must be noted, however, that a formulation can be performed with asymmetric placement, albeit with the added complication of both axially odd and even parity harmonics being present simultaneously.

Let us decompose the current density into axial and azimuthal components

$$J_\phi(\phi',z') = I\Phi(\phi')Z(z'), \tag{17}$$

where I is the current in the wire. The axial variation of a symmetric or anti-symmetric pair separated by an axial distance $2d$, is given by

$$Z^{\pm}(z') = \delta(z'-d)\pm\delta(z'+d), \tag{18}$$

with the resulting p^{th} reflected Fourier transform from (10) written as

$$J_\phi^{mp}(k) = e^{ikpL_s}\left(e^{-(-1)^p ikd}\pm e^{(-1)^p ikd}\right)\Phi^m, \tag{19}$$

where the azimuthal Fourier transform of the azimuthal variation of the current density is

$$\Phi^m = \frac{1}{2\pi}\int_0^{2\pi}\mathrm{d}\phi'\; e^{-im\phi'}\Phi\left(\phi'\right). \tag{20}$$

To maximize a specific degree of harmonic $m=M$, with either complete azimuthal symmetry, $M=0$, or periodicity $\pi/|M|$, the azimuthal component is chosen according to the desired harmonic field, given by

$$\Phi(\phi') = \begin{cases}\sum_{\lambda=0}^{2M-1}(-1)^\lambda\left[H\left(\phi'+\varphi-\frac{\lambda\pi}{M}\right)-H\left(\phi'-\varphi-\frac{\lambda\pi}{M}\right)\right], & M>0\\ 1, & M=0\\ \sum_{\lambda=0}^{2M-1}(-1)^\lambda\left[H\left(\phi'+\varphi-\frac{\lambda\pi}{M}-\frac{\pi}{2M}\right)-H\left(\phi'-\varphi-\frac{\lambda\pi}{M}-\frac{\pi}{2M}\right)\right], & M<0\end{cases} \tag{21}$$

where $H(x)$ is the Heaviside function. These azimuthal variations are illustrated in Fig. 3. The azimuthal Fourier transform, from (20), is then found to be

$$\Phi^m(\varphi) = \begin{cases} \frac{\sin(m\varphi)}{\pi m} \sum_{\lambda=0}^{2M-1} (-1)^\lambda e^{-\frac{im\lambda\pi}{M}}, & M > 0 \\ \delta_{m0}, & M = 0 \\ \frac{\sin(m\varphi)}{\pi m} e^{-\frac{im\pi}{2M}} \sum_{\lambda=0}^{2M-1} (-1)^\lambda e^{-\frac{im\lambda\pi}{M}}. & M < 0 \end{cases} \tag{22}$$

Due to the preserved symmetries within the system, axial symmetric and anti-symmetric coils can only generate odd and even parity harmonics, respectively. From this parity, the symmetry of a specific order of harmonic $n = N$, and, subsequently, axial coil symmetry, can then be chosen to select the required field symmetries within the system. These building blocks, composed of zonal and tesseral, symmetric and anti-symmetric coils, are depicted in Fig. 4.

Using (19), (17) and (14), noticing the expression can be written in terms of a Fourier series, the axial magnetic field generated by symmetric and anti-symmetric pairs is given by

$$B_z^{\pm}(\rho, \phi, z) = \frac{2\mu_0 I}{L_s} \sum_{m=-\infty}^{\infty} b_m^{\pm}(\rho, z; d) e^{im\phi} \Phi^m, \tag{23}$$

respectively, where

$$b_m^{+}(\rho, z; d) = \sum_{p \text{ even}} \cos\left(\frac{\pi p z}{L_s}\right) \cos\left(\frac{\pi p d}{L_s}\right) \frac{I_m\left(\left|\frac{\pi p}{L_s}\right| \rho\right)}{I_m\left(\left|\frac{\pi p}{L_s}\right| \rho_s\right)}, \tag{24}$$

$$b_m^{-}(\rho, z; d) = \sum_{p \text{ odd}} \sin\left(\frac{\pi p z}{L_s}\right) \sin\left(\frac{\pi p d}{L_s}\right) \frac{I_m\left(\left|\frac{\pi p}{L_s}\right| \rho\right)}{I_m\left(\left|\frac{\pi p}{L_s}\right| \rho_s\right)}, \tag{25}$$

are symmetric and anti-symmetric axial magnetic field variations, respectively, of the coil basis. Using this coil basis that generates zonal and tesseral, symmetric and anti-symmetric fields, we may now begin to construct coil structures that select specific harmonic fields.

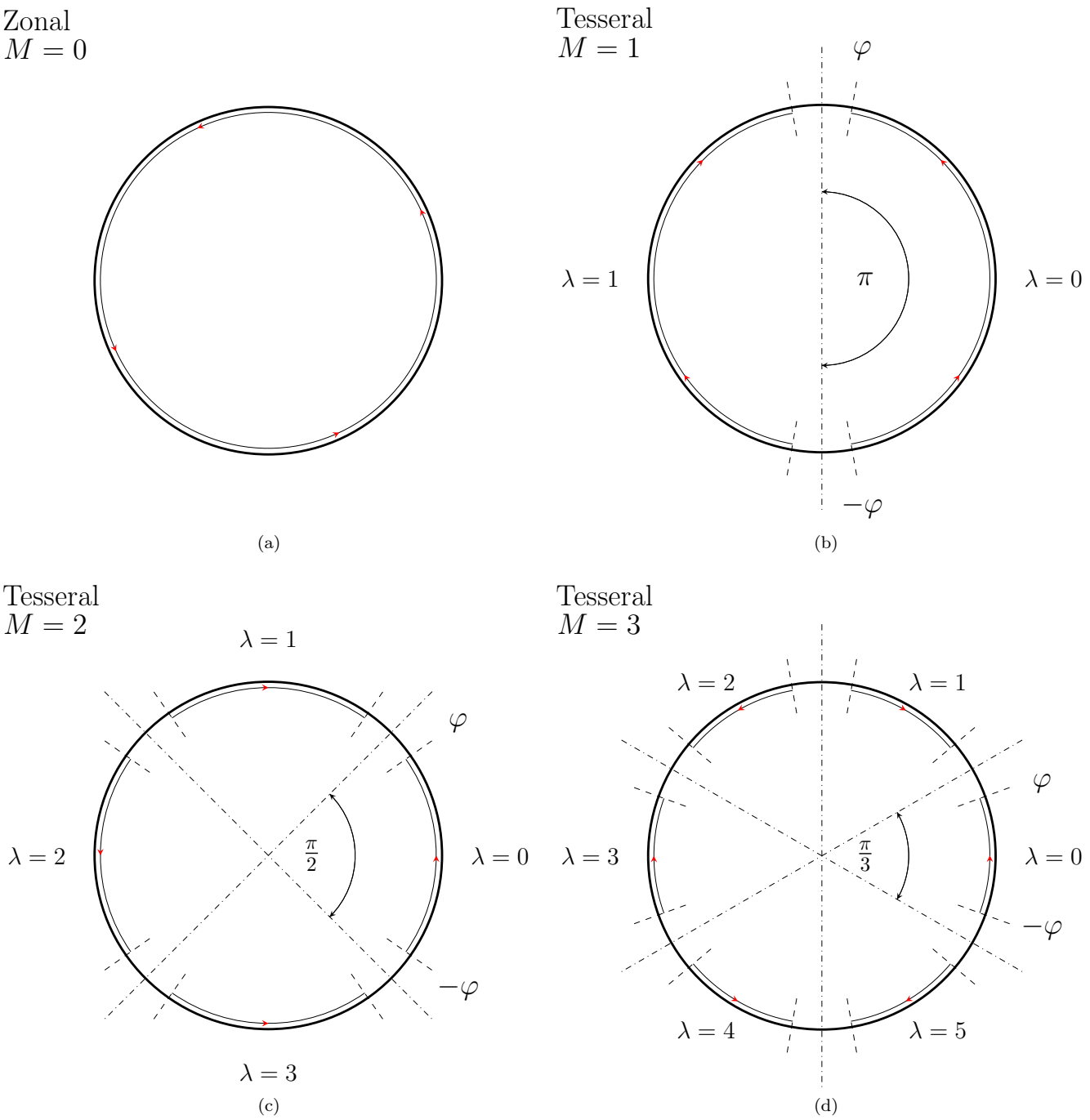


FIG. 3: Azimuthal variation in the basis currents on the $\rho\phi$-plane required by (21) to generate (a) the zonal, $M = 0$, and (b–d) tesseral harmonics of degree one, two, and three, $M = (1 - 3)$, respectively, where the azimutal arc length for each period, λ, is given by 2φ. Red arrows show the direction of current flow.

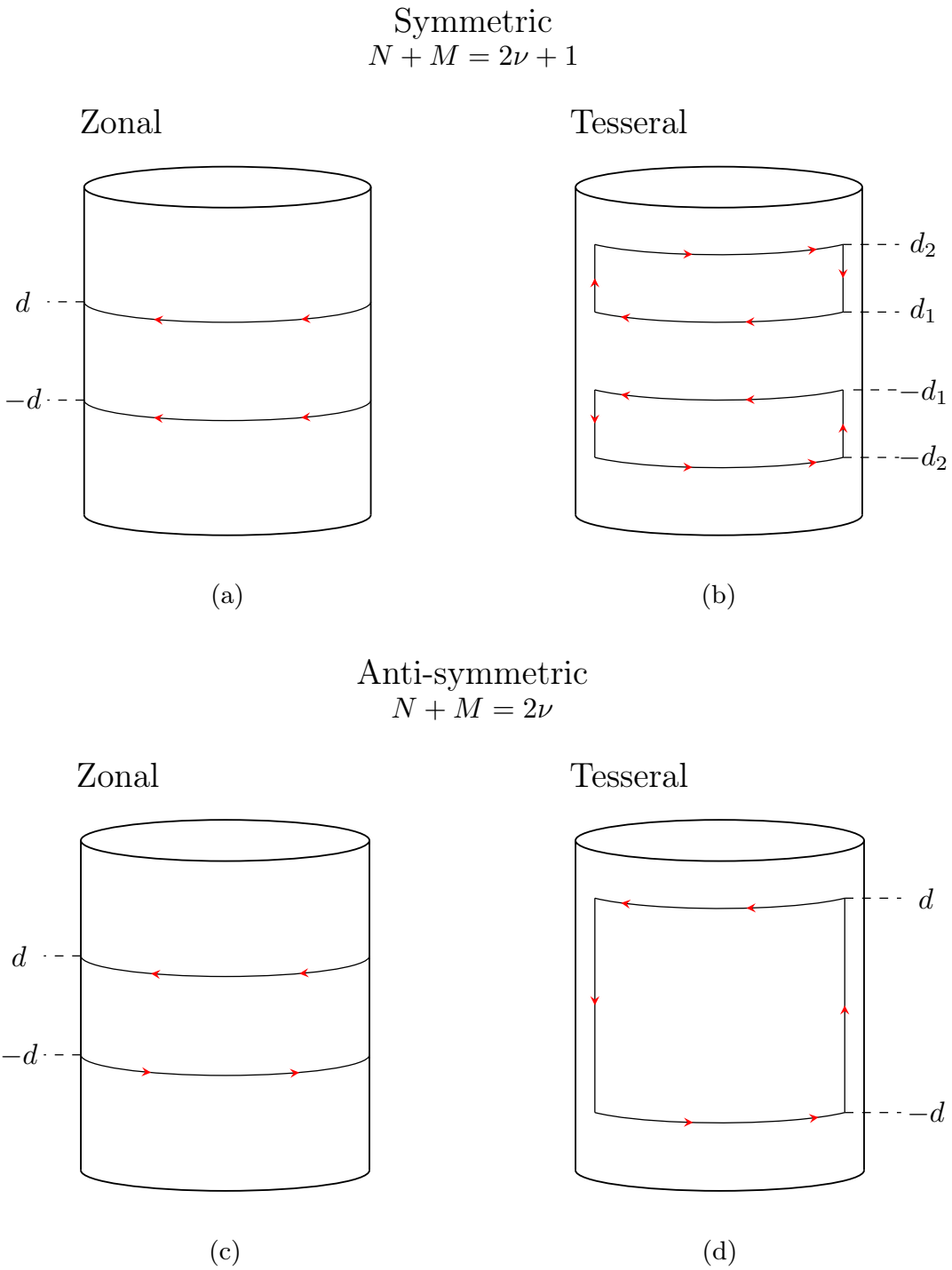


FIG. 4: Azimuthal and axial variation in the basis currents on the ϕz-plane required by (17) to generate (a)-(b) symmetric, $(N + M) = 2\nu + 1$, and (c)-(d) anti-symmetric, $(N + M) = 2\nu$, zonal and tesseral harmonics, respectively, where N and M are the order and degree of the harmonic and $\nu \in \mathrm{Z}^{0+}$. Red arrows show the direction of current flow.

IV. HARMONIC SELECTION

The methodology for designing a coil to generate a specific spherical harmonic variation in any vector direction relies on the azimuthal variation and axial symmetries generated by the coil basis and their connection to the axial magnetic and scalar spherical harmonic fields in free space.

The azimuthal variations and, subsequently, the degrees of harmonics generated, as described in (23), are dictated by the periodicity of a given coil configuration. Thus, to maximize the degree of the desired harmonic we must consider the azimuthal Fourier transform, (22). For $M = 0$, it is apparent that loops only generate fields of degree $m = 0$, and, so, do not require azimuthal optimization. For $|M| > 0$, however, sets of arcs of periodicity $\pi/|M|$ generate an infinite number of harmonic fields of degree $m = (2\nu + 1)M$, where $\nu \in \mathrm{Z}^{0+}$. Therefore, to maximize the desired degree of a tesseral harmonic field, the angular length, φ, should be adjusted to eliminate as many undesired azimuthal variations as possible. From analysis of (22), the leading-order error term of degree $m = 3M$ is removed simply if

$$\sin(3M\varphi) = 0. \tag{26}$$

However, depending on the required accuracy of the desired field, further variations might need to be removed. To achieve this, additional arcs of angular length φ_j and azimuthal turn ratios, I_j^φ, can be used to allow multiple degrees to be minimized simultaneously, as depicted in Fig. 5a. Hence, generalizing (26), we can use M' arcs to simultaneously minimize $\tilde{M}$ degrees of harmonics,

$$\min_{\varphi_j, I_j^\varphi} \left[\sum_{j=1}^{M'} I_j^\varphi \sin((2\nu+1)M\varphi_j) \right], \qquad \nu \in \mathbb{Z} : \nu \in [1, \tilde{M}]. \tag{27}$$

Therefore, using this relation, the harmonics which do not exist within the axial field, $m = n$, can be selected or minimized. In theory, as there are $2M'$ independent free variables, $2M'$ degrees can be removed from the system. For practical applications I_j^φ must be integer ratios of one-another and connected in series, limiting the space in which optimal φ_j can exist. The equations (27) can be solved analytically for integer I_j^φ via substitution of the appropriate Chebyshev polynomials, but it is often quicker to solve them using a numerically exhaustive search technique because of the complexity of the Chebyshev polynomials when compared to the simplicity of (27). Typically, the best solutions have significant angular extents and azimuthal turn ratios within an order of magnitude of each other to prevent the finite size of the wires from introducing deviations. It should also be noted that the value of I_j^φ can be negative, indicating that the j^{th} arc is flowing in the opposite direction. Designs with counter-propagating flows are useful if there are specific regions where wires are prohibited, providing additional flexibility when designing coil setups. They are, however, often very power-inefficient.

The same logic can also be applied to the radial and axial variations within the system to remove harmonics of odd or even parity. First, let us transform the spherical harmonic field (16) into cylindrical coordinates, and separate it into terms of even and odd order,

$$\begin{aligned} B_z = &\left[\sum_{n=0}^{\infty} \sum_{m=-2n}^{2n} C_{2n+1,m}(2n+m+1)(\rho^2+z^2)^n P_{2n,m}\left(\frac{z}{(\rho^2+z^2)^{1/2}}\right) + \right. \\ &\left. \sum_{n=1}^{\infty} \sum_{m=-2n-1}^{2n-1} C_{2n,m}(2n+m)(\rho^2+z^2)^{\frac{n-1}{2}} P_{2n-1,m}\left(\frac{z}{(\rho^2+z^2)^{1/2}}\right) \right] \begin{pmatrix} \cos(|m|\phi) & m \geq 0 \\ \sin(|m|\phi) & m < 0 \end{pmatrix} . \end{aligned} \tag{28}$$

After analyzing (28) and (23), we can see that the radial and axial dependence of every harmonic of order n and degree m, excluding $m \neq n$, must be completely contained within the symmetric and anti-symmetric axial field variations (24)–(25). Therefore, we can write these variations in terms of the harmonic magnitudes

$$b_m^+(\rho, z; d) = \sum_{n=0}^{\infty} \tilde{C}_{2n+1,m}(d, \rho_s, L_s)(\rho^2+z^2)^n P_{2n,m}\left(\frac{z}{(\rho^2+z^2)^{1/2}}\right), \qquad m \leq 2n \tag{29}$$

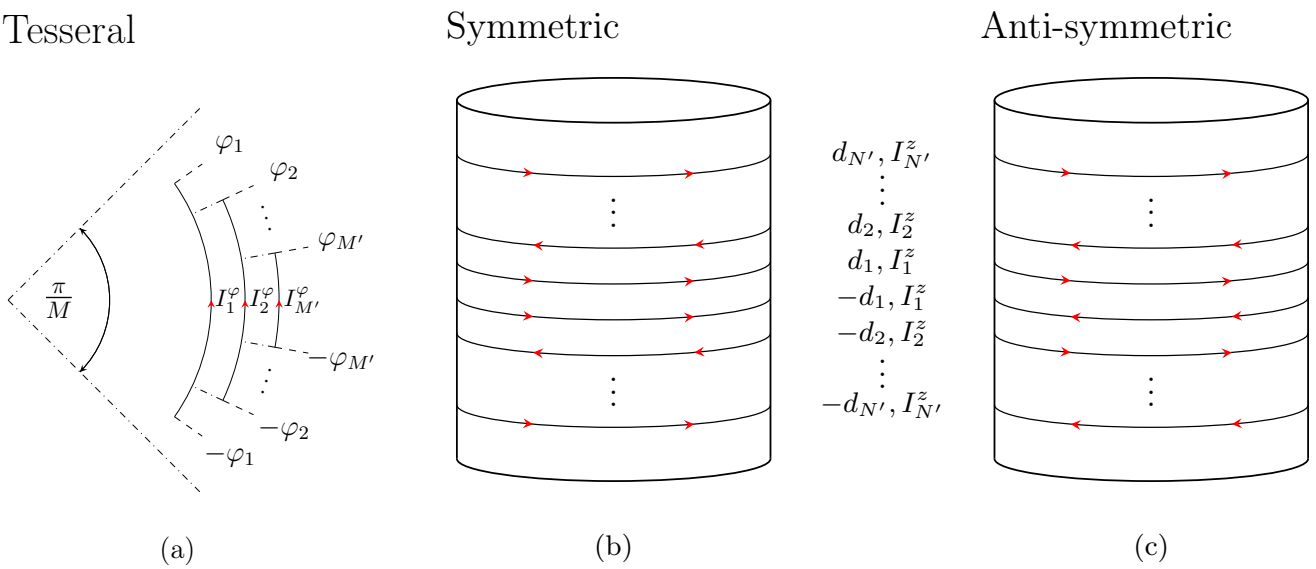


FIG. 5: Sets of the basis currents from (17) to generate more accurate (a) tesseral harmonics of degree M presented on the $\rho\phi$-plane (b)-(c) symmetric and anti-symmetric zonal harmonics, respectively, presented on the ϕz-plane, where N' and M' are the number of basis currents used. Red arrows show the direction of current flow.

$$b_m^-(\rho, z; d) = \sum_{n=1}^{\infty} \tilde{C}_{2n,m}(d, \rho_s, L_s)(\rho^2 + z^2)^{\frac{2n-1}{2}} P_{2n-1\ m}\left(\frac{z}{(\rho^2 + z^2)^{1/2}}\right), \qquad m \leq 2n-1 \tag{30}$$

where $\tilde{C}_{n,m}(d, \rho_s, L_s)$ describes the effective harmonic magnitude that depends on the coil and shield parameters. The relationship between $\tilde{C}_{n,m}(d, \rho_s, L_s)$ and the placement of loops and arcs is apparent when the series expansions of both the trigonometric and Bessel functions are substituted into (24)-(25). The spatial variations can then be separated and grouped into their constituent harmonics then related to the coil parameters. This must be done on a case-by-case basis as only specific sets of harmonics exist within each of the basis coils. Once the harmonics have been separated and effective harmonic magnitudes found in terms of loop or arc positions and shield parameters, the positions can then be found to maximize a desired order of harmonic N. This, again, can be generalized to remove the set of undesired harmonic fields of order $n \in \mathbb{Z} : n \in [n_1', n_N']$ and degree M through the set of simultaneous equations using pairs of symmetric and anti-symmetric loops or arcs at positions d_i with axial turn ratios I_i^z. This is illustrated for zonal symmetric and anti-symmetric loops in Fig. 5b-c. The road map of this harmonic selection process is summarized in Fig. 6.

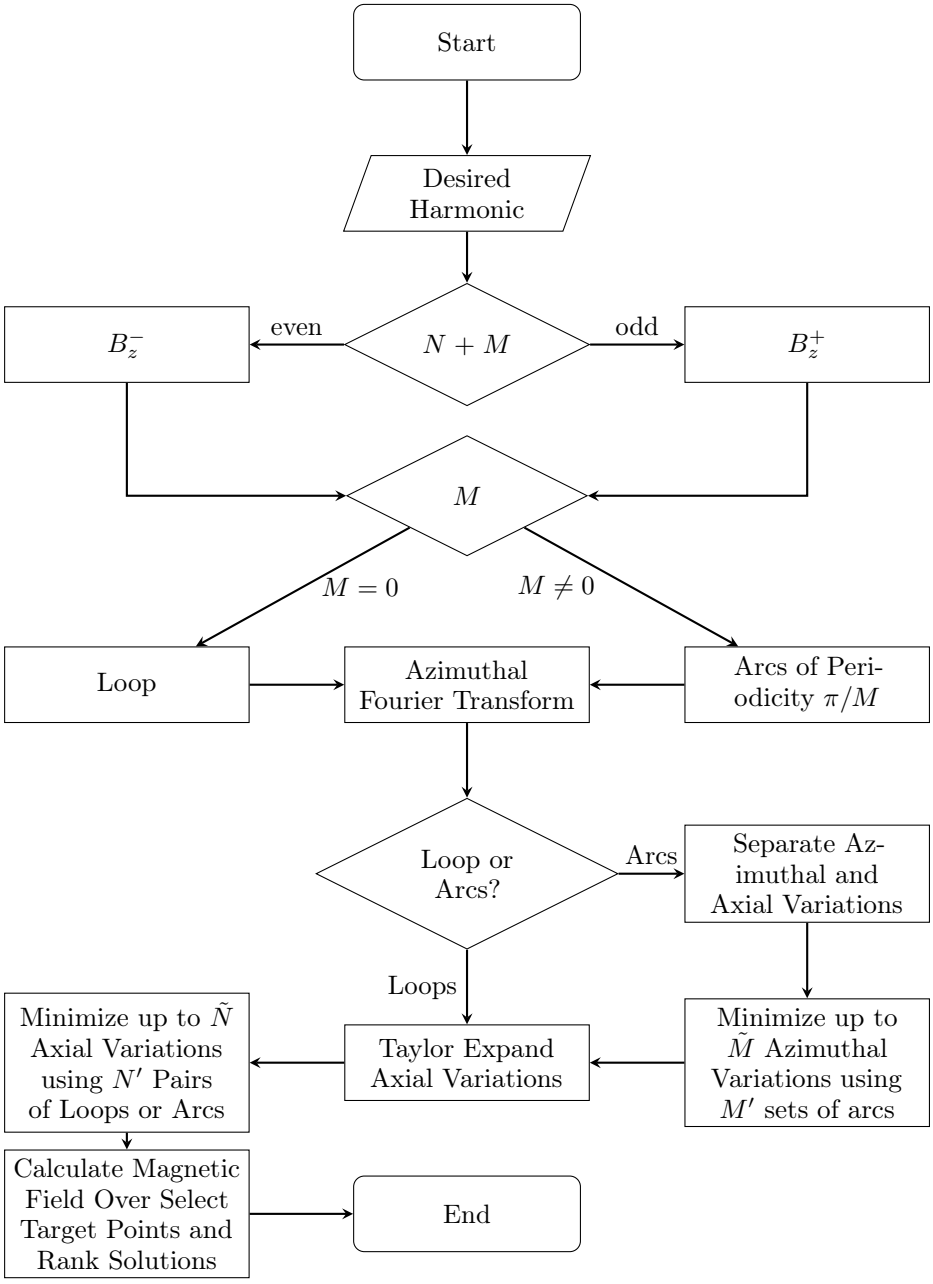


FIG. 6: Flow diagram describing the harmonic minimization method for a target harmonic of order N and degree M using N' axial pairs of loops or arcs with M' arcs at each axial position.

Example: Zonal linear gradient

Let us apply our analytical model to calculate the axial field generated by a pair of loops in the anti-Helmholtz configuration in a shielded environment, depicted in Fig. 7, to demonstrate the effect of the magnetic shield. The anti-Helmholtz configuration uses a pair of anti-symmetric axial loops to generate the scalar harmonic field, Z_2, which produces an axial linear gradient, $\mathrm{d}B_z/\mathrm{d}z$. The optimal loop position in free space, $d = \left(\sqrt{3}/2\right)\rho_c$, can be derived by eliminating the cubic variations in the generated field, i.e. the Z_4 scalar harmonic, through a series expansion of the spatially-varying terms, demonstrated in Appendix B. In Fig. 8a and Fig. 8b we examine the field linearity of an anti-Helmholtz coil in free space and inside a magnetic shield, respectively. The magnetic shield, with shield aspect ratio $L_s/(2\rho_s) = 1$, is chosen as an example similar to standard commercially available magnetic shields [49] to demonstrate the impact of non-optimized designs in real-world systems. The presence of the magnetic shield effects the inductance, gradient, and linearity of the design. The inductance and gradient are both increased by approximately a factor of two. However, large deviations are introduced into the field due to the non-zero cubic variations reducing the central volume of 1% accuracy to the desired gradient by approximately a factor of three. Evidently, new optimal separations must be determined to improve the accuracy of magnetic fields in shielded environments.

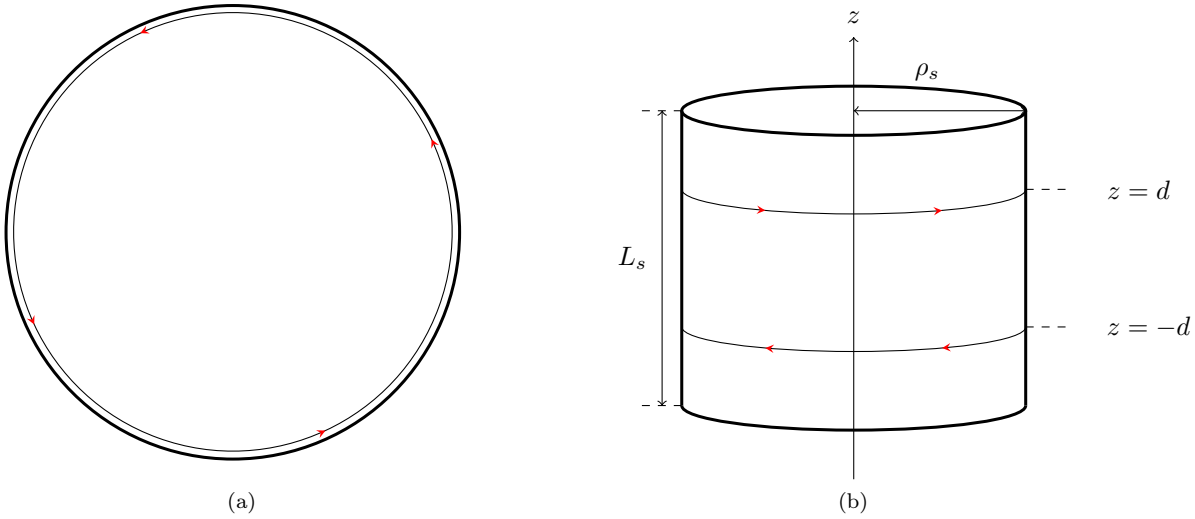


FIG. 7: Schematic diagram of an anti-symmetric pair of loops of radius ρ_s showing the (a) azimuthal variation and (b) axial position $z = \pm d$ placed symmetrically around the origin of a closed magnetic shield of radius ρ_s and length $L_s = 2\rho_s$.

The axial magnetic field generated by a pair of anti-symmetric axial loops on the shield's interior surface from (19), (22), and (23) is given by

$$B_z\left(\rho, \phi, z\right) = \frac{2\mu_0 I}{L_s} b_0^-\left(\rho, z; d\right). \tag{31}$$

As directed in the previous section, the harmonic fields in the system can be found by expanding the spatially-varying functions. By expanding these functions, we can group the spatial variations into their constituent spherical harmonic functions, and thereby determine how their effective magnitudes relate to the coil parameters. Using (25), and substituting the well-known series expansions,

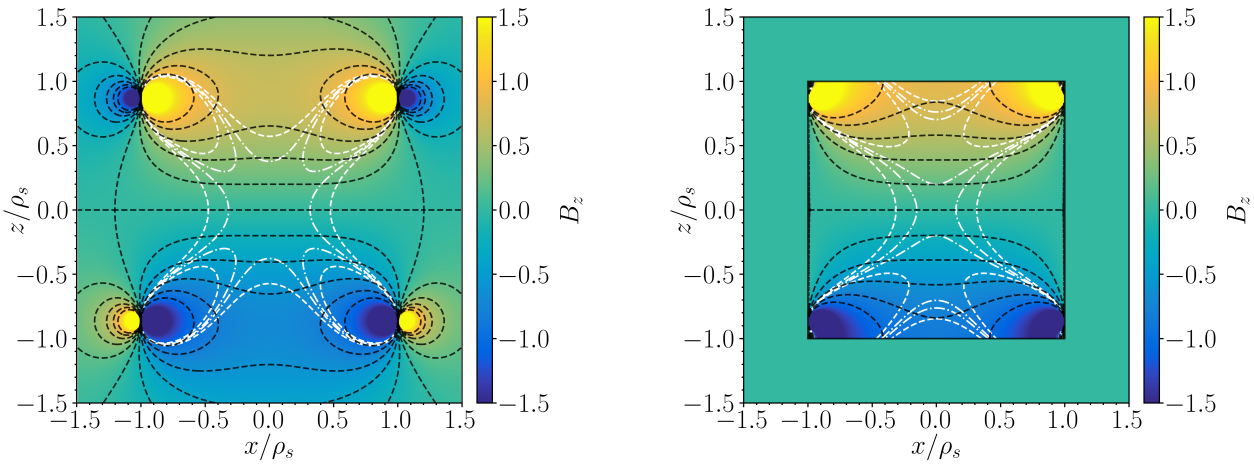
$$I_m(x) = \sum_{l=0}^{\infty} \frac{1}{l!(l+m)!}\left(\frac{x}{2}\right)^{2l+m} \qquad \text{and} \qquad \sin(x) = \sum_{l=0}^{\infty} \frac{(-1)^l x^{2l+1}}{(2l+1)!}, \tag{32}$$

the axial field generated by the anti-symmetric pair (31) can be written in terms of the harmonic fields

$$B_z\left(\rho, \phi, z\right) = \frac{2\mu_0 I}{\pi}\left(z\tilde{C}_{2,0}\left(d, \rho_s, L_s\right) + \left(\frac{z\rho^2}{4} - \frac{z^3}{6}\right)\tilde{C}_{4,0}\left(d, \rho_s, L_s\right) + \dots\right), \tag{33}$$

where the effective harmonic magnitudes are given by

$$\tilde{C}_{2n,0}\left(d,\rho_s,L_s\right)=\frac{1}{L_s^{2n-1}}\sum_{p=1}^{\infty}(2p-1)^{2n-1}\frac{\sin\left(\frac{\pi d(2p-1)}{L_s}\right)}{I_0\left(\frac{\pi(2p-1)\rho_s}{L_s}\right)}. \tag{34}$$



(a) (b)

FIG. 8: Color maps showing the magnitude of the normalized axial magnetic field, B_z, in the xz-plane generated by the coil depicted in Fig. 7 in the anti-Helmholtz arrangement with separation, $d=\pm\left(\sqrt{3}/2\right)\rho_s$ in two situations (a) in free space and (b) placed symmetrically around the origin of a closed magnetic shield of radius ρ_s and length $L_s=2\rho_s$ (solid black outline). White contours show where the field deviates from the target field by 5% (dashed curves) and 1% (dot-dashed curves). Black contours represent lines of constant magnetic flux (dashed curves). The resistance, field per unit current, and inductance of the coil both in free space and inside a unit length magnetic shield are presented in Table I.

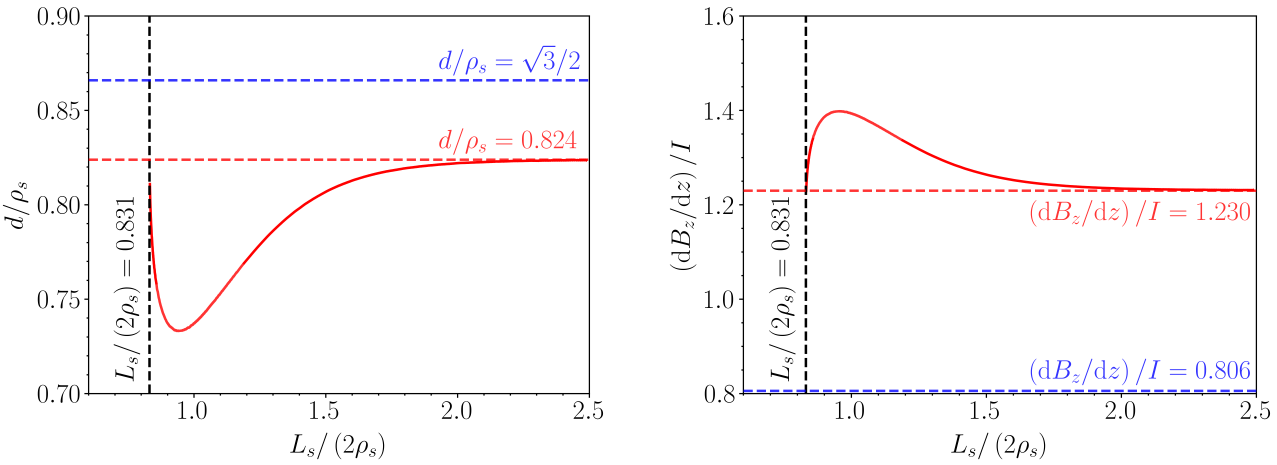
Using (34) the optimal positions, $z=\pm d$, for a single anti-symmetric pair can be determined for a given shield aspect ratio so that the leading-order error term is removed

$$\tilde{C}_{4,0}\left(d,\rho_s,L_s\right)=\frac{1}{L_s^{3}}\sum_{p=1}^{\infty}(2p-1)^{3}\frac{\sin\left(\frac{\pi d(2p-1)}{L_s}\right)}{I_0\left(\frac{\pi(2p-1)\rho_s}{L_s}\right)}=0. \tag{35}$$

In Fig. 9a-b, we present the optimal separation for any shield aspect ratio found through an exhaustive numerical search and the gradient per unit current it generates for unit shield length, respectively. The red dotted lines within Fig. 9a-b are the optimal separation, $d=0.824\rho_s$ as the shield aspect ratio tends to to infinity and the gradient per unit current, 1.23, that is generated, respectively. The blue dotted lines within Fig. 9a-b are the separation for the standard anti-Helmholtz configuration, $d=\sqrt{3}\rho_s/2$ and the gradient per unit current, 0.806, that is generated in free space, respectively. Due to the interaction and finite length of the magnetic shield there exists a shield aspect ratio, $0<L_s/(2\rho_s)\lessapprox 0.831$, where no separation entirely removes the cubic variation in the field. In this case, to determine the optimal separation contributions from both the cubic and quintic variations should be minimized, but not nulled entirely, to achieve the most uniform field linearity for a given application.

Expanding on this, we can generalize the above example using N' loops at positions d_i, to minimize $\tilde{N}$ harmonics through the use of (34), resulting in the set of simultaneous equations

$$\min_{I_i^z,d_i}\left(\sum_{i=1}^{N'}\frac{I_i^z}{L_s^{2n-1}}\sum_{p=1}^{\infty}(2p-1)^{2n-1}\frac{\sin\left(\frac{\pi d_i(2p-1)}{L_s}\right)}{I_0\left(\frac{\pi(2p-1)\rho_s}{L_s}\right)}\right),\qquad n\in\mathbb{Z}:n\in[2,\tilde{N}+1]. \tag{36}$$



(a) (b)

FIG. 9: (a) Optimal normalized separation, d/ρ_s, of the anti-symmetric pair, depicted in Fig. 7, to generate the zonal Z_2 harmonic as the length of the shield increases (red curve). Horizontal dashed lines (red and blue) show the analytical values of $d = 0.824\rho_s$ and $d = \left(\sqrt{3}/2\right)\rho_s$ obtained in the long shield limit ($L_s \gg 2\rho_s$) and in free space, respectively. (b) Gradient per current, $(\mathrm{d}B_z/\mathrm{d}z)/I$, of the optimal anti-symmetric pair as the length of the shield increases (red curve). Horizontal dashed lines (red and blue) show the values of $\mathrm{d}B_z/\mathrm{d}z = 1.230I$ and $\mathrm{d}B_z/\mathrm{d}z = 0.806I$ obtained in the long shield limit and in free space, respectively. Vertical dashed line (black) in (a) and (b) shows the minimum shield length $L_s = 1.62\rho_s$ below which no optimal solution can be found.

The manual removal of multiple harmonic fields is difficult and time consuming. To find the optimal separations each undesired harmonic must be analyzed in turn, but, as n increases, the magnitude of each harmonic becomes increasingly sensitive to the positions d_i. As such, the domain in which a solution exists that eliminates many harmonics becomes progressively more challenging to find. Moreover, to easily manufacture these nested designs, like with the azimuthal turn ratios, the axial turn ratios I_i^z should be integers within an order of magnitude range, which further increases the difficulty in finding solutions.

Clearly, unlike the simultaneous equations used to determine optimal angular lengths, the construction of this problem is nontrivial, and requires a level of intuition to solve effectively. The parity of each undesired harmonic magnitude over the domain of allowed d_i can be determined and combined to find a suitable range of I_i^z where solutions exist. From this, the domain where a solution for d_i exists can be searched efficiently. The process for determining the search regions could be automated and be performed whenever a different harmonic field is selected or the aspect ratio of the shield is altered. However, this is time consuming and can not be generalized effectively. This bounded multi-dimensional minimization problem with integer constraints is an ideal candidate for a multi-objective optimization procedure which can allow optimal positions and turn ratios to be found in a computationally-effective manner.

V. GENETIC ALGORITHM OPTIMIZATION

There are a vast array of optimization methods which can be used to find optimal solutions to minimization problems. The applicability of these methods is dependent on the functional form and number of different of objective functions. Multi-objective optimization describes a group of methods which allow the simultaneous optimization of many functions. These methods allow the optimization of conflicting objectives, resulting in a higher quality solution. Here, we use a genetic algorithm to solve the non-linear, mixed-integer, multi-objective optimization problem. The optimal continuous separations d_i and discrete turn ratios I_i^z for N' loops or arcs are found to minimize the amplitudes of a set of undesired harmonic fields, which are the objective functions, constrained by the minimum distance between any two loops D and maximum turn ratio $I^z_{\mathrm{max.}}$. We pose the optimization problem by using the set of arbitrary user-defined undesired

harmonic fields of order $n \in \mathbb{Z} : n \in [\tilde{n}_1, \tilde{n}_{\tilde{N}}]$ and degree M as the objective functions

$$\begin{cases} \min f_1 = \tilde{C}_{\tilde{n}_1,M}\left(\rho_s, L_s; d_1, \ldots, d_{N'}, I_1, \ldots, I_{N'}\right), \\ \qquad\qquad \vdots \\ \min f_{\tilde{N}} = \tilde{C}_{\tilde{n}_{\tilde{N}},M}\left(\rho_s, L_s; d_1, \ldots, d_{N'}, I_1, \ldots, I_{N'}\right). \end{cases} \tag{37}$$

Here, we assume that the required azimuthal variations have been eliminated using (27) and the remaining undesired harmonics constitute the $\tilde{N}$ leading-order error terms of degree M that exist within axial magnetic field. The search domain of the design parameters are

$$\begin{cases} D/2 < d_1 < d_2 - D, \\ d_1 + D < d_2 < d_3 - D, \\ \qquad\qquad \vdots \\ D + d_{N'-1} < d_{N'} < L_s/2, \\ 1 \leq I_1^z \leq I_{\text{max.}}^z, \\ -I_{\text{max.}}^z \leq I_2^z \leq I_{\text{max.}}^z, \\ \qquad\qquad \vdots \\ -I_{\text{max.}}^z \leq I_{N'}^z \leq I_{\text{max.}}^z, \end{cases} \tag{38}$$

where the physical constraints on the system are that the axial turn ratios are less than the maximum axial turn ratio $I_{\text{max.}}^z$, the separation of any two nested loops or arcs is less than the minimum separation D, and the outer loop arc is axially inside the shield $d_{N'} < L_s/2$.

Here, we use the MATLAB function `gamultiobj()` from the multi-objective genetic algorithm toolbox, this function uses the NSGA-II algorithm [40]. We modify the mutation, crossover, and creation functions to allow integer turn ratios and continuous value separations to be optimized simultaneously. The population size, number of generations, and function tolerance are changed depending on the number of design parameters and objective functions used in a specific design to find solutions effectively. We now present two examples of optimized coil designs found through the use of a genetic algorithm. Firstly, we design an improved linear gradient field Z_2, and compare this result to the previous anti-Helmholtz design. Then, we design a transverse bias field, $T_{1,1}$, where $m = n = 1$, which, importantly, is absent from the axial field in (14). We demonstrate how the desired field can be indirectly selected by removing the leading-order error terms that are present in the axial field. This optimized transverse coil is then compared to an equivalent non-optimized transverse coil for comparison.

Example I: Improved linear gradient field

To find an improved linear gradient field we choose to search for solutions using a four pair anti-symmetric loop setup within a magnetic shield of aspect ratio $L_s/(2\rho_s) = 1$. The axial magnetic field is given by

$$B_z\left(\rho, \phi, z\right) = \frac{2\mu_0}{L_s} \sum_{i=1}^{4} I_i^z b_0^-(\rho, z; d_i). \tag{39}$$

and we choose to minimize the first three leading-order error terms

$$\begin{cases} \min f_1 = \tilde{C}_{4,0}\left(\rho_s, L_s; d_1, \ldots, d_4, I_1^z, \ldots, I_4^z\right), \\ \min f_2 = \tilde{C}_{6,0}\left(\rho_s, L_s; d_1, \ldots, d_4, I_1^z, \ldots, I_4^z\right), \\ \min f_3 = \tilde{C}_{8,0}\left(\rho_s, L_s; d_1, \ldots, d_4, I_1^z, \ldots, I_4^z\right), \end{cases} \tag{40}$$

from (34), given by

$$\tilde{C}_{2n,0} = \sum_{i=1}^{4} \frac{I_i^z}{L_s^{2n-1}} \sum_{p=1}^{\infty} (2p-1)^{2n-1} \frac{\sin\left(\frac{\pi d_i (2p-1)}{L_s}\right)}{I_0\left(\frac{\pi(2p-1)\rho_s}{L_s}\right)}. \tag{41}$$

We constrain the separation of the wires such that $D = 0.01\rho_s$, the upper bound of the small wire approximation, and limit the maximum turn ratio $I^z_{\text{max.}} = 9$, and search for optimal values of $[d_1, \ldots, d_4]$ and $[I_1^z, \ldots, I_4^z]$. The genetic algorithm outputs numerous Pareto-optimal solutions where the first three undesired contributions are minimized, i.e. many solutions exist where no undesired harmonic can be minimized more without increasing the magnitude of another undesired harmonic. To filter these solutions, we rank them according to their stability by adjusting the wire placements slightly and analyzing their performance. The most stable solution which nearly entirely eliminates the first three unwanted harmonics from the system is depicted in Fig. 10 with axial field generated in free space and inside the magnetic shield in Fig. 11a-b, respectively. Due to the improved linearity from the additional pairs the central volume of the region to within 1% accuracy is increased by a factor of seven compared to the standard anti-Helmholtz configuration inside the same magnetic shield, shown in Fig. 8, demonstrating the effectiveness of the methodology and the applicability of the genetic algorithm optimization to this problem. However, the resistance and inductance for the improved system within the shield are an order of magnitude larger than the standard anti-Helmholtz configuration. The resistance, gradient, and inductance both in free space and inside a unit length magnetic shield are summarized in Table. I.

Although not guaranteed, there could exist other multi-pair designs that minimize more undesired harmonics than the example depicted in Fig. 10. However, the effect of removing high-order harmonics will reach a point of diminishing returns where the sensitivity of the harmonic magnitudes to the position of the loops or arcs is so large that a suitable solution can not be obtained in a reasonable amount of time. The unique benefits of discrete coil optimization are lost if too large a number of harmonics need to be nulled and the design becomes more complex, meaning a coarse discretization of a continuum-optimized current density could yield better results.

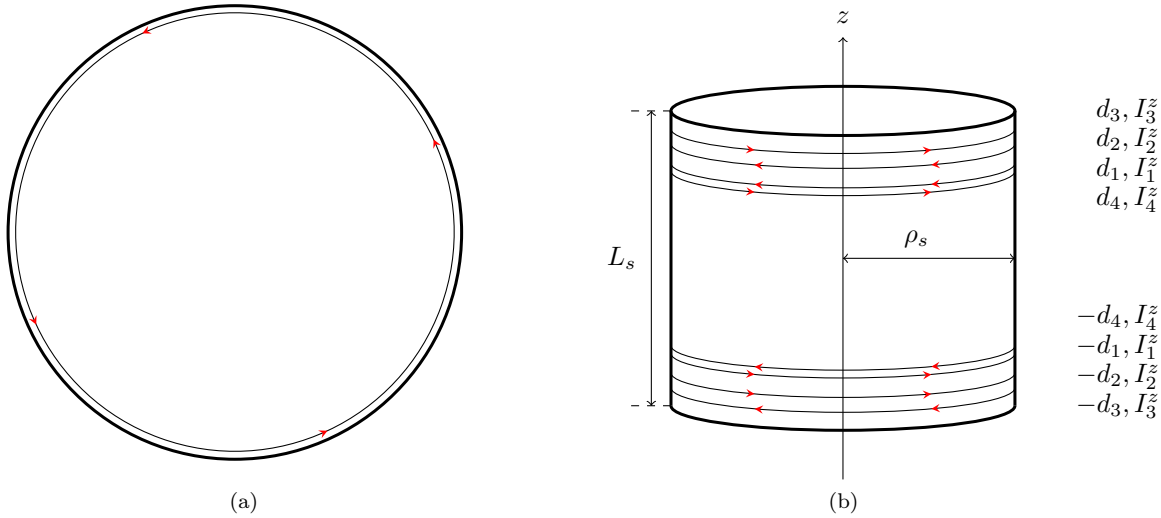
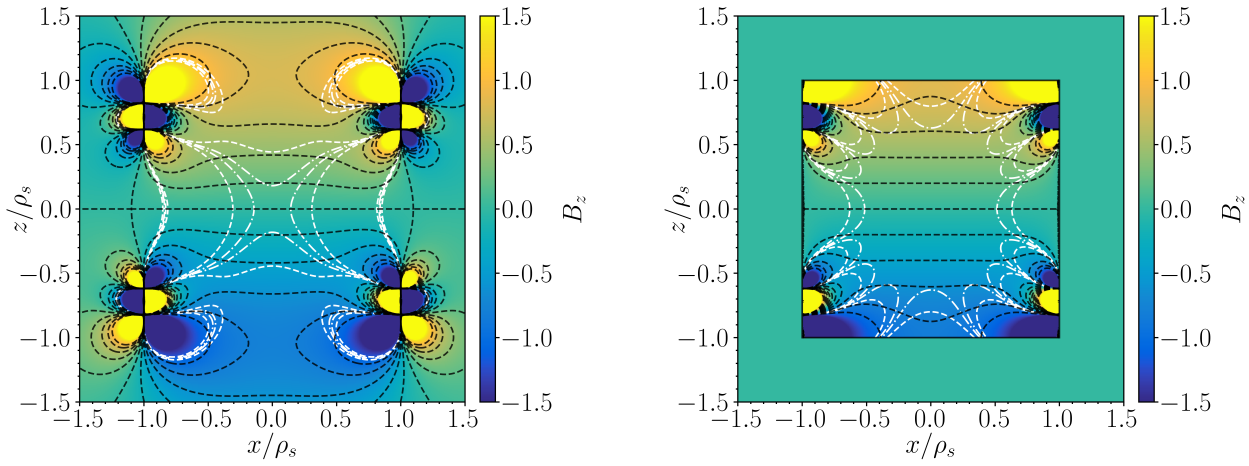


FIG. 10: Schematic diagram of four anti-symmetric loop pairs of radius ρ_s showing the (a) azimuthal variations and (b) axial positions $z = \pm d_i$, where $d_i = [0.592, 0.645, 0.777, 0.878]\rho_s$, with axial turn ratios $I_i^z = [3, -3, -2, 3]$, for $i \in \mathbb{Z} : i \in [1, 4]$, placed symmetrically around the origin of a closed magnetic shield of radius ρ_s and length $L_s = 2\rho_s$.

Example II: transverse bias field

A transverse bias field, B_x, can be represented by a single spherical harmonic field of order $n = 1$ and degree $m = 1$. As such, the symmetries within the desired harmonic field correspond to the anti-symmetric tesseral coil basis, with azimuthal periodicity π depicted in Fig. 4d and Fig. 3b, respectively. As previously mentioned, the harmonic $T_{1,1}$ is not present within the axial field. However, we can still search for optimized transverse coils using the axial magnetic



(b) (c)

FIG. 11: Color maps showing the magnitude of the normalized axial magnetic field, B_z, in the xz-plane generated the design depicted in Fig. 10 in two situations (a) in free space and (b) placed symmetrically around the origin of a closed magnetic shield of radius ρ_s and length $L_s = 2\rho_s$ (solid black outline). White contours show where the field deviates from the target field by 5% (dashed curves) and 1% (dot-dashed curves). Black contours represent lines of constant magnetic flux (dashed curves). The resistance, gradient per unit current, and inductance of the coil both in free space and inside a unit length magnetic shield are presented in Table I.

field. Here, we use a four pair setup with three overlapping arcs of different angular lengths, with axial magnetic field

$$B_z\left(\rho,\phi,z\right) = \frac{4\mu_0}{L_s}\sum_{m=1}^{\infty}\sum_{i=1}^{4}\sum_{j=1}^{3} I_i^z I_j^{\varphi} b_m^-(\rho,z;d_i)\Phi_j^m\cos(m\phi), \tag{42}$$

where

$$\Phi^m(\varphi_j) = \frac{\sin(m\varphi_j)}{\pi m}(1-(-1)^m). \tag{43}$$

Using three angular lengths, we are able to remove the first three sets of harmonics of degrees $m = (3,5,7)$ by solving the set of simultaneous equations

$$\min_{\varphi_j}\left(\sum_{j=1}^{M'} I_j^{\varphi}\sin((2\nu+1)\varphi_j)\right), \qquad \nu\in\mathbb{Z}:\nu\in[1,3]. \tag{44}$$

For simplicity and ease of manufacturing, we chose $I_j^{\varphi} = [1,1,1]$, and find optimized angular lengths of $\varphi_j = [1.367, 1.101, 0.592]$. Having removed the leading-order azimuthal errors of degrees $m = (3,5,7)$, the first three leading-order error terms in the desired field now exist in the axial field (42), and are given by

$$\tilde{C}_{2n-1,1} = \sum_{i=1}^{N} I_i^z \sum_{p=1}^{\infty}(2p-1)^{2n}\frac{\sin\left(\frac{\pi d_i(2p-1)}{L_s}\right)}{I_1\left(\frac{\pi(2p-1)\rho_s}{L_s}\right)}, \qquad n\in\mathbb{Z}:n\in[2,4]. \tag{45}$$

where the objective functions are written as

$$\begin{cases} \min f_1 = \tilde{C}_{3,1}\left(\rho_s, L_s; d_1,\ldots,d_4, I_1,\ldots,I_4\right), \\ \min f_2 = \tilde{C}_{5,1}\left(\rho_s, L_s; d_1,\ldots,d_4, I_1,\ldots,I_4\right), \\ \min f_3 = \tilde{C}_{7,1}\left(\rho_s, L_s; d_1,\ldots,d_4, I_1,\ldots,I_4\right). \end{cases} \tag{46}$$

Again, we place the constraint on the separation between wires $D = 0.01\rho_s$, and limit the maximum turn ratio such that $I^z_{\text{max.}} = 9$. Again, we select the most stable Pareto-optimal solution which effectively eliminates the first two leading-order error terms and greatly reduces the third. The solution is graphically depicted in Fig. 12 where the transverse field variations in the $xz-$plane in free space and inside the magnetic shield are shown in Fig. 13a-b, respectively. Although no standard transverse field design exists which fits within a magnetic shield with this aspect ratio, we use a non-optimized saddle coil with separation $d = L_s - \rho_w$ and azimuthal variation Fig. 12a, as the comparison. This non-optimized coil is depicted in Fig. 14. The optimized transverse coil generates a 1% homogeneous region approximately 4 times greater than the non-optimized design. However, the resistance and inductance for the optimized transverse field coils are three and ten times larger than the non-optimized arrangement. The field per unit current is also reduced by a factor of 7. The resistance, field per unit current, and inductance, for both optimized and non-optimized designs in free space and within the magnetic shield are summarized in Table. I.

Additional constraints could be added to the optimization to minimize the resistance, inductance, or to maximized the field per current. However, this would come at a cost of field fidelity. For a given experimental situation, the Pareto-optimal solutions should be ranked according to achieve the most optimal outcome.

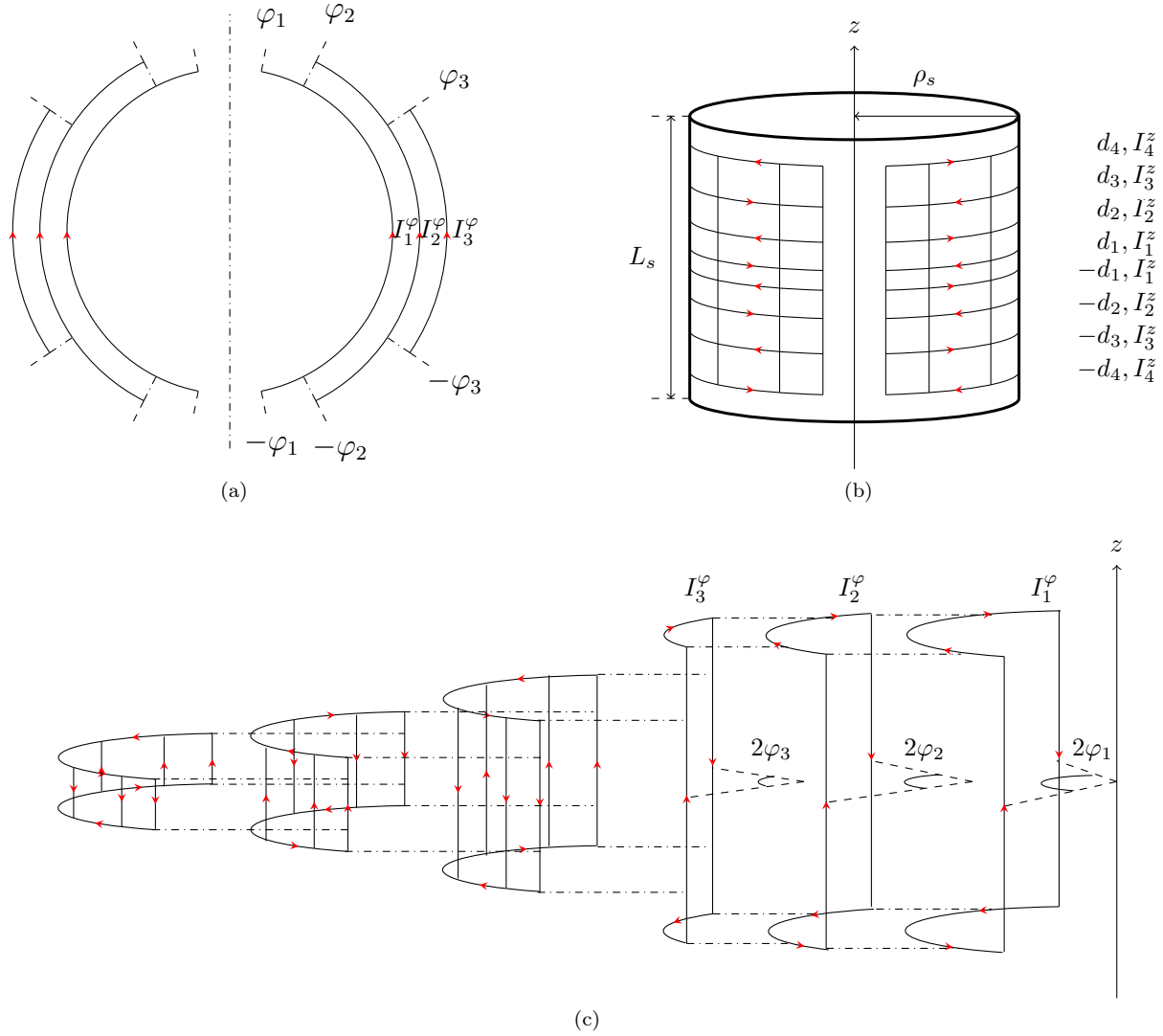
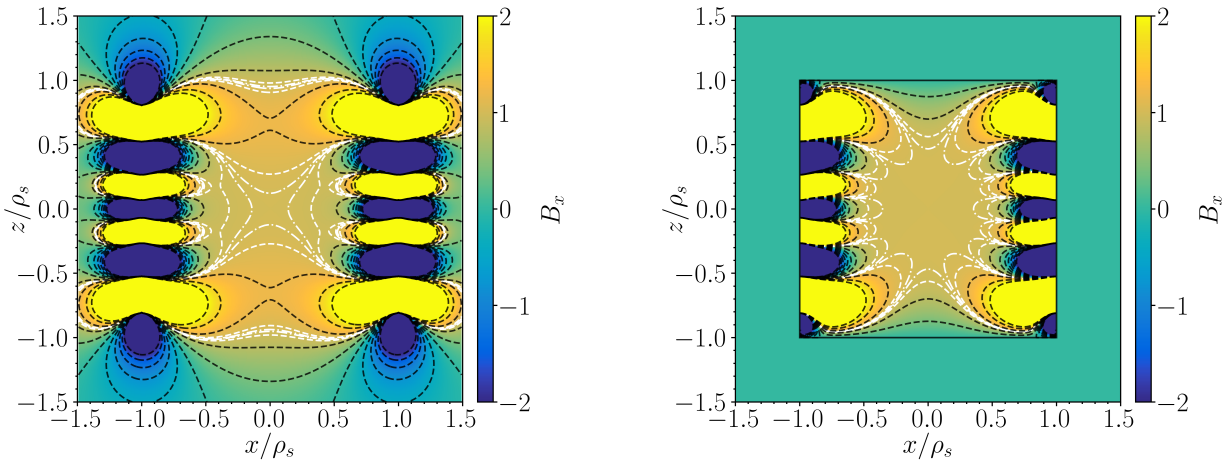
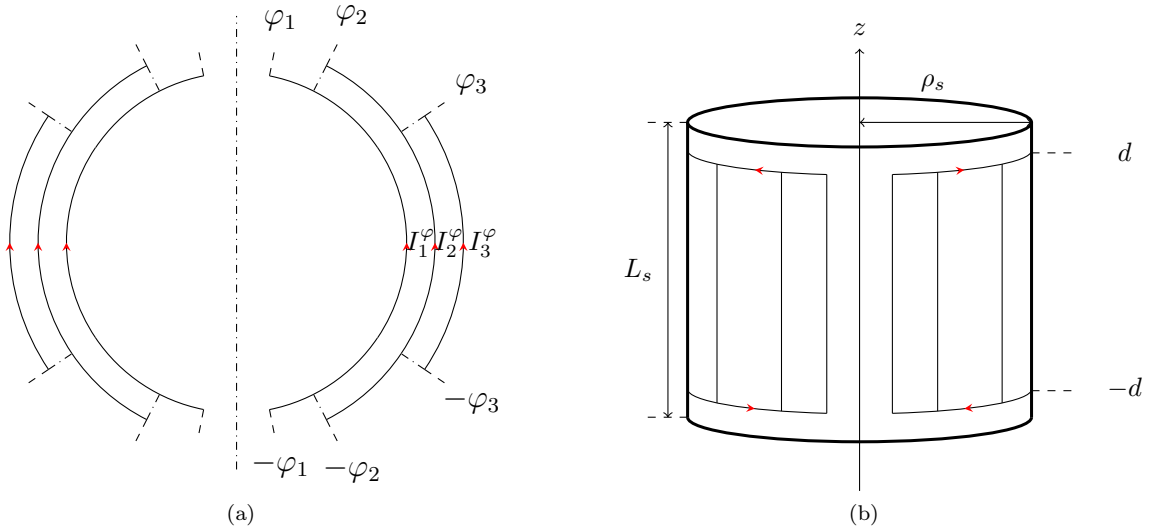


FIG. 12: Schematic diagram of four axial anti-symmetric arc pairs of radius ρ_s with three azimuthal variations for each pair, showing the (a) azimuthal variations of periodicity, π, for the three separate angular lengths $\varphi_j = [1.376, 1.101, 0.593]$ with azimuthal turn ratios $I^\varphi_j = [1, 1, 1]$, for $j \in \mathbb{Z} : j \in [1, 3]$, and (b) axial positions $z = \pm d_i$, where $d_i = [0.068, 0.226, 0.525, 0.810]\rho_s$, with axial turn ratios $I^z_i = [5, -3, 2, -1]$, for $i \in \mathbb{Z} : i \in [1, 4]$, placed symmetrically around the origin of a closed magnetic shield of radius ρ_s and length $L_s = 2\rho_s$. (c) Shows an expanded schematic diagram of one azimuthal section of the coil depicted in (a)-(b) for clarity.



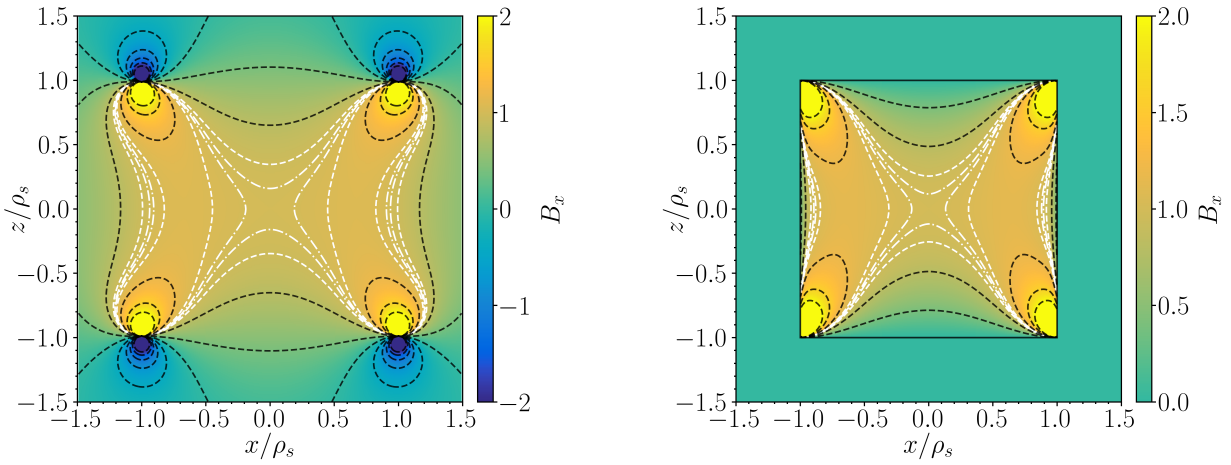
(c) (d)

FIG. 13: Color maps showing the magnitude of the normalized transverse magnetic field, B_x, in the xz-plane generated the design depicted in Fig. 12 in two situations (a) in free space and (b) placed symmetrically around the origin of a closed magnetic shield of radius ρ_s and length $L_s = 2\rho_s$ (solid black outline). White contours show where the field deviates from the target field by 5% (dashed curves) and 1% (dot-dashed curves). Black contours represent lines of constant magnetic flux (dashed curves). The resistance, field per unit current, and inductance of the coil both in free space and inside a unit length magnetic shield are presented in Table I.



(a) (b)

FIG. 14: Schematic diagram of one axial anti-symmetric arc pair of radius ρ_s with three azimuthal variations, showing the (a) azimuthal variations of periodicity, π, for the three separate angular lengths $\varphi_j = [1.376, 1.101, 0.593]$ with azimuthal turn ratios $I_j^\varphi = [1, 1, 1]$, for $j \in \mathbb{Z} : j \in [1, 3]$, and (b) axial positions $z = \pm d$, where $d = (L_s/2 - \rho_w)\rho_s$, placed symmetrically around the origin of a closed magnetic shield of radius ρ_s and length $L_s = 2\rho_s$.



(b) (c)

FIG. 15: Color maps showing the magnitude of the normalized transverse magnetic field, B_x, in the xz-plane generated the design depicted in Fig. 14 in two situations (a) in free space and (b) placed symmetrically around the origin of a closed magnetic shield of radius ρ_s and length $L_s = 2\rho_s$ (solid black outline). White contours show where the field deviates from the target field by 5% (dashed curves) and 1% (dot-dashed curves). Black contours represent lines of constant magnetic flux (dashed curves). The resistance, field per unit current, and inductance of the coil both in free space and inside a unit length magnetic shield are presented in Table I.

Coil Design		Resistance (Ω)	Field / Current (μT/m$^{\text{N-1}}$)	Inductance (μH)
Anti-Helmholtz	Unshielded	0.134	3.28	6.19
	Shielded		7.16	12.4
Improved Linear Gradient	Unshielded	1.48	2.74	131
	Shielded		6.92	184
Non-Optimized Transverse	Unshielded	1.03	4.21	51.8
	Shielded		6.88	104
Optimized Transverse	Unshielded	3.63	0.65	724
	Shielded		1.04	1010

TABLE I: The resistance R, field per unit current C_{NM}/I, and inductance L, for example coils, with wire radius $\rho_w = 0.5$ mm, depicted in the text both in free space and inside an example magnetic shield of unit length $L_s = 1$ m and radius $\rho_s = 0.5$ m. The anti-Helmholtz and improved linear gradient coils are represented in Fig. 7 and Fig. 10, respectively, and generate a $N = 2$ zonal harmonic field, Z_2. The non-optimized and optimized transverse coils are represented in Fig. 14 and Fig. 12, respectively, and generate a $N = 1$, $M = 1$ tesseral harmonic field, $T_{1,1}$.

VI. CONCLUSION

Here, we have provided a coil design method based around simple discrete loops and arcs, allowing the construction of any physical magnetic field within a magnetically shielded cylinder. We utilized a previously formulated Green's function that satisfies the boundary conditions at the surface of a high-permeability cylinder and determined simplified equations with leading-order corrections when the coil is resting on the magnetic shield's surface. We then presented a discrete coil basis composed of unit-coil building blocks. The magnetic fields generated by these

building blocks were then decomposed into the set of harmonic magnetic fields generated in free space. The coil parameters, namely the spacing, angular lengths, and currents through pairs of loops and arcs, were then related to the set of harmonic fields within a specific design and chosen to select desired field profiles within the system. Finally, we used this decomposition to find optimal discrete coil designs using a genetic algorithm optimization procedure.

Using the anti-Helmholtz pair as an example, we found that the central volume of 1% field gradient linearity diminished by a factor of three when placed inside a high-permeability shield of equal length and diameter. We then used our model to investigate the optimal separation of an anti-Helmholtz pair in a magnetic shield of arbitrary length. Taking this optimization one step further, we formulated simultaneous equations to remove multiple harmonic fields using multiple loops and arcs and used a genetic algorithm to find optimized turn ratios and separations. We applied this optimization procedure to design a high fidelity transverse bias and linear-gradient field. Notably, we found that the improved linear-gradient design increased the central volume of 1% linearity by a factor of seven compared to the standard anti-Helmholtz arrangement in the same shield. However, this came at a cost of increased power and inductance.

The analytical model, discrete coil basis, and optimization procedure presented here allow the efficient design of compact discrete coils that generate accurate magnetic fields within a finite length cylindrical magnetic shield. This methodology will facilitate new miniaturized technologies that require custom magnetic fields within a magnetically shielded environment, and existing systems can easily be retrofitted to include simple discrete coils. Additional objective functions could be added to the method such as sensitivity of the harmonic magnitudes to wire placement or the minimization of power or inductance. These additions may come at the cost of field fidelity but would allow the method to be tailored to the needs of individual experiments. Further research could investigate the use of discrete planar coils on the surface of the end-plates to enable more power-efficient and accurate designs, or the coil basis could be applied to generate self-canceling free space discrete coil sets with significant optical access.

ACKNOWLEDGMENTS

We acknowledge support from the UK Quantum Technology Hub Sensors and Timing, funded by the Engineering and Physical Sciences Research Council (EP/M013294/1).
The authors M.P., P.J.H., T.M.F., M.J.B., and R.B. declare that they have a patent pending to the UK Government Intellectual Property Office (Application No.1913549.0) regarding the magnetic field optimization techniques described in this work. N.H, M.J.B, and R.B also declare financial interests in a University of Nottingham spin-out company, Cerca. The authors have no other competing financial interests.

APPENDIX A: AXIAL DIFFERENTIATION OF SPHERICAL HARMONICS

Let us consider the harmonic

$$R_{n,m}(r,\theta,\phi) = r^n P_{n,m}\left(\cos\theta\right) \begin{pmatrix} \cos\left(|m|\phi\right) \\ \sin\left(|m|\phi\right) \end{pmatrix}, \qquad \begin{matrix} m \geq 0 \\ m < 0 \end{matrix} \tag{47}$$

The differential of an arbitrary curvilinear coordinate system with respect to another may be expressed as

$$\frac{\partial R_{n,m}(r,\theta,\phi)}{\partial \chi_i} = \sum_j \frac{\partial \xi_j}{\partial \chi_i} \frac{\partial}{\partial \xi_j} R_{n,m}(r,\theta,\phi). \tag{48}$$

Using this, the differential in cylindrical coordinates may be determined. Spherical polar coordinates can be written as

$$r = \sqrt{\rho^2 + z^2}, \qquad \theta = \cos^{-1}\left(\frac{z}{\sqrt{\rho^2+z^2}}\right), \qquad \phi = \phi. \tag{49}$$

As a result the axial derivative is written by

$$\frac{\partial R_{n,m}(r,\theta,\phi)}{\partial z} = \left(\frac{\partial r}{\partial z}\frac{\partial}{\partial r} + \frac{\partial \theta}{\partial z}\frac{\partial}{\partial \theta}\right) R_{n,m}(r,\theta,\phi), \tag{50}$$

Using (48) and (49) the differential with respect to z is given simply by

$$\frac{\partial R_{n,m}(r,\theta,\phi)}{\partial z} = \left(\cos\theta\frac{\partial}{\partial r} - \frac{\sin\theta}{r}\frac{\partial}{\partial\theta}\right) R_{n,m}(r,\theta,\phi), \tag{51}$$

which, using (47), becomes

$$\frac{\partial R_{n,m}(r,\theta,\phi)}{\partial z} = r^{n-1}\left(n\cos\theta P_{n,m}\left(\cos\theta\right) - \sin\theta\frac{\partial P_{n,m}\left(\cos\theta\right)}{\partial\theta}\right)\begin{pmatrix}\cos\left(|m|\phi\right) & m\geq 0\\ \sin\left(|m|\phi\right) & m<0\end{pmatrix}, \tag{52}$$

Directly substituting the relation from [51]

$$\frac{\partial P_{n,m}\left(\cos\theta\right)}{\partial\theta} = m\cot\theta P_{n,m}\left(\cos\theta\right) - \frac{n+m}{\sin\theta}P_{n-1,m}\left(\cos\theta\right) \tag{53}$$

into (52) yields the final expression

$$\frac{\partial R_{n,m}(r,\theta,\phi)}{\partial z} = (n+m)P_{n-1,m}\left(\cos\theta\right)\begin{pmatrix}\cos\left(|m|\phi\right) & m\geq 0\\ \sin\left(|m|\phi\right) & m<0\end{pmatrix}, \tag{54}$$

APPENDIX B: HARMONIC DECOMPOSITION OF ANTI-HELMHOLTZ CONFIGURATION

An anti-Helmholtz configuration generates axial linear gradient with an axial anti-symmetric setup, $z' = \pm d$, with complete azimuthal symmetry, $\Phi = 1$. Let us find the optimal anti-Helmholtz separation in an unshielded environment first using a spherical harmonic decomposition. Using the known magnetic field generated by a circular loop in free space [50] the axial field generated by an anti-symmetric setup of radius ρ_c without a magnetic shield is given by

$$B_z\left(\rho,\phi,z\right) = \frac{2\mu_0 I}{\rho_c\pi}\int_0^\infty \mathrm{d}k\ k\sin\left(\frac{kz}{\rho_c}\right)\sin\left(\frac{kd}{\rho_c}\right)I_0\left(\frac{k\rho}{\rho_c}\right)K_1(k). \tag{55}$$

In order to determine the optimal separation the field must be decomposed into its orthogonal eigenfunctions. This can be done through expanding the spatially-varying terms, separating the harmonic fields generated, and removing the leading-order error in the desired field. Taylor expanding (55) and grouping the terms into the harmonic fields in cylindrical coordinates results in

$$B_z\left(\rho,\phi,z\right) = \frac{2\mu_0 I}{\rho_c\pi}\left(z\tilde{C}_{2,0}\left(\rho_c,d\right) + \left(\frac{z\rho^2}{4} - \frac{z^3}{6}\right)\tilde{C}_{4,0}\left(\rho_c,d\right) + \dots\right), \tag{56}$$

where $\tilde{C}_{2,0}\left(\rho_c,d\right)$, $\tilde{C}_{4,0}\left(\rho_c,d\right)$, …, $\tilde{C}_{2n,0}\left(\rho_c,d\right)$ are the relative magnitudes of the harmonics in (15), respectively, which are dependent on the coil geometry, given by

$$\tilde{C}_{2n,0}\left(d,\rho_c\right) = \frac{1}{\rho_c^{2n-1}}\int_0^\infty \mathrm{d}k\ k^{2n}\sin\left(\frac{kd}{\rho_c}\right)K_1(k). \tag{57}$$

To design an optimal linear gradient field using this set-up, the leading-order error in the desired field must be removed. Therefore, to remove the cubic variations in the field it is required that

$$\tilde{C}_{4,0} = \frac{1}{\rho_c^3}\int_0^\infty \mathrm{d}k\ k^4\sin\left(\frac{kd}{\rho_c}\right)K_1(k) = \frac{15\rho_c^3 d\left(3\rho_c^2 - 4d^2\right)\pi}{2\left(\rho_c^2+d^2\right)^{\frac{9}{2}}} = 0. \tag{58}$$

As expected, this is satisfied at the standard anti-Helmholtz separation $d/\rho_c = \sqrt{3}/2$.

---

[1] F. Roméo and D. I. Hoult, Magnet field profiling: analysis and correcting coil design, Magn. Reson. Med. **1**, 1 (1984).
[2] S. Pissanetzky, Minimum energy MRI gradient coils of general geometry, Meas. Sci. Technol. **3**, 7 (1992).
[3] M. Poole and R. Bowtell, Novel gradient coils designed using a boundary element method, Concept Magn. Reson. B **3**, 162–175 (2007).
[4] N. Holmes, T. M. Tierney, J. Leggett, E. Boto, S. Mellor, G. Roberts, R.M. Hill, V. Shah, G.R. Barnes, M.J. Brookes, and R. Bowtell, Balanced, bi-planar magnetic field and field gradient coils for field compensation in wearable magnetoencephalography, Sci. Rep. **9**, 14196 (2019).
[5] L.K. Forbes and S. Crozier, A novel target-field method for finite-length magnetic resonance shim coils: I. Zonal shims, J. Phys. D: Appl. Phys. **34**, 3447 (2001).
[6] L.K. Forbes and S. Crozier, A novel target-field method for finite-length magnetic resonance shim coils: II. Tesseral shims, J. Phys. D: Appl. Phys. **35**, 839 (2002).
[7] L.K. Forbes and S. Crozier, A novel target-field method for magnetic resonance shim coils: III. Shielded zonal and tesseral coils, J. Phys. D: Appl. Phys. **36**, 68 (2002).
[8] X. Wu, Z. Pagel, B. S. Malek, T. H. Nguyen, F. Zi, D. S. Scheirer, and H. Müller, Gravity surveys using a mobile atom interferometer, Sci. Adv. **5**, 9 (2019).
[9] V. Menoret, P. Vermeulen, N. L. Moigne, S. Bonvalot, P. Bouyer, A. Landragin, and B. Desruelle, Gravity measurements below 10^{-9} g with a transportable absolute quantum gravimeter, Sci. Rep. **8**, 1 (2018).
[10] M. J. Snadden, J. M. McGuirk, P. Bouyer, K. G. Haritos, and M. A. Kasevich, Measurement of the Earth's gravity gradient with an atom interferometer-based gravity gradiometer, Phys. Rev. Lett. **81**, 971 (1998).
[11] K. Bongs, M. Holynski, J. Vovrosh, P. Bouyer, G. Condon, E. Rasel, C. Schubert, W. P. Schleich, and A. Roura, Taking atom interferometric quantum sensors from the laboratory to real-world applications, Nat. Rev. Phys. **1**, 731 (2019).
[12] I. Moric, P. Laurent, P. Chatard, C.-M. de Graeve, S. Thomin, V. Christophe, and O. Grosjean, Magnetic shielding of the cold atom space clock PHARAO, Acta Astronaut. **102**, 287 (2014).
[13] L. Liu, D.-S. Lü, W.-B. Chen, T. Li, Q.-Z. Qu, B. Wang, L. Li, W. Ren, Z.-R. Dong, J.-B. Zhao, W.-B. Xia, X. Zhao, J.-W. Ji, M.-F. Ye, Y.-G. Sun, Y.-Y. Yao, D. Song, Z.-G. Liang, S.-J. Hu, and Y.-Z. Wang, In-orbit operation of an atomic clock based on laser-cooled ^{87}Rb atoms, Nat. Commun. **9**, 2760 (2018).
[14] B. Patton, E. Zhivun, D. C. Hovde, and D. Budker, All-optical vector atomic magnetometer, Phys. Rev. Lett. **113**, 013001 (2014).
[15] Y. J. Kim and I. Savukov, Ultra-sensitive magnetic microscopy with an optically pumped magnetometer, Sci. Rep. **6**, 24773 (2016).
[16] H. Zhang, S. Zou, X. Chen, and W. Quan, Parameter modeling analysis and experimental verification on magnetic shielding cylinder of all-optical atomic spin magnetometer, J. Sens. **5**, 491746 (2015).
[17] M. V. Romalis and H. B. Dang, Atomic magnetometers for materials characterization, Mater. Today, **14**, 6 (2011).
[18] E. Boto *et al.*, Moving magnetoencephalography towards real-world applications with a wearable system, Nature **555**, 657–661 (2018).
[19] R.M. Hill *et al.*, Multi-channel whole-head OPM-MEG: Helmet design and a comparison with a conventional system, NeuroImage **219**, 116995 (2020).
[20] T.M. Tierney *et al.*, Optically pumped magnetometers: From quantum origins to multi-channel magnetoencephalography, NeuroImage **199**, 598–608 (2019).
[21] A. Borna *et al.*, Non-Invasive Functional-Brain-Imaging with an OPM-based Magnetoencephalography System, PLOS ONE **15**, 1–24 (2020).
[22] H. Eswaran, D Escalona-Vargas, E.H. Bolin, J.D. Wilson, and C.L. Lowery, Fetal magnetocardiography using optically pumped magnetometers: a more adaptable and less expensive alternative?, Prenat Diagn. **37**, 193–196 (2017).
[23] S. Lew, M.S. Hämäläinen, and Y. Okada, Toward noninvasive monitoring of ongoing electrical activity of human uterus and fetal heart and brain, Clinical Neurophysiology **128**, 2470–2481 (2017).
[24] S. Strand, W. Lutter, J.F. Strasburger, V.k. Shah, O. Baffa, and R.T. Wakai, Low-Cost Fetal Magnetocardiography: A Comparison of Superconducting Quantum Interference Device and Optically Pumped Magnetometers, Journal of the American Heart Association **8**, 16 (2019).
[25] A. Mager, Magnetic shielding efficiencies of cylindrical shells with axis parallel to the field, J. Appl. Phys. **39**, 1914 (1968).
[26] S. S. Grabchikov, A. V. Trukhanov, S. V. Trukhanov, I. S. Kazakevich, A. A. Solobay, V. T. Erofeenko, N. A. Vasilenkov, O. S. Volkova, and A. Shakin, Effectiveness of the magnetostatic shielding by the cylindrical shells, J. Magn. Magn. Mater. **398**, 49 (2016).
[27] J. Prat-Camps, C. Navau, D. Chen, and A. Sanchez, Exact analytical demagnetizing factors for long hollow cylinders in transverse field, IEEE Magn. Lett. **3**, 0500104 (2012).
[28] S. Celozzi, R. Araneo, and G. Lovat, Appendix B: Magnetic Shielding, John Wiley & Sons Ltd. (2008).
[29] A.J. Mäkinen, R. Zetter, J. Iivanainen, K.C.J. Zevenhoven, L. Parkkonen, and R.J. Ilmoniemi, Magnetic field modeling with surface currents. Part I. Implementation and usage of bfieldtools, J. Appl. Phys **128**, 063906 (2020).

[30] R. Zettera, A.J. Mäkinen, J. Iivanainen, K.C.J. Zevenhoven, R.J. Ilmoniemi, and L. Parkkonen, Magnetic field modeling with surface currents. Part II. Implementation and usage of bfieldtools, J. Appl. Phys **128**, 063905 (2020).
[31] M. Packer, P.J. Hobson, N. Holmes, J. Leggett, P. Glover, M.J. Brookes, R. Bowtell, and T.M. Fromhold, Optimal Inverse Design of Magnetic Field Profiles in a Magnetically Shielded Cylinder, Phys. Rev. Applied **14**, 054004 (2020).
[32] M. Packer, P.J. Hobson, N. Holmes, J. Leggett, P. Glover, M.J. Brookes, R. Bowtell, and T.M. Fromhold, Planar Coil Optimization in a Magnetically Shielded Cylinder, arXiv 2101.01275 (2021).
[33] C.-Y. Liu, T. Andalib, D. C. M. Ostapchuk, and C. P. Bidinosti, Analytic models of magnetically enclosed spherical and solenoidal coils, Nucl. Instrum. Methods Phys. Res. **949**, 162837 (2020).
[34] R. Lambert and C. Uphoff, Magnetically shielded solenoid with field of high homogeneity, Rev. Sci. Instrum. **46**, 3 (1975).
[35] R. J. Hanson and F. M. Pipkin, Magnetically shielded solenoid with field of high homogeneity, Rev. Sci. Instrum. **36**, 2 (1965).
[36] T. Liu, A. Schnabel, Z. Sun, J. Voigt and L. Li, Approximate expressions for the magnetic field created by circular coils inside a closed cylindrical shield of finite thickness and permeability, J. Magn. Magn. Mater. **507**, 0304-8853 (2020).
[37] H. Tamaki, H. Kita and S. Kobayashi, Multi-objective optimization by genetic algorithms: a review, Proceedings of IEEE International Conference on Evolutionary Computation 517-522 (1996).
[38] H. Tamaki, H. Kita, and S. Kobayashi, Genetic algorithms for modelling and optimisation, Journal of Computational and Applied Mathematics **184**, 205-222 (2005).
[39] K. Deb, Multi-Objective Optimization Using Evolutionary Algorithms, Wiley New York (2001).
[40] K. Deb, A. Pratap, S. Agarwal, and T. Meyarivan A fast and elitist multiobjective genetic algorithm: NSGA-II, IEEE Transactions on Evolutionary Computation **6**, 2 182 (2002).
[41] M. Sakakibara and G. Uehara and Y. Adachi and T. Meguro, Evaluation of Heat Treatment of Mu-Metal Based on Permeability Under Very-Low-Frequency Micromagnetic Fields, IEEE Transactions on Magnetics **57**, 2, (2021).
[42] J. D. Jackson, Classical electrodynamics (3rd ed.), Wiley New York (1998).
[43] P. Hammond, Electric and magnetic images, Proc. IEE Part C Monogr. **107**, 306 (1960).
[44] W.A. Roshen, Effect of finite thickness of magnetic substrate on planar inductors, IEEE Trans. Magn. **26**, 270 (1990).
[45] J. R. Corea, A. M. Flynn, B. Lechene, G. Scott, G. D. Reed, P. J. Shin, M. Lustig, and A. C. Ariasb, Screen-printed flexible MRI receive coils, Nat. Commun. **7**, 10839 (2016).
[46] T. D. Ngo, A. Kashani, G. Imbalzano, K. T. Q. Nguyen, and D. Hui, Additive manufacturing (3D printing): A review of materials, methods, applications and challenges, Compos. B. Eng. **143**, 172 (2018).
[47] M. J. E Golay, Saddle coils for uniform static magnetic field generation in NMR experiments, Concept Magn. Reson. B **29**B(1), 9-19 (2016).
[48] M. J. E Golay, Field homogenizing coils for nuclear spin resonance instrumentation, Rev Sci Instrum **29**, 313-315 (1958).
[49] https://twinleaf.com/shield/MS-1L/.
[50] R. Turner, A target field approach to optimal coil design, J. Phys. D: Appl. Phys. **19**, 8 (1986).
[51] P. M. Morse and H. Feshbach, Methods of Theoretical Physics, McGraw-Hill Book Comp. New York (1953).

Chapter 6

Conclusion

A complete design method has been formulated within this body of work that allows the generation of quasi-static magnetic fields within closed, finite-length high-permeability cylinders. The magnetic shield's response was formulated in terms of the initial current source such that the magnetic field could be found in terms of a coil basis and efficiently optimized to generate hybrid field-generating systems. Each magnetic field design method presented a different solution to optimal magnetic field design, with their own advantages and disadvantages, benefiting a wide range of applications.

Arbitrary cylindrical coils or cylindrical current distributions provide accurate fields within magnetic shields with large aspect ratios. Due to the geometry of the coil, these systems provide extensive axial access but reduced radial access. The interaction of the cylindrical currents with the cylindrical surface of the shield also magnifies the magnetic field. Therefore, these systems are advantageous within experiments such as gravity gradient atom interferometers where the region of interest is long and thin, requiring large amounts of free space in the axial direction. One downside of this method is that accurate fields in regions close to the magnetic shield's end caps are hard to generate. This difficulty arises due to the form of the interaction and geometric limitations of the cylindrical current source. The planar end caps oppose the fields generated by the current source due to the reflected image currents, resulting in large

gradient fields.

Conversely, arbitrary planar currents are beneficial in the geometrically opposite scenario. These systems provide accurate fields within cylinders with small aspect ratios. This coil geometry provides large amounts of radial access with reduced axial access. Due to the planar coil's interaction with the shield, magnetic fields are easily made in regions close to the planar end caps but hard to make radially close to the cylindrical surface. This design method could benefit systems that are limited by axial size constraints. These designs are also easily manufactured and retrofitted within existing systems allowing for improvements within systems without system redesign.

Due to the systems' symmetries and the form of the current sources' interactions with the magnetic shield, a combination of both planar and cylindrical currents could maximize the benefits of each coil geometry. This combination of designs could lead to ultra-precise field generating systems that are both axially and radially large. However, due to the designs' complexity, these systems would lack access and would have to be designed carefully to accommodate it. Discrete coil systems provide a compromise with flexible optical access both axially and radially but with limited field accuracy. However, since these designs are composed of simple building blocks, they can be manufactured relatively easily and provide cost-effective solutions. These designs could be helpful when large amounts of access is required, and the constraint on the magnetic field's accuracy is flexible.

These methods can be used effectively when the material thickness is greater than 0.5 mm, the material's permeability is $\mu_r \gg 20000$, and the frequency of the initial current source is $\omega \approx 0$. However, these conditions are not always met. Some experiments require time-varying fields, lightweight, and low-noise systems. The finite frequency, permeability, and thickness could introduce deviations from the analytical model within these systems. If these deviations are small, iterative numerical optimization using finite element software could be performed to adjust the current density to account for these parameters.

This optimization could be achieved by particle swarm, genetic algorithm, or any other efficient optimization procedure that can traverse the highly non-linear optimization landscape. In extreme cases, where the frequency of the time-varying fields is the kHz regime, or the permeability and thickness are too low, the theoretical model presented breaks down, and minor adjustments to the approximate solution are no longer valid. In this case, further analytical models need to be formulated to take the eddy current mechanism, and finite permeability and thickness into account. This inclusion would only be possible if the complete time-dependent solution is found, including the material's conductivity, permeability, and thickness, and could be an area of further research.

These methods provide a solution for a priori quasi-static magnetic field design within high-permeability finite-length cylindrical shields, which are currently being used in the development of gravity sensors at the University of Birmingham, low-field environments for medical imaging at the University of Nottingham, and a commercial shielding product being manufactured by Magnetic Shields Limited. Future applications could include compact hybrid cancellation systems for quantum computers, miniaturized gravity sensors, and other developing quantum technologies which require magnetic shielding, resulting in the next generation of commercialized quantum technologies.

Bibliography

[1] J. E. C. Williams, "Superconducting magnets for mri," *IEEE Transactions on Nuclear Science*, vol. 31, no. 4, pp. 994–1005, 1984.

[2] P. Konzbul and K. Sveda, "Shim coils for NMR and MRI solenoid magnets," *Measurement Science and Technology*, vol. 6, no. 8, pp. 1116–1123, 1995.

[3] S. Hidalgo-Tobon, "Theory of gradient coil design methods for magnetic resonance imaging," *Concepts in Magnetic Resonance Part A*, vol. 36A, no. 4, pp. 223–242, 2010.

[4] T. Zhang, "Keynote talk — superconducting magnets for mri applications," in *2013 IEEE International Conference on Applied Superconductivity and Electromagnetic Devices*, 2013, pp. 537–537.

[5] T. Tadic and B. G. Fallone, "Design and optimization of superconducting mri magnet systems with magnetic materials," *IEEE Transactions on Applied Superconductivity*, vol. 22, no. 2, pp. 4 400 107–4 400 107, 2012.

[6] M. A. Brideson, L. K. Forbes, and S. Crozier, "Determining complicated winding patterns for shim coils using stream functions and the target-field method," *Concepts in Magnetic Resonance*, vol. 14, no. 1, pp. 9–18, 2002.

[7] R. Turner, "Gradient coil design: A review of methods," *Magnetic Resonance Imaging*, vol. 11, no. 7, pp. 903–920, 1993.

[8] M. Coleman and S. McIntosh, "The design and optimisation of tokamak poloidal field systems in the blueprint framework," *Fusion Engineering and Design*, vol. 154, p. 111544, 2020.

[9] R. Schmied, J. H. Wesenberg, and D. Leibfried, "Optimal surface-electrode trap lattices for quantum simulation with trapped ions," *Phys. Rev. Lett.*, vol. 102, p. 233002, 2009.

[10] R. Schmied, D. Leibfried, R. J. C. Spreeuw, and S. Whitlock, "Optimized magnetic lattices for ultracold atomic ensembles," *New Journal of Physics*, vol. 12, no. 10, p. 103029, 2010.

[11] C. J. Dedman, R. G. Dall, L. J. Byron, and A. G. Truscott, "Active cancellation of stray magnetic fields in a bose-einstein condensation experiment," *Review of Scientific Instruments*, vol. 78, no. 2, p. 024703, 2007.

[12] D. C. Aveline, J. R. Williams, E. R. Elliott, C. Dutenhoffer, J. R. Kellogg, J. M. Kohel, N. E. Lay, K. Oudrhiri, R. F. Shotwell, N. Yu, and R. J. Thompson, "Observation of bose–einstein condensates in an earth-orbiting research lab," *Nature*, vol. 582, pp. 193–197, 2020.

[13] S. Fray and M. Weitz, "Atom-based test of the equivalence principle," *Space Sci. Rev.*, vol. 148, pp. 225–232, 2009.

[14] R. Bouchendira, P. Clade, S. Guellati-Khelifa, F. Nez, and F. Biraben, "New determination of the fine structure constant and test of the quantum electrodynamics," *Phys. Rev. Lett.*, vol. 106, 2011.

[15] R. Geiger, L. Amand, A. Bertoldi, B. Canuel, W. Chaibi, C. Danquigny, I. Dutta, B. Fang, S. Gaffet, J. Gillot, D. Holleville, A. Landragin, M. Merzougui, I. Riou, D. Savoie, and P. Bouyer, "The matter-wave laser interferometer gravitation antenna (MIGA): New perspectives for fundamental physics and geosciences," Proceedings of the 50th Rencontres de Moriond "100 years after GR", La Thuile, Italy, 2015.

[16] B. Battelier, B. Barrett, L. Fouché, L. Chichet, L. Antoni-Micollier, H. Porte, F. Napolitano, J. Lautier, A. Landragin, and P. Bouyer, "Development of compact cold-atom sensors for inertial navigation," in *Quantum Optics*, J. Stuhler and A. J. Shields, Eds., vol. 9900, International Society for Optics and Photonics. SPIE, 2016, pp. 21 – 37.

[17] S. M. Brewer, J.-S. Chen, A. M. Hankin, E. R. Clements, C. W. Chou, D. J. Wineland, D. B. Hume, and D. R. Leibrandt, "$^{27}Al^{+}$ quantum-logic clock with a systematic uncertainty below 10^{-18}," *Phys. Rev. Lett.*, vol. 123, p. 033201, 2019.

[18] X. Wu, Z. Pagel, B. S. Malek, T. H. Nguyen, F. Zi, D. S. Scheirer, and H. Müller, "Gravity surveys using a mobile atom interferometer," *Sci. Adv.*, vol. 5, no. 9, 2019.

[19] J. A. Rushton, M. Aldous, and M. D. Himsworth, "Contributed review: The feasibility of a fully miniaturized magneto-optical trap for portable ultracold quantum technology," *Review of Scientific Instruments*, vol. 85, no. 12, p. 121501, 2014.

[20] A. Hinton, M. Perea-Ortiz, J. Winch, J. Briggs, S. Freer, D. Moustoukas, S. Powell-Gill, C. Squire, A. Lamb, C. Rammeloo, B. Stray, G. Voulazeris, L. Zhu, A. Kaushik, Y.-H. Lien, A. Niggebaum, A. Rodgers, A. Stabrawa, D. Boddice, S. R. Plant, G. W. Tuckwell, K. Bongs, N. Metje, and M. Holynski, "A portable magneto-optical trap with prospects for atom interferometry in civil engineering," *Philosophical Transactions of the Royal Society A: Mathematical, Physical and Engineering Sciences*, vol. 375, no. 2099, p. 20160238, 2017.

[21] P. D. Lett, W. D. Phillips, S. L. Rolston, C. E. Tanner, R. N. Watts, and C. I. Westbrook, "Optical molasses," *J. Opt. Soc. Am. B*, vol. 6, no. 11, pp. 2084–2107, 1989.

[22] L. Liu, D.-S. Lü, W.-B. Chen, T. Li, Q.-Z. Qu, B. Wang, L. Li, W. Ren, Z.-R. Dong, J.-B. Zhao, W.-B. Xia, X. Zhao, J.-W. Ji, M.-F. Ye, Y.-G. Sun, Y.-Y. Yao, D. Song, Z.-G. Liang, S.-J. Hu, and Y.-Z. Wang, "In-orbit operation of an atomic clock based on laser-cooled ^{87}Rb atoms," *Nat. Commun.*, vol. 9, 2018.

[23] B. Wu, D. Zhu, B. Cheng, L. Wu, K. Wang, Z. Wang, Q. Shu, R. Li, H. Wang, X. Wang, and Q. Lin, "Dependence of the sensitivity on the orientation for a free-fall atom gravimeter," *Opt. Express*, vol. 27, no. 8, pp. 11 252–11 263, 2019.

[24] B. Wu, Z. Wang, B. Cheng, Q. Wang, A. Xu, and Q. Lin, "The investigation of a μgal-level cold atom gravimeter for field applications," *Metrologia*, vol. 51, no. 5, pp. 452–458, 2014.

[25] Q.-Q. Hu, C. Freier, B. Leykauf, V. Schkolnik, J. Yang, M. Krutzik, and A. Peters, "Mapping the absolute magnetic field and evaluating the quadratic zeeman-effect-induced systematic error in an atom interferometer gravimeter," *Phys. Rev. A*, vol. 96, p. 033414, 2017.

[26] V. Menoret, P. Vermeulen, N. L. Moigne, S. Bonvalot, P. Bouyer, A. Landragin, and B. Desruelle, "Gravity measurements below 10^{-9} g with a transportable absolute quantum gravimeter," *Sci. Rep.*, vol. 8, no. 12300, 2018.

[27] Y. Bidel, N. Zahzam, C. Blanchard, A. Bonnin, M. Cadoret, A. Bresson, D. Rouxel, and m.-f. Lalancette, "Absolute marine gravimetry with matter-wave interferometry," *Nat. Commun.*, vol. 9, 2018.

[28] Y. Sakamoto, C. Bidinosti, Y. Ichikawa, T. Satoh, Y. Ohtomo, S. Kojima, C. Funayama, T. Suzuki, M. Tsuchiya, T. Furukawa, A. Yoshimi, T. Ino, H. Ueno, Y. Matsuo, T. Fukuyama, and K. Asahi, "Development of high-homogeneity magnetic field coil for ^{129}Xi edm experiment," *Hyperfine Interact.*, vol. 230, 2015.

[29] N. Holmes, J. Leggett, E. Boto, G. Roberts, R. M. Hill, T. M. Tierney, V. Shah, G. R. Barnes, M. J. Brookes, and R. Bowtell, "A bi-planar coil system for nulling background magnetic fields in scalp mounted magnetoencephalography," *NeuroImage*, vol. 181, pp. 760–774, 2018.

[30] W. Wu, B. Zhou, Z. Liu, J. Wang, L. Xiaoyang, Y. Jia, and G. Liu, "Self-shielded uniform magnetic field coil design for miniature atomic sensors using a particle swarm optimization algorithm," *IEEE Access*, vol. 8, pp. 227 866–227 878, 2020.

[31] N. Cooper, L. Coles, S. Everton, I. Maskery, R. Campion, S. Madkhaly, C. Morley, J. O'Shea, W. Evans, R. Saint, P. Krüger, F. Oručević, C. Tuck, R. Wildman, T. Fromhold, and L. Hackermüller, "Additively manufactured ultra-high vacuum chamber for portable quantum technologies," *Additive Manufacturing*, vol. 40, p. 101898, 2021.

[32] S. H. Madkhaly, L. A. Coles, C. Morley, C. D. Colquhoun, T. M. Fromhold, N. Cooper, and L. Hackermüller, "Performance-optimized components for quantum technologies via additive manufacturing," 2021.

[33] M. Purucker and K. Whaler, "5.06 - crustal magnetism," in *Treatise on Geophysics (Second Edition)*, second edition ed., G. Schubert, Ed. Oxford: Elsevier, 2015, pp. 185–218.

[34] G. McCracken and P. Stott, "Chapter 5 - magnetic confinement," in *Fusion*, G. McCracken and P. Stott, Eds. Burlington: Academic Press, 2005, pp. 47–60.

[35] H. Zhao, S. Crozier, and D. M. Doddrell, "Compact clinical mri magnet design using a multi-layer current density approach," *Magnetic Resonance in Medicine*, vol. 45, no. 2, pp. 331–340, 2001.

[36] N. Holmes, T. M. Tierney, J. Leggett, E. Boto, S. Mellor, G. Roberts, R. M. Hill, V. Shah, G. R. Barnes, M. J. Brookes, and R. Bowtell, "Balanced, bi-planar magnetic field and field gradient coils for field compensation in wearable magnetoencephalography," *Sci Rep*, vol. 9, p. 14196, 2019.

[37] J. D. Jackson, *Electrodynamics, Classical*. American Cancer Society, 2003.

[38] M. J. E. Golay, "Field homogenizing coils for nuclear spin resonance instrumentation," *Review of Scientific Instruments*, vol. 29, no. 4, pp. 313–315, 1958.

[39] F. Roméo and D. I. Hoult, "Magnet field profiling: Analysis and correcting coil design," *Magnetic Resonance in Medicine*, vol. 1, no. 1, pp. 44–65, 1984.

[40] R. Turner, "A target field approach to optimal coil design," *Journal of Physics D: Applied Physics*, vol. 19, no. 8, pp. L147–L151, 1986.

[41] R Turner, "Minimum inductance coils," *Journal of Physics E: Scientific Instruments*, vol. 21, no. 10, pp. 948–952, 1988.

[42] D. Hoult and R. Deslauriers, "Accurate shim-coil design and magnet-field profiling by a power-minimization-matrix method," *Journal of Magnetic Resonance, Series A*, vol. 108, no. 1, pp. 9–20, 1994.

[43] M. Stéphane, "Chapter 13 - inverse problems," in *A Wavelet Tour of Signal Processing (Third Edition)*, third edition ed., M. Stéphane, Ed. Boston: Academic Press, 2009, pp. 699–752.

[44] J. W. Carlson, K. A. Derby, K. C. Hawryszko, and M. Weideman, "Design and evaluation of shielded gradient coils," *Magnetic Resonance in Medicine*, vol. 26, no. 2, pp. 191–206, 1992.

[45] K. Yoda, "Analytical design method of self-shielded planar coils," *Journal of Applied Physics*, vol. 67, no. 9, pp. 4349–4353, 1990.

[46] W. Liu, X. Tang, and D. Zu, "A novel target-field approach to design bi-planar shim coils for permanent-magnet mri," *Concepts in Magnetic Resonance Part B: Magnetic Resonance Engineering*, vol. 37B, no. 1, pp. 29–38, 2010.

[47] L. K. Forbes, M. A. Brideson, and S. Crozier, "A target-field method to design circular biplanar coils for asymmetric shim and gradient fields," *IEEE Transactions on Magnetics*, vol. 41, no. 6, pp. 2134–2144, 2005.

[48] L. K. Forbes and S. Crozier, "A novel target-field method for finite-length magnetic resonance shim coils: I. zonal shims," *Journal of Physics D: Applied Physics*, vol. 34, no. 24, pp. 3447–3455, 2001.

[49] L. Wen-Tao, Z. Dong-Lin, and T. Xin, "A novel approach to designing cylindrical-surface shim coils for a superconducting magnet of magnetic resonance imaging," *Chinese Physics B*, vol. 19, no. 1, pp. 018 701–12, 2010.

[50] D. Green, J. Leggett, and R. Bowtell, "Hemispherical gradient coils for magnetic resonance imaging," *Magnetic Resonance in Medicine*, vol. 54, no. 3, pp. 656–668, 2005.

[51] P. T. While, L. K. Forbes, and S. Crozier, "3d gradient coil design – toroidal surfaces," *Journal of Magnetic Resonance*, vol. 198, no. 1, pp. 31–40, 2009.

[52] P. T. While, J. G. Korvink, N. J. Shah, and M. S. Poole, "Theoretical design of gradient coils with minimum power dissipation: Accounting for the discretization of current density into coil windings," *Journal of Magnetic Resonance*, vol. 235, pp. 85–94, 2013.

[53] L. K. Forbes and S. Crozier, "A novel target-field method for magnetic resonance shim coils: III. shielded zonal and tesseral coils," *Journal of Physics D: Applied Physics*, vol. 36, no. 2, pp. 68–80, 2002.

[54] L. K. Forbes and S. Crozier, "A novel target-field method for finite-length magnetic resonance shim coils: II. tesseral shims," *Journal of Physics D: Applied Physics*, vol. 35, no. 9, pp. 839–849, 2002.

[55] S. Pissanetzky, "Minimum energy MRI gradient coils of general geometry," *Measurement Science and Technology*, vol. 3, no. 7, pp. 667–673, 1992.

[56] C. A. Floudas and V. Visweswaran, *Quadratic Optimization*. Boston, MA: Springer US, 1995, pp. 217–269.

[57] R. A. Lemdiasov and R. Ludwig, "A stream function method for gradient coil design," *Concepts in Magnetic Resonance Part B: Magnetic Resonance Engineering*, vol. 26B, no. 1, pp. 67–80, 2005.

[58] M. Poole and R. Bowtell, "Novel gradient coils designed using a boundary element method," *Concepts in Magnetic Resonance Part B: Magnetic Resonance Engineering*, vol. 31B, no. 3, pp. 162–175, 2007.

[59] K.-H. Chang, "Chapter 19 - multiobjective optimization and advanced topics," in *e-Design*, K.-H. Chang, Ed. Boston: Academic Press, 2015, pp. 1105–1173.

[60] F. A. Potra and S. J. Wright, "Interior-point methods," *Journal of Computational and Applied Mathematics*, vol. 124, no. 1, pp. 281–302, 2000, numerical Analysis 2000. Vol. IV: Optimization and Nonlinear Equations.

[61] J. Christensen and C. Bastien, "Chapter — three - introduction to general optimization principles and methods," in *Nonlinear Optimization of Vehicle Safety Structures*, J. Christensen and C. Bastien, Eds. Oxford: Butterworth-Heinemann, 2016, pp. 107–168.

[62] F.-S. Wang and L.-H. Chen, *Heuristic Optimization*. New York, NY: Springer New York, 2013, pp. 885–885.

[63] M. Zamani-Gargari, M. Nazari-Heris, and B. Mohammadi-Ivatloo, "Chapter 30 - application of particle swarm optimization algorithm in power system problems," in *Handbook of Neural Computation*, P. Samui, S. Sekhar, and V. E. Balas, Eds. Academic Press, 2017, pp. 571–579.

[64] Y. Eren, I. B. Küçükdemiral, and I. Üstoğlu, "Chapter 2 - introduction to optimization," in *Optimization in Renewable Energy Systems*, O. Erdinç, Ed. Boston: Butterworth-Heinemann, 2017, pp. 27–74.

[65] K. Deb, A. Pratap, S. Agarwal, and T. Meyarivan, "A fast and elitist multiobjective genetic algorithm: Nsga-ii," *IEEE Transactions on Evolutionary Computation*, vol. 6, no. 2, pp. 182–197, 2002.

[66] D. W. Boeringer and D. H. Werner, "Particle swarm optimization versus genetic algorithms for phased array synthesis," *IEEE Transactions on Antennas and Propagation*, vol. 52, no. 3, pp. 771–779, 2004.

[67] A. P. Wills, "On the magnetic shielding effect of trilamellar spherical and cylindrical shells," *Phys. Rev. (Series I)*, vol. 9, pp. 193–213, 1899.

[68] E. Boto, N. Holmes, J. Leggett, G. Roberts, V. Shah, S. S. Meyer, L. D. Muñoz, K. J. Mullinger, T. M. Tierney, S. Bestmann, G. R. Barnes, R. Bowtell, and M. J. Brookes, "Moving magnetoencephalography towards real-world applications with a wearable system," *Nature*, vol. 555, pp. 657–661, 2018.

[69] F. P. dos Santos and S. Bonvalot, *Cold-Atom Absolute Gravimetry*. Cham: Springer International Publishing, 2016, pp. 1–6.

[70] I. Moric, P. Laurent, P. Chatard, C.-M. de Graeve, S. Thomin, V. Christophe, and O. Grosjean, "Magnetic shielding of the cold atom space clock pharao," *Acta Astronautica*, vol. 102, pp. 287–294, 2014.

[71] B. Whelan, S. Kolling, B. M. Oborn, and P. Keall, "Passive magnetic shielding in MRI-linac systems," *Physics in Medicine & Biology*, vol. 63, no. 7, p. 075008, 2018.

[72] S. Celozzi, R. Araneo, and G. Lovat, *Appendix B: Magnetic Shielding*. John Wiley & Sons, Ltd, 2008, pp. 282–316.

[73] M. N. O. Sadiku, "A simple introduction to finite element analysis of electromagnetic problems," *IEEE Transactions on Education*, vol. 32, no. 2, pp. 85–93, 1989.

[74] Q. Cao, D. Pan, J. Li, Y. Jin, Z. Sun, S. Lin, G. Yang, and L. Li, "Optimization of a coil system for generating uniform magnetic fields inside a cubic magnetic shield," *Energies*, vol. 11, no. 3, 2018.

[75] R. Turner and R. M. Bowley, "Passive screening of switched magnetic field gradients," *Journal of Physics E: Scientific Instruments*, vol. 19, no. 10, pp. 876–879, 1986.

[76] C. P. Bidinosti, Y. Sakamoto, and K. Asahi, "General solution of the hollow cylinder and concentric dc surface current," *IEEE Magnetics Letters*, vol. 5, pp. 1–4, 2014.

[77] C. Y. Liu, T. Andalib, D. C. M. Ostapchuk, and C. P. Bidinosti, "Analytic models of magnetically enclosed spherical and solenoidal coils," *Nucl. Instrum. Meth. A*, vol. 949, p. 162837, 2020.

[78] T. Liu, A. Schnabel, Z. Sun, J. Voigt, and L. Li, "Approximate expressions for the magnetic field created by circular coils inside a closed cylindrical shield of finite thickness and permeability," *Journal of Magnetism and Magnetic Materials*, vol. 507, p. 166846, 2020.

[79] A. J. Mäkinen, R. Zetter, J. Iivanainen, K. C. J. Zevenhoven, L. Parkkonen, and R. J. Ilmoniemi, "Magnetic-field modeling with surface currents. part i. physical and computational principles of bfieldtools," *Journal of Applied Physics*, vol. 128, no. 6, p. 063906, 2020.

[80] R. Zetter, A. J. Mäkinen, J. Iivanainen, K. C. J. Zevenhoven, R. J. Ilmoniemi, and L. Parkkonen, "Magnetic field modeling with surface currents. part ii. implementation and usage of bfieldtools," *Journal of Applied Physics*, vol. 128, no. 6, p. 063905, 2020.

[81] P. M. Morse and H. Feshbach, *Methods of Theoretical Physics*. New York: McGraw-Hill Book Comp., 1953.

[82] I. N. Sneddon, *Special Functions of Mathematical Physics and Chemistry*. Edinburgh: Oliver & Boyd, 1961.

Appendix A

Cartesian Differentiation of Spherical Harmonics

Let us consider the harmonic

$$\Phi_{nm} = r^n P_{nm}\left(\cos\theta\right)\cos\left(m\left(\phi-\phi'\right)\right). \tag{A.1}$$

The differential of an arbitrary curvilinear coordinate system with respect to another may be expressed as

$$\frac{\partial\Phi_{nm}}{\partial\chi_i} = \sum_j \frac{\partial\xi_j}{\partial\chi_i}\frac{\partial}{\partial\xi_j}\Phi_{nm}. \tag{A.2}$$

Using this, the differential with respect to a Cartesian direction may be determined. Let us start with the x-direction, resulting in

$$\frac{\partial\Phi_{nm}}{\partial x} = \left(\frac{\partial r}{\partial x}\frac{\partial}{\partial r} + \frac{\partial\theta}{\partial x}\frac{\partial}{\partial\theta} + \frac{\partial\phi}{\partial x}\frac{\partial}{\partial\phi}\right)\Phi_{nm}. \tag{A.3}$$

Using the Spherical coordinates (r,θ,ϕ) obtained from the Cartesian coordinates (x,y,z),

$$r = \sqrt{x^2+y^2+z^2}, \qquad \theta = \cos^{-1}\left(\frac{z}{r}\right), \qquad \phi = \tan^{-1}\left(\frac{y}{x}\right). \tag{A.4}$$

Together, using (A.3) and (A.4) results in

$$\frac{\partial\Phi_{nm}}{\partial x} = \left(\cos\phi\sin\theta\frac{\partial}{\partial r} + \frac{\cos\phi\cos\theta}{r}\frac{\partial}{\partial\theta} - \frac{\sin\phi}{r\sin\theta}\frac{\partial}{\partial\phi}\right)\Phi_{nm}. \tag{A.5}$$

Using the differentials of Ferrer's associated Legendre polynomials [81],

$$\frac{\partial P_{nm}\left(\cos\theta\right)}{\partial\theta} = m\cot\theta P_{nm}\left(\cos\theta\right) - P_{n,m+1}\left(\cos\theta\right), \tag{A.6}$$

as well as the relations

$$\cos\left(\left(m+1\right)\phi - m\phi'\right) = \cos\phi\cos\left(m\left(\phi-\phi'\right)\right) - \sin\phi\sin\left(m\left(\phi-\phi'\right)\right) \tag{A.7}$$

$$\cos\left(\left(m-1\right)\phi - m\phi'\right) = \cos\phi\cos\left(m\left(\phi-\phi'\right)\right) + \sin\phi\sin\left(m\left(\phi-\phi'\right)\right), \tag{A.8}$$

results in

$$\frac{\partial \Phi_{nm}}{\partial x} = \frac{r^{n-1}}{2}\Big[\cos\left((m+1)\,\phi - m\phi'\right)A + \cos\left((m-1)\,\phi - m\phi'\right)(A+B)\Big], \tag{A.9}$$

where

$$A = (n-m)\sin\theta P_{nm}\left(\cos\theta\right) - \cos\theta P_{n,m+1}\left(\cos\theta\right), \tag{A.10}$$

and

$$B = \frac{2m}{\sin\theta}P_{nm}\left(\cos\theta\right). \tag{A.11}$$

Substituting the identities in [81]

$$(2n+1)\sin\theta P_{nm}\left(\cos\theta\right) = P_{n+1,m+1}\left(\cos\theta\right) - P_{n-1,m+1}\left(\cos\theta\right) \tag{A.12}$$

$$(2n+1)\cos\theta P_{nm}\left(\cos\theta\right) = (n-m+1)P_{n+1,m}\left(\cos\theta\right) + (n+m)P_{n-1,m}\left(\cos\theta\right) \tag{A.13}$$

directly into (A.10) yields

$$A = -P_{n-1,m+1}\left(\cos\theta\right). \tag{A.14}$$

From this, and (A.11), it is seen that

$$A + B = \frac{2m}{\sin\theta}P_{nm}\left(\cos\theta\right) - P_{n-1,m+1}\left(\cos\theta\right). \tag{A.15}$$

Using Rodrigues' Legendre formula [82] the associated Legendre polynomials may be represented by

$$P_{nm}(x) = \frac{1}{2^n n!}\left(x^2-1\right)^{m/2}\frac{\partial^{n+m}}{\partial x^{n+m}}\left(x^2-1\right)^n. \tag{A.16}$$

Using this relation, we can transform (A.15) into

$$A + B = \frac{\left(1-x^2\right)^{\frac{m-1}{2}}}{2^{n-1}(n-1)!}\Big[m\frac{\partial^{n+m-1}}{\partial x^{n+m-1}}\left(2x\left(x^2-1\right)^{n-1}\right) - \left(1-x^2\right)\frac{\partial^{n+m}}{\partial x^{n+m}}\left(x^2-1\right)^{n-1}\Big], \tag{A.17}$$

where $x = \cos\theta$. Expanding (A.17) through the use of Leibnitz' theorem [81] yields

$$A + B = \frac{\left(1-x^2\right)^{\frac{m-1}{2}}}{2^{n-1}(n-1)!}\Big[-\left(1-x^2\right)\frac{\partial^2}{\partial x^2} + 2mx\frac{\partial}{\partial x} + 2m\left(n+m-1\right)\Big]\frac{\partial^{n+m-2}}{\partial x^{n+m-2}}\left(x^2-1\right)^{n-1}. \tag{A.18}$$

Legendre's differential equation satisfied by $P_{n-1,0}(x)$, which can be expanded using (A.16), is

$$\frac{1}{2^{n-1}(n-1)!}\left[\left(1-x^2\right)\frac{\partial^2}{\partial x^2}-2x\frac{\partial}{\partial x}+n(n-1)\right]\frac{\partial^{n-1}}{\partial x^{n-1}}\left(x^2-1\right)^{n-1}=0. \tag{A.19}$$

Taking the $(m-1)^{\text{th}}$ derivative of (A.19), using Rodrigues' formula once again, whilst also multiplying by a prefactor in order to generate a function of the same form as (A.18), results in

$$\begin{aligned}\frac{\left(1-x^2\right)^{\frac{m-1}{2}}}{2^{n-1}(n-1)!}\Bigg[&\left(1-x^2\right)\frac{\partial^2}{\partial x^2}-2mx\frac{\partial}{\partial x}\\ &-m(m-1)+n(n-1)\Bigg]\frac{\partial^{n+m-2}}{\partial x^{n+m-2}}\left(x^2-1\right)^{n-1}=0.\end{aligned} \tag{A.20}$$

Through the addition of (A.20) and (A.18), the first and second derivatives may now be eliminated, resulting in the simplified equation

$$A+B=(n+m)\left(n+m-1\right)\frac{\left(1-x^2\right)^{\frac{m-1}{2}}}{2^{n-1}(n-1)!}\frac{\partial^{n+m-2}}{\partial x^{n+m-2}}\left(x^2-1\right)^{n-1}. \tag{A.21}$$

Finally, through the use of (A.16), (A.21) can be written as

$$A+B=(n+m)\left(n+m-1\right)P_{n-1,m-1}\left(\cos\theta\right). \tag{A.22}$$

From (A.22), (A.14), and (A.9), we see that the derivative of a spherical harmonic with respect to x is given by

$$\begin{aligned}\frac{\partial\Phi_{nm}}{\partial x}=\frac{r^{n-1}}{2}(&-(1+\delta_{m,0})P_{n-1,m+1}\left(\cos\theta\right)\cos\left(\left(m+1\right)\phi-m\phi'\right)\\ &+(1-\delta_{m,0})(n+m)(n+m-1)P_{n-1,m-1}\left(\cos\theta\right)\cos\left(\left(m-1\right)\phi-m\phi'\right).\end{aligned} \tag{A.23}$$

Similarly, the derivative of a spherical harmonic with respect to y can be shown to be

$$\begin{aligned}\frac{\partial\Phi_{nm}}{\partial y}=\frac{r^{n-1}}{2}(&-(1+\delta_{m,0})P_{n-1,m+1}\left(\cos\theta\right)\sin\left(\left(m+1\right)\phi-m\phi'\right)\\ &-(1-\delta_{m,0})(n+m)(n+m-1)P_{n-1,m-1}\left(\cos\theta\right)\sin\left(\left(m-1\right)\phi-m\phi'\right).\end{aligned} \tag{A.24}$$

Using (A.2) and (A.4) the differential with respect to z is given simply by

$$\frac{\partial\Phi_{nm}}{\partial z}=\left(\cos\theta\frac{\partial}{\partial r}-\frac{\sin\theta}{r}\frac{\partial}{\partial\theta}\right)\Phi_{nm}, \tag{A.25}$$

which, using (A.1), becomes

$$\frac{\partial\Phi_{nm}}{\partial z}=r^{n-1}\cos\left(m\left(\phi-\phi'\right)\right)\left(n\cos\theta P_{nm}\left(\cos\theta\right)-\sin\theta\frac{\partial P_{nm}\left(\cos\theta\right)}{\partial\theta}\right). \tag{A.26}$$

Directly substituting the relation

$$\frac{\partial P_{nm}(\cos\theta)}{\partial\theta} = m\cot\theta P_{nm}(\cos\theta) - \frac{n+m}{\sin\theta}P_{n-1,m}(\cos\theta) \tag{A.27}$$

into (A.26) yields the final expression

$$\frac{\partial\Phi_{nm}}{\partial z} = (n+m)P_{n-1,m}(\cos\theta)\cos\left(m\left(\phi-\phi'\right)\right). \tag{A.28}$$